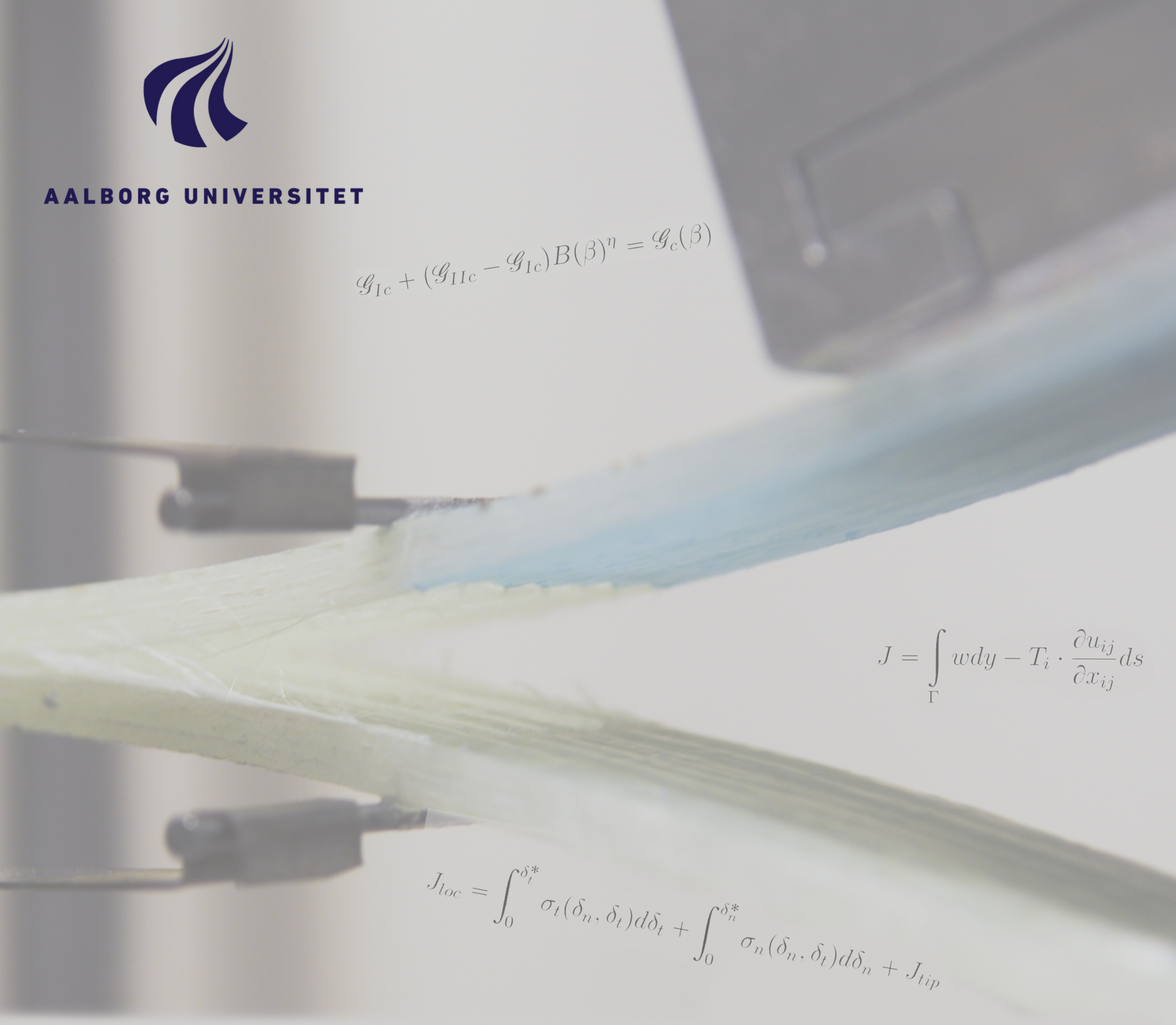


# Development of a test tool for evaluation of cohesive zone parameters in DCB composite specimens

Jon Svenninggaard
Master Thesis
DMS
Aalborg University
December 2014

This master thesis has been written in LaTeX by Jon Svenninggaard, December 2014.

**Study Board of Industry and Global Business Development**
Fibigerstræde 16 DK - 9220 Aalborg East
Phone +45 99 40 93 09
lft@m-tech.aau.dk
http://www.aau.dk

**Title:**
Development of a test tool for evaluation of cohesive zone parameters in DCB composite specimens

**Project Period:**
Fall Semester 2014

**Participant:**
Jon Svenninggaard

**Supervisors:**
Esben Lindgaard
Brian Lau Verndal Bak
Johnny Jakobsen

**Copies:** 3

**Date of Completion:**
December 19, 2014

**Abstract:**

This master thesis main goal has been to develop a test tool, to test for fracture mechanics parameters under mode I, mode II and mode mixity loading using pure moments. The tests specimens are double cantilever beam (DCB) specimens, made from fiber reinforced composites. The test tool, that has been developed and manufactured at Aalborg University. For the verification, that the test tool produces the correct moments and no spurious shear forces are introduced during a test, a test device with strain gauges bonded, has been used together with Digital image correlation (DIC). The test tool has been used to test specimens fabricated from fiberglass and epoxy. Here a 20 $\mu m$ slip film has been inserted between the middle layers to act as a crack starter. Successful mode I tests were conducted and the fracture parameters were used in a programmed finite element script capable of simulating the fracture process of a specimen with the same properties as the one tested.

# Resumé

Dette kandidat projekt på uddannelsen *Design af Mekaniske Systemer* (DMS) ved Aalborg Universitet, omhandler udviklingen og tilblivelsen af et testfikstur til bestemmelse af brudmekaniske parametre i glasfiberforstærkede, såkaldte *double cantilever beam* (DCB) emner. Test fiksturet, der er konstrueret på Aalborg Universitet, er i stand til at teste for brudmekaniske revne parametre under modus I såvel som modus II og blandingsmodus mellem I og II. For at verificere testfiksturet er et værktøj fabrikeret, hvorpå strain gauges er monteret. Sammen med digital image correlation (DIC) og en i et specielt fikstur indbygget last celle, har det derved været muligt at verificere at der under tests ikke bliver introduceret urigtige snitkræfter. Test fiksturet har været anvendt til at teste DCB emner fremstillet af glasfiber og epoxy. Som revnestarter er der indlagt en 20 $\mu m$ tynd slipfilm mellem de midterste lag i laminatet. Der er testet for modus II uden success da ingen revnevækst blev observeret. For blandingsmodus, med modusforholdet 0.5, er der yderligere udført forsøg. Her blev revnevækst observeret i ét forsøg. Forsøgene måtte dog afbrydes pga. store rotationer af prøveemnet. Derimod er der ved modus I, på bagrund af tests, fundet en kritisk energifrigørelsesgrad, som er anvendt i et programmeret script til brug ved FEM analyse. Her er de ved tests fundne data anvendt til at simulere revnevækst for lignende emner.

# Preface

This project is authored by Jon Svenninggaard on the $10^{th}$ semester of Design of Mechanical systems at Aalborg University. The project consists of the hard copy as well as a DVD, which can be found enclosed in the back of the hard copy. The DVD contains a copy of the project as PDF and documents concerning the project. The table of content for the DVD is seen below.

| **Document** | **Description** |
|---|---|
| DMS_Thesis_josv.pdf | The complete thesis as pdf |
| 01 - RevB.pdf | Overall assembly drawing |
| 01-01 - RevB.pdf | Drawing of the frame structure |
| 01-02.pdf | Wire roller assembly |
| 01-03 - RevB.pdf | Fixation tool |
| 01-03-01-02.pdf | Wheel assembly |
| 01-03-02.pdf | Fixation wheel assembly |
| 01-04-01-RevB.pdf | Long roller assembly |
| 01-04-02-RevB.pdf | Short roller assembly |
| 01-05.pdf | Small moment arm assembly |
| 01-10.pdf | Test device |
| VCCT_Test_2D.inp | Ansys APDL script for VCCT calculation |
| Frame.inp | Ansys APDL script for the frame analysis |

The project excluding appendixes, contains 112,962 sign with breaks, which is equivalent to 50 normal pages with 2250 signs per page. Further included is 64 figures, which are equivalent to 750 signs with breaks per figure and is thereby equal to 22 normal pages. This sums up to 72 normal pages. Thereby the limit of 75 normal pages is retained.

Aalborg University, December 19, 2014

Jon Svenninggaard
josv@via.dk

# Acknowledgements

I want to express my sincere gratitude to my supervisors Esben Lindgaard, Brian Bak, and Johnny Jakobsen, for their inspiration, qualified critique, patience, help and friendliness during the long process of writing this thesis. I also want to thank Jens H. Andreasen for his help and talks when the time was short. Further I want to thank my colleague Mohsen Rezaei for assisting with the tests and I would also like to thank Søren Bruun and Klaus Kjær for their assistance in manufacturing the test tool. Not but least my wife and kids for their patience.

# Contents

# List of Figures

# List of Tables

# Chapter 1

# Introduction

## 1.1 Background description

The amount of composites used in industry, increase every year because of the large possibilities that the materials possess including the well-known highly strived for; weight to strength ratio. This is utilized to a far extend in the energy sector, which is the primary driver of this increased use of composites. Here the increased stiffness and low weight in products results in lowering the emissions in the transport sector and is used to increase the production capacity in wind turbines by making the blades longer and lighter.
Because of the manufacturing processes used today, and the natural- heterogeneous properties, composite materials tend to have already included defects built into the material, which over time can lead to failures with catastrophic consequence. The following two quotes are taken from the Seattle newspaper in July 2009 (Gates, 2009).

*"The wing damage that grounded Boeing's new composite 787 Dreamliner occurred under less stress than previously reported — and is more extensive" "The structural flaw in the Boeing design was found in May during a ground test that bent the wings upward. Stresses at the ends of the long rods that stiffen the upper wing skin panels caused the fibrous layers of the composite plastic material to delaminate."*

This shows that even today the knowledge about designing with layered composites is not sufficient. Some parameters are still being assumed and not taken into account. For instance in delamination the cohesive zone, also known as the bridging zone, which can be characterized as a material toughness zone, is not only material

dependent but also size dependent.
The damages due to manufacturing errors, in-plane impacts or other reasons can also result in delamination. The fracture can spread in a composite structure without being found by ordinary visual inspection, because it is hidden between the layers.

Since the beginning of the eighties, Double Cantilevered Beams (DCB) have been subject for analysis of different kind of crack growth behavior and determination of energy release rates (Carlsson and Gillespie, 1990). Today and over the recent years it has, with increasing use of numerical methods and computer efficiency, been very popular to use the cohesive zone modeling approach as a tool to investigate the fracture process in layered fiber composites (Jin and Sun, 2005). The most popular, and standardized approach (ASTM, 2006) and (International Standard, 2001) to test materials in for instance Mode I is using the wedge method. Here a double cantilevered beam (DCB) specimen is mounted with hinges at the tip of the beams in a tensile test machine, and loaded until fracture. See fig. 1.1.

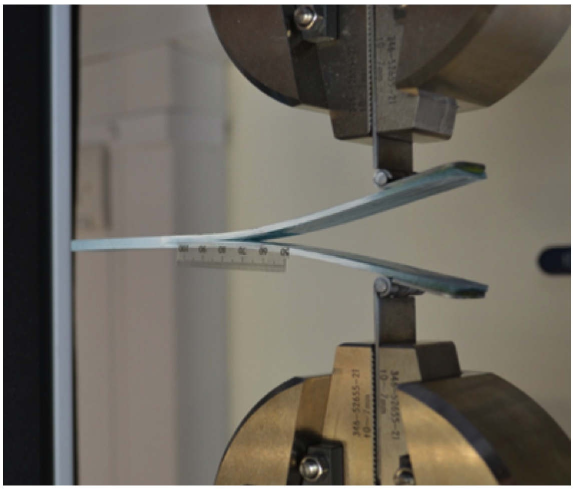

Figure 1.1: DCB - Mode I testing using the wedge method. *Source: accismultifunctional.com*

.

In this process, the crack length must be recorded, which can be a challenging task. The crack growth is not stable as the moment increases with crack length. I.e. the moment in the specimen where the specimen has opened to the onset of damage ($\delta^0$) (figure 1.2) is equal to $M_1 = P \cdot a_0$. When it opens further, assuming the force is kept constant, the moment increases due to the crack propagation i.e. $M_2 = P \cdot a_1$ This can be seen illustrated in figure 1.2. This will be further discussed in a later chapter.

Solutions to overcome this have been proposed over the years. One successful method

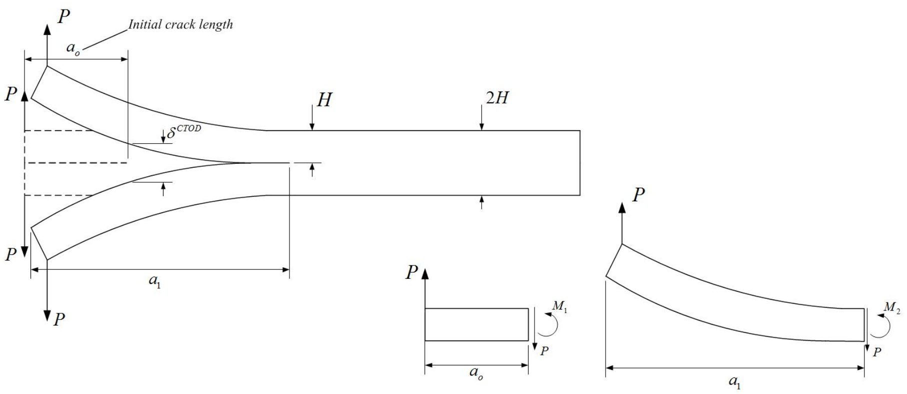


Figure 1.2: Free body diagram of a DCB specimen tested with the wedge method in the unloaded and unloaded state

.

was proposed by Jacobsen and Sørensen (2001). Here the specimen is mounted in a special fixture and using a system of wires. The specimen is then subjected to pure moment, ranging from full mode I crack opening to pure mode II. This system greatly facilitates the determination of the energy release rate of the specimen, by making the specimen energy release rate depending on the crack tip opening displacement $\delta^{\text{CTOD}}$ (CTOD) only. There is however a number of problems in this system.

To minimize the influence of the rotations and displacements in the system, long wires are used. Hence it is not designed for fatigue analysis, since the system is assumed to yield a very low natural frequency (Sørensen et al., 2006). Furthermore the long wires, require a system which is close to 4 meters tall. This limits the system from being used with standard test machines.

## 1.2 The test specimens

The double cantilever beam (DCB) test specimens that are to be tested (see figure 1.1) can be made of various materials. This can for instance be fiber reinforced laminated composites, with fibers and constituents being made from different materials like glass, carbon, or aramide in connection with different forms of epoxies, vinylesters, polyesters or thermoplastics. It can also be different solids, like steel, ceramics or aluminum that are bonded with various forms of glue. However for this project the focus will be on glass fiber reinforced reinforced with epoxy.

The minimum and maximum size of the specimens are chosen to have the following dimensions (height x width x length):

$$min\ 5\ x\ 20\ x\ 200\ mm$$
$$max\ 50\ x\ 30\ x\ 800\ mm$$

### 1.2.1 Discussion about material parameters

In order to determine the loads the test tool is subjected to, it is necessary to know initial material parameters. It is the material parameters, that determine how much load the specimens will be subjected to. According to Sørensen and Jacobsen (2009) it is in various papers ((Huang and Hull, 1989),(Benzeggagh and Kenane, 1996),(Ducept et al., 1997)) discussed that critical energy release rates for mode I loading can range between $\mathscr{G}_{Ic} = 200J/m^2$ and be as high as $\mathscr{G}_{Ic} = 3000J/m^2$ and even higher for mode II loading. In this project the test tool will be designed to handle the maximum size of the specimens (shown in the previous section) in mode I and II loading. The data that has been chosen for further work can be seen in table: 1.1 shown below:

| $E_{11}$ | $\nu_{12}$ | $\mathscr{G}_{Ic}$ | $\mathscr{G}_{IIc}$ |
|---|---|---|---|
| $37\ GPa$ | 0.3 | $500\ \frac{J}{m^2}$ | $3000\ \frac{J}{m^2}$ |

Table 1.1: Initial material values for concept development

Here $E_{11}$ is the modulus of elasticity, $\nu_{12}$ is Poisson's ratio in the 1-2 plane, $\mathscr{G}_{Ic}$ and $\mathscr{G}_{IIc}$ are the critical energy release rates for mode I and II cracking respectively.
These data will be used to find the maximum moment the specimens will be subjected to.

## 1.3 Outline of the project

The scope of this project is to develop a new test tool to test DCB specimens. The specimens have to be subjected to moments resulting in crack openings ranging from pure mode I to mode II. The report is divided into three parts. The first part is covering the theoretical framework needed to analyze the DCB specimens in order later to use the fracture parameters in the FEM. The next part covers the development of the test fixture and a discussion about benefits and drawbacks in the system.The third and last part describes and evaluates the tests, the implementation and results from the FEM and a discussion about further work.

**Theoretical framework**

First the background theory from the classical linear elastic fracture mechanics is presented, where the $J$ - integral is derived. This is then applied to a DCB specimen, to find the energy release rate when it is subjected to mode I with pure moment as well as wedge forces. The later is to show the difference between the two methods. The $J$ - integral is also derived for mode mixities ranging between mode I and mode II.

Then the J - integral is developed for the area around the crack tip, the so called cohesive or bridging zone.

In order to model the cohesive zone, the Barenblatt approach is described, leading to the cohesive zone model. This is shown for mode I crack opening as well as pure mode II and mixed modes between I and II. Then the propagation criteria for mixed mode loading is shown.

**Development of the test fixture**

In order to understand previous test methods, these are described and evaluated, which can be found in appendix A. Then different concepts are developed, based on pure moment application. The various concepts are evaluated using free body diagrams as well as a list of requirements and criteria that needs to be fulfilled. All developed concepts can be found in appendix B.

The chosen concept is developed in detail, and the final test tool is presented.

The differences between the developed fixture and the one previously developed by Bent Sørensen and his team is analyzed. Furthermore the new fixture is evaluated were sources of errors and future improvements are discussed.

**Test results and finite element analysis**

The test specimens are presented, as well as a detailed description about the test methods. The results are treated and analyzed. A script for finite element analysis is presented, and the results from the tests are input. This is followed by an overall conclusion and discussion about further work.

## 1.4 Specification of purpose

With basis in the above, the specific purpose of the project can be formulated as:

*"The purpose of this project is to develop a test tool to evaluate the cohesive zone parameters in DCB composite specimens and verify the experimentally obtained cohesive zone properties in a numerical model"*

# Part I

# Theoretical framework

# Chapter 2

# Introduction to delamination in composite materials

## 2.1 Introduction

Delamination in composite materials is one of the most common failure modes in composites because the interface between the layers (matrix) offers a low resistance path in which cracks can easily grow (Bolotin, 2001). This is because it is the matrix properties that determine the adjacent layers bonding strength.
Delamination might originate from different types of damage. The damage can originate from manufacturing errors, were porosities, foreign objects or bubbles of gas are trapped inside the laminate. It can also arise from low velocity - high force impact, that might damage the matrix inside the laminate. This might come from handling the parts, or drop of a tool on a surface. Even light impacts might cause defects in the upper layers. The damage could also arise from high static loads as well as fatigue loads.

Two different types of delamination can be characterized. Internal in the material, and near the surface. The internal delaminations can be considered cracks and the composite itself as an anisotropic body (Bolotin, 2001). The near surface delaminations are more complicated from a mechanics viewpoint because the deformations of the delaminated section does not necessary follow the deformation of the rest of the laminate. Not only the growth of the delamination needs to be taken into consideration but also the local (buckling) stability of the section or part of the composite. This is important for laminates in compression, were the delaminated lamina's may buckle, which can result in cracks propagating. Figure (2.1) shows a thin shell, which could be assumed as part of a wind turbine blade, with a near surface delamination subjected to compressive loads.

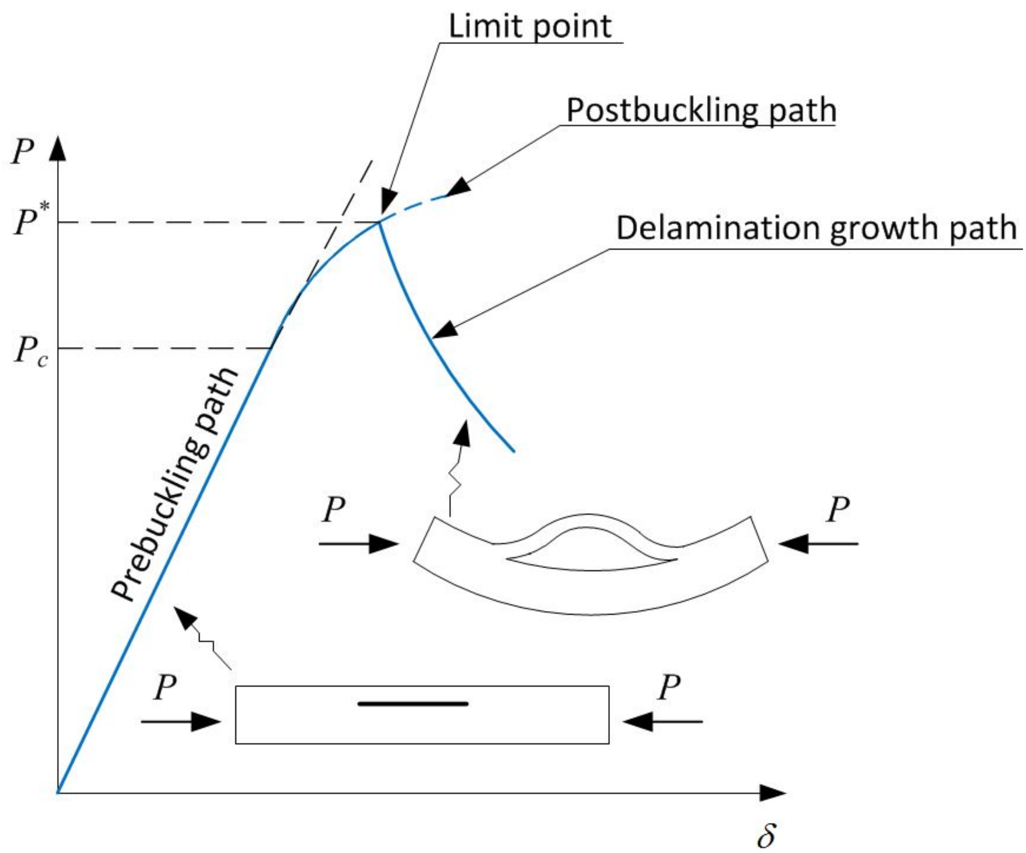


Figure 2.1: Buckling of a thin shell with delamination - freely inspired from (Barbero (2007) p.256)

The shell buckles due to the compressive load. The critical point $P_c$ is were the compressive membrane stresses, transform into bending stress. At the bifurcation point $P^*$, the shell looses its load carrying capability.

In order to verify the strength in the design phase, engineers often turn to using numerical simulation as the finite element method. But in order to simulate delaminations, the finite element program needs material input in form of critical energy release rates, maximum tractions and displacements during the delamination phase. These material properties must be characterized by tests.

# Chapter 3

# Basics of fracture mechanics

Fracture mechanics could be characterized into several groups. In this study the main concepts from the classic linear elastic fracture mechanics (LEFM) approach will be presented.
Generally LEFM could be divided into two approaches that can be used to find the crack properties. Either looking at the crack tip itself using the stress intensity factor (SIF) or looking at the energy balance for the entire structure using the energy approach to get the the strain energy release rate $\mathscr{G}$ (SERR).

This chapter is divided into four sections. First the SERR will be presented, then the concept of the SIF will be demonstrated, and followed by the relation between the SERR and SIF.

Then finally the concept of using the $J$ - Integral will be discussed. The $J$ - integral will be used in the analytical derivation of the SERR for the Double Cantilevered Beam (DCB) subjected to pure moment application as well as wedge forces. The later will be presented in order to illustrate the problems that are encountered using this test method, as was discussed in the introduction!

## 3.1 Linear Elastic Fracture Mechanics

Looking at the energy balance in a body with an initial crack of length $a$ (see figure 3.1a), and starting by showing the total elastic potential as (Andreasen, 2010):

$$\Pi = U + V \tag{3.1}$$

Where $\Pi$ is the total elastic potential, $U$ is the internal strain energy and $V$ is the potential of the outer forces. In order to have the system in equilibrium, variation of total elastic potential for small displacement field $\delta u$ must be zero, i.e.

$$\delta\Pi = \delta U + \delta V = 0 \tag{3.2}$$

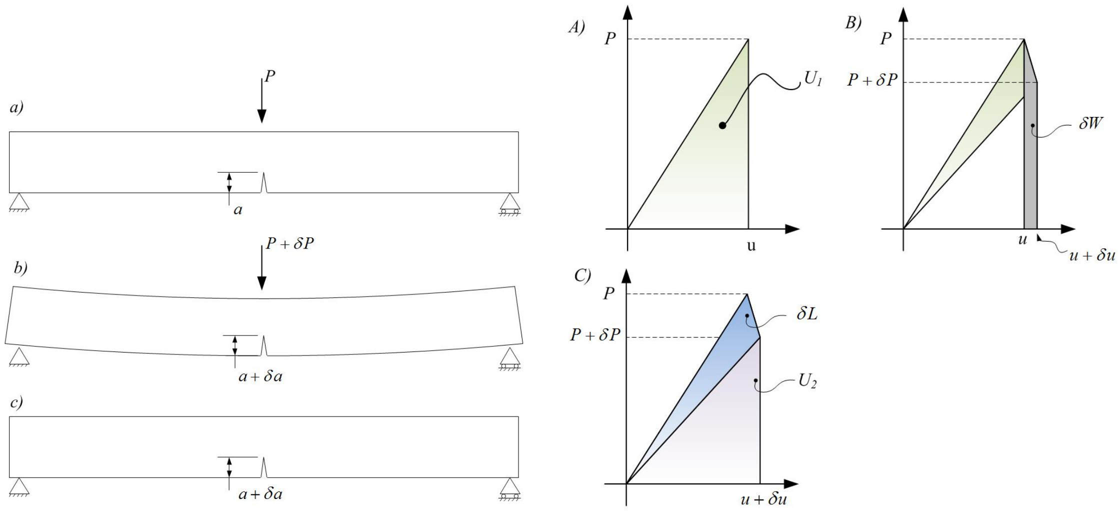


(a) (b)

Figure 3.1: The energy process

It is assumed that there is a crack with length $a$ in a solid body (Figure 3.1b(a)), and the body is initially unloaded. Load will be increased slowly from 0 to $P$. Hence dynamic terms is neglected. Deflections will grow from 0 to $u$ (figure 3.1b(A)). In this stage strain energy will reach $U_1$. By increasing the load to $P + \delta P$ (figure 3.1b(b)), crack grows from $a$ to $a + \delta a$, where $\delta a$ is of negligible size. The work of outer forces are equivalent to $\delta W$ (figure 3.1b(B)) and is given as:

$$\delta W = -\delta V \cong P\delta u \tag{3.3}$$

Where $P$ is the external force, $u$ is the displacement and $W$ the work. By unloading the body, the energy will be returned to $U_2$ (figure 3.1b(c)). The energy that is used in the process to form the new crack faces is shown in figure 3.1b(C) and is:

$$\delta L = \delta W - \delta U \tag{3.4}$$

By assumption of small displacements, elastic potential variation can be written as:

$$\delta\Pi = U(u + \delta u, a + \delta a) + V(u + \delta u, a + \delta a) - U(u, a) - V(u, a) \tag{3.5}$$

Rewriting equation 3.5, with small changes in crack length $a$, there will be a small increment in $U$ and $V$ per crack length:

$$\begin{aligned}\delta\Pi = U(u+\delta u,a) + \frac{\partial U(u+\delta u,a)}{\partial a}\delta a - U(u,a) + ...\\ V(u+\delta u,a) + \frac{\partial V(u+\delta u,a)}{\partial a}\delta a - V(u,a)\end{aligned} \tag{3.6}$$

According to (3.5), sum of changes in internal strain energy and external potential must be zero, eq. (3.6) becomes:

$$\delta\Pi = \frac{\partial U(u+\delta u,a)}{\partial a}\delta a + \frac{\partial V(u+\delta u,a)}{\partial a}\delta a \tag{3.7}$$

Which again can be written as:

$$\delta\Pi = \frac{\partial}{\partial a}[U(u+\delta u,a) + V(u+\delta u,a)]\delta a = \frac{\partial \Pi}{\partial a} \tag{3.8}$$

As stated in eq. (3.4), and remembering that $\delta W = -\delta V$, eq. (3.8) is rewritten:

$$\frac{\partial \Pi(u,a)}{\partial a}\delta a = \frac{\partial}{\partial a}[U(u,a) - W(u,a)]\delta a \tag{3.9}$$

The change in strain energy and outer potential is equal to:

$$\delta U = \frac{\partial U\,(u,a)}{\partial a}\delta a \delta V = \frac{\partial V\,(u,a)}{\partial a}\delta a \tag{3.10}$$

The change in energy is then found by comparing (3.4) and (3.9):

$$\delta L = -\frac{\partial V}{\partial a}\delta a - \frac{\partial U}{\partial a}\delta a = -\frac{\partial \Pi\,(u,a)}{\partial a}\delta a \tag{3.11}$$

By assumption of independent energy change of fracture area:

$$\mathscr{G} = -\frac{1}{t}\frac{\partial \Pi}{\partial a} \tag{3.12}$$

This is defined as the Griffith energy release rate ($\mathscr{G}$) and describes the energy released per new crack face when the crack grows. The fracture criterion is met when the energy release rate is equivalent to the critical energy release rate, indexed $\mathscr{G}_c$, or in other words, if the crack can consume the energy which is input to the system, the crack will grow in a stable manner. If the crack releases its energy, it will grow unstable. Stable crack growth is obtained for:

$$\mathscr{G} \leqslant \mathscr{G}_c \tag{3.13}$$

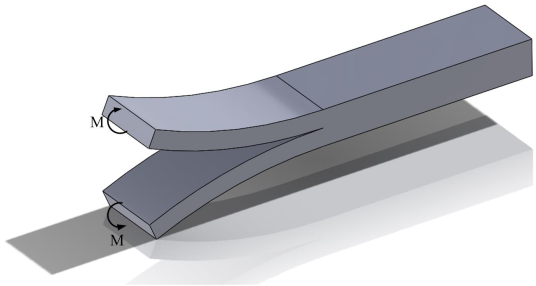


Figure 3.2: DCB Specimen subjected to pure moment

For a Double Cantilever Beam (DCB), as shown in 3.2, the strain energy in one beam can be expressed as (Gere and Goodno, 2012):

$$U = \frac{1}{2}\int_0^a \frac{M^2}{2EI}dx = \frac{aM^2}{4EI} \tag{3.14}$$

Where the integral is evaluated along the entire crack length $a$. The potential of the outer forces for one beam can be expressed as:

$$V = -W = -\frac{M \cdot v'(0)}{2} = -\frac{aM^2}{2EI} \tag{3.15}$$

The total elastic potential for both beams is then:

$$\Pi = U + V = 2\frac{aM^2}{4EI} - 2\frac{aM^2}{2EI} = -\frac{aM^2}{EI} \tag{3.16}$$

The energy release rate can then be expressed as:

$$\mathscr{G} = -\frac{1}{t}\frac{\partial \Pi}{\partial a} = \frac{M^2}{tEI} \tag{3.17}$$

$M$ is the moment applied to each beam end, $t$ is the thickness of the beam,$E$ is Young's modulus, and $I$ is the moment of inertia for the beam and given as $I = \frac{tH^3}{12}$ where $H$ is the height of one beam end.

## 3.2 Stress intensity factor

Looking at the local stress field in terms of the Cartesian coordinates, which is a function of the far field stress, and the polar coordinates, measured from the crack tip as shown in figure 3.3.

Stresses in front of the crack tip can be expressed in terms of the Stress Intensity Factor (SIF), the radius $r$ and the angle $\theta$. These expressions for a 2D state of stress, and a mode I crack, can be seen below in eq. 3.18.

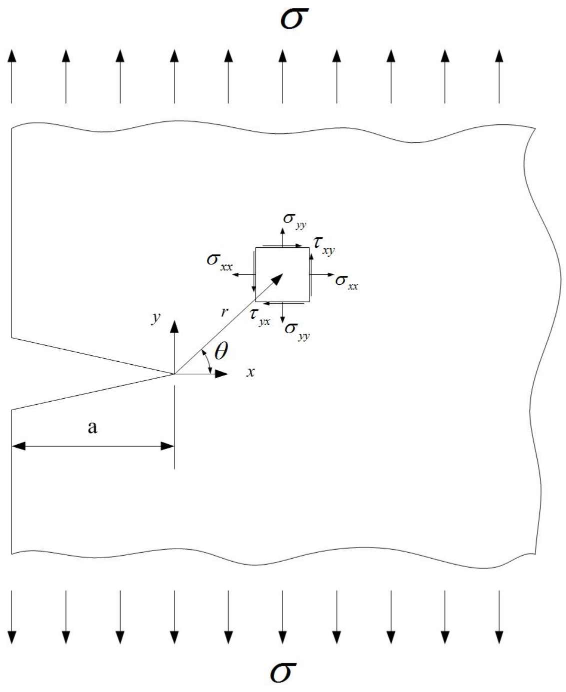


Figure 3.3: Crack tip stresses

$$
\begin{aligned}
\sigma_{xx} &= \frac{K_I}{\sqrt{2\pi r}}\cos\left(\frac{\theta}{2}\right)\left(1-\sin\left(\frac{\theta}{2}\right)\sin\left(\frac{3\theta}{2}\right)\right)\\
\sigma_{yy} &= \frac{K_I}{\sqrt{2\pi r}}\cos\left(\frac{\theta}{2}\right)\left(1+\sin\left(\frac{\theta}{2}\right)\sin\left(\frac{3\theta}{2}\right)\right)\\
\tau_{xy} &= \frac{K_I}{\sqrt{2\pi r}}\sin\left(\frac{\theta}{2}\right)\cos\left(\frac{\theta}{2}\right)\cos\left(\frac{3\theta}{2}\right)
\end{aligned}
\tag{3.18}
$$

These can be derived from the Westergaard complex stress function and can be found in for instance (Anderson, 2005) and (Andreasen, 2010). For a location in the crack plane, where $\theta = 0$, equation (3.18) reduces to:

$$
\begin{aligned}
\sigma_{xx} = \sigma_{yy} &= \frac{K_I}{\sqrt{2\pi r}}\\
\tau_{xy} &= 0
\end{aligned}
\tag{3.19}
$$

Fracture will occur when the SIF increases to its critical value. For a mode I crack, shown in figure 3.4a, the crack will propagate in an unstable manner if:

$$K_I \geqslant K_{Ic} \tag{3.20}$$

The corresponding symmetry displacement modes for mode I, II and III can be

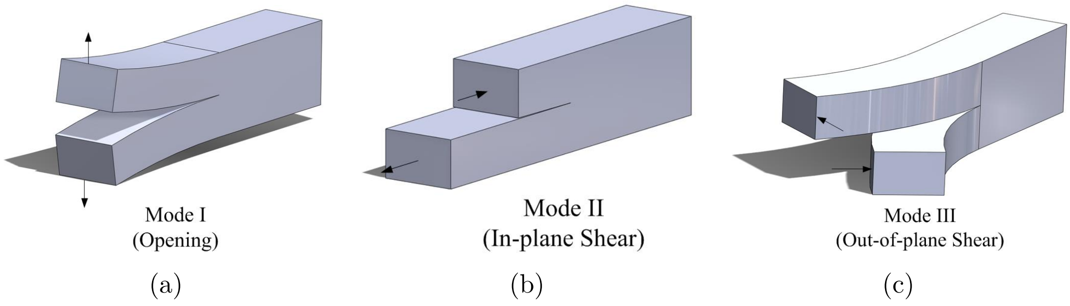


Figure 3.4: Modes of crack extension; Mode I, Mode II, and Mode III

shown as (Andreasen, 2010):

$$\begin{array}{llll} \text{Mode I}: & u^+ = u^- & v^+ = -v^- & w^+ = w^- \\ \text{Mode II}: & u^+ = -u^- & v^+ = v^- & w^+ = w^- \\ \text{Mode III}: & u^+ = u^- & v^+ = v^- & w^+ = -w^- \end{array} \tag{3.21}$$

Displacements in $u$, $v$ and $w$ directions indicate directions of displacements, were $^+$ and $^-$ signs indicate upper or lower fracture surface.

In principle all three different crack modes can exist at the same time, however focusing on plane problems, i.e. neglecting out of plane shear mode (mode III). Then determining the ratio of mode mixities, the phase angle is introduced as (Andreasen, 2010):

$$\psi = \tan^{-1}(\frac{\mathrm{K_{II}}}{\mathrm{K_{I}}}) \tag{3.22}$$

Pure mode I is corresponding to $\psi = 0$ and pure mode II is $\psi = \pi/2$ (Andreasen, 2010). Mode mixity is often referred to the ratio between two modes and is expressed in term of the SERR, which is similar to the SIF as:

$$\beta = \frac{\mathscr{G}_{II}}{\mathscr{G}_{I} + \mathscr{G}_{II}} \tag{3.23}$$

This shows, that $\beta = 0$ for pure mode I, and $\beta = 1$ for pure mode II. Here only modes I and II are taken into account.

## 3.3 Relation between the SERR and SIF

Using the crack closure method (CCM), the relation between the energy release rate and the stress intensity factor approach for plane stress is (Andreasen, 2010):

$$\mathscr{G}_I = \frac{{K_I}^2}{2\mu\left(1+\nu\right)} = \frac{{K_I}^2}{E} \tag{3.24}$$

Where the index $I$ represents mode $I$, $\mu$ is the shear modulus and $\nu$ is Poisson's ratio.

## 3.4 The $J$ - integral

The path independent $J$ – integral first proposed by (Rice, 1968), which is another way to show the energy release rate for a cracked body and is equivalent to $\mathscr{G}$ for LEFM. It can be used regardless of elastic or elastic-plastic material behavior, which makes it suitable for DCB specimens as in this case with bridging behavior of the fiber ligaments, which is called large scale bridging (LSB). The integral is expressed as (Andreasen, 2010):

$$J = \int\limits_{\Gamma} wdy - T_i \cdot \frac{\partial u_{ij}}{\partial x_{ij}} ds \tag{3.25}$$

Here $\Gamma$ is a curve surrounding the tip of the notch, $w$ being the strain energy density defined as:

$$w\left(x,y\right) = \int_0^{\varepsilon_{ij}} \sigma_{ij} d\varepsilon_{ij} \tag{3.26}$$

And $T_i$ is the traction vector depending on the outward normal i.e.

$$T_i = \sigma_{ij} n_j \tag{3.27}$$

Also it is assumed that:

$$J = \mathscr{G} \tag{3.28}$$

The relation between the energy release rate and the stress intensity factor $K$ is shown for mode I and plane stress as (Andreasen, 2010):

$$\mathscr{G}_I = \frac{{K_I}^2}{E} \tag{3.29}$$

And for plane strain as:

$$\mathscr{G}_I = \frac{(1-\nu^2){K_I}^2}{E} \tag{3.30}$$

## 3.5 DCB subjected to pure mode I moment

Applying the J - integral to a DCB specimen subjected to pure mode I loading is shown here.

Consider the DCB specimen in figure 3.5. It is subjected to even but with opposite direction bending moments on the two beam ends. The total beam height is $2H$ and the crack length is $a$. The path for the $J$ integral $\Gamma_{ext}$ is routed along the outer edges of the specimen, so that $\Gamma_{ext} = \Gamma_1 + \Gamma_2 + \Gamma_3 + \Gamma_4 + \Gamma_5$ Applying the $J$ - integral from eq. 3.25 no tractions exist on free surfaces, i.e. $T_i = 0$ on $\Gamma_2$ $\Gamma_3$ and $\Gamma_4$.

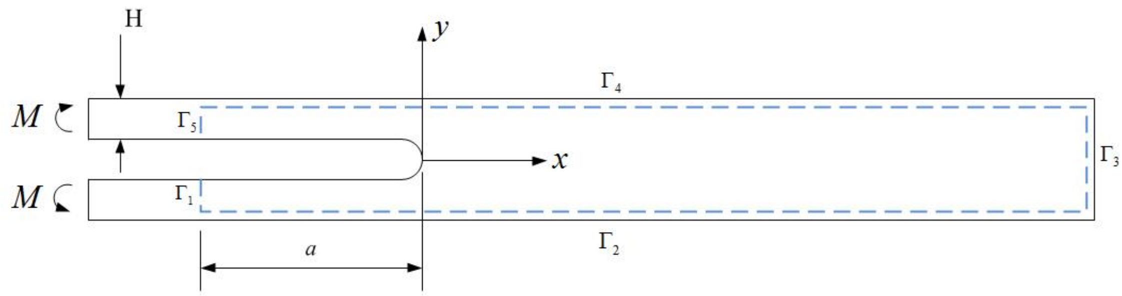


Figure 3.5: J - Integral

This means that there is no contribution to the $J$ - integral along these boundaries as $dy = 0$ and $T_i = 0$. Furthermore the strain energy density, $w = 0$ on the boundary $\Gamma_3$ , because neither stress nor strain exists on that path. Along the segments $\Gamma_1$ and $\Gamma_5$, $dS = -dy$ due to the integration direction counterclockwise. At $x = -a$, it is assumed that the tractions $T_y = 0$ because there is only stresses in the $x$ direction, due to pure moment. This way $T_x = -\sigma_{xx}$ . With the strain energy defined in this situation as:

$$w = \tfrac{1}{2}\sigma_{xx}\epsilon_{xx} \tag{3.31}$$

And the normal vector for $\Gamma_1$ is:

$$n_1 = (-1, 0, 0) \tag{3.32}$$

Using the above equations, the second part of (3.25) can be written as:

$$T_i \frac{\partial u_{ij}}{\partial x_{ij}} = \sigma_{ij} n_j \frac{\partial u_{ij}}{\partial x_{ij}} = \sigma_{xx} n_1 \varepsilon_{xx} = -\sigma_{xx}\varepsilon_{xx} \tag{3.33}$$

Then the integral for $\Gamma_1$, over the height of one of the beams $H$, can then be shown as:

$$
\begin{aligned}
J_1 &= \int_0^{-H} \frac{1}{2}\sigma_{xx}\varepsilon_{xx}dy - \int_0^{-H} -\sigma_{xx}\varepsilon_{xx}dS \\
J_1 &= \int_0^{-H} \frac{1}{2}\sigma_{xx}\varepsilon_{xx}dy - \int_0^{-H} \left(\sigma_{xx}\varepsilon_{xx}\right)dy \\
J_1 &= -\int_0^{-H} \frac{1}{2}\sigma_{xx}\left(y\right)\varepsilon_{xx}\left(y\right)dy \\
J_1 &= \int_0^{H} \frac{\sigma_{xx}^2}{E}dy
\end{aligned}
\tag{3.34}
$$

Using Bernoulli - Euler beam theory, the normal stress is defined as (Gere and Goodno, 2012):

$$
\sigma_{xx} = \frac{M\left(\frac{H}{2} - y\right)}{I_z} \tag{3.35}
$$

The integral in (3.34) can be written as:

$$
J_1 = \int_0^{H} \frac{M^2\left(\frac{H}{2} - y\right)^2}{2EI_z^{\;2}}dy = \frac{M^2H^3}{24EI_z^{\;2}} \tag{3.36}
$$

Since the moment of inertia for a square beam is defined as:

$$
I_z = \frac{tH^3}{12} \tag{3.37}
$$

Eq. (3.36) becomes:

$$
J_1 = \frac{M^2}{2tEI_z} \tag{3.38}
$$

It can be shown that integration of path 5 ($\Gamma_5$) yields the same result. Therefore the entire $J$ integral, hereafter named $J_{ext}$ (because it is evaluated along the external edges of the specimen), becomes:

$$
\boxed{J_{ext} = \frac{M^2}{tEI_z}} \tag{3.39}
$$

Which is similar to the energy release rate $\mathscr{G}$ shown in eq. (3.17).

## 3.6 DCB specimen subjected to wedge forces

Considering the specimen which was shown in figure 1.2, and applying the $J$ - integral as discussed in the previous subsection, it is illustrated by the FBD in figure 3.6:

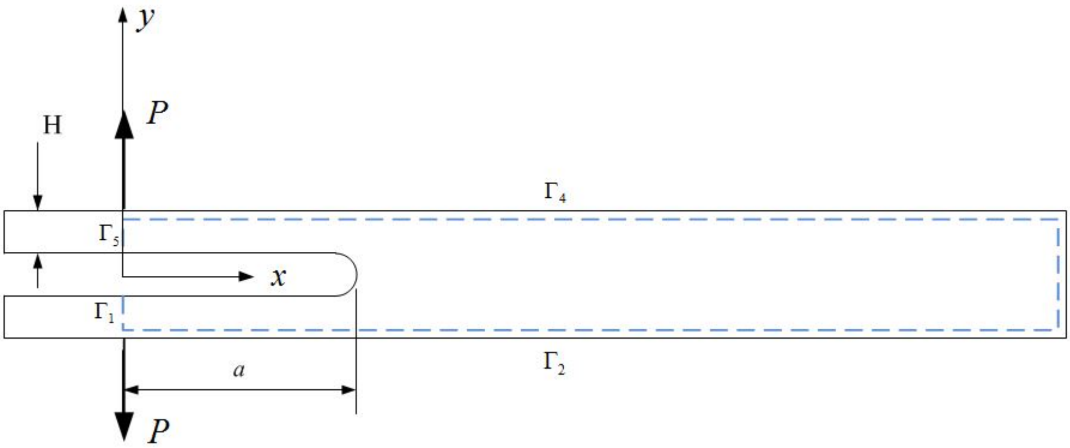


Figure 3.6: J - Integral applied with wedge forces

As in the previous section 3.5 only path 1 and 5 are considered due to $dy = 0$ on path 2 and 4, furthermore $T_i = 0$ on path 2, 3, and 4. Focusing on path 1, and writing a deflection expression for the lower beam and differentiate wrt. $x$ to utilize that $u_y = v(x)$ and $u_{y,x} = \frac{\partial v(x)}{\partial x}$ to get:

$$\frac{\partial v(x)}{\partial x} = -\frac{P \cdot (a^2 - x^2)}{2E \cdot I} \tag{3.40}$$

Writing out the J- Integral using that $u_{x,x} = \varepsilon_{xx} = \frac{\sigma_{xx}}{E}$ and $dS = -dy$ gives:

$$J_1 = \int_0^{-H} \frac{\sigma_{xx}^2}{2E} + \sigma_{xy} \cdot \frac{P \cdot (a^2 - x^2)}{2EI} dy \tag{3.41}$$

Using (Gere and Goodno, 2012):

$$\int_0^{-H} \sigma_{xy} dy = -\frac{P}{t} \tag{3.42}$$

Were $t$ is the thickness of the beam. Using Bernoulli - Euler beam theory the normal stress is given as:

$$\sigma_{xx} = \frac{M \cdot (H/2 - y)}{I} = \frac{P \cdot a \cdot (y - H/2)}{I} \tag{3.43}$$

Substituting equations 3.42 and 3.43 into 3.41, to get:

$$J_1 = \int_0^{-H} \frac{P^2x^2(y-H/2)^2}{2EI^2} + \frac{P^2(a^2-x^2)}{2tEI} dy \tag{3.44}$$

The first part of the integral in equation 3.44, can be expressed as:

$$\int_0^{-H} (y-H/2)^2 dy = -\frac{I}{t} \tag{3.45}$$

Then:

$$J_1 = \frac{P^2a^2}{2tEI} \tag{3.46}$$

Again it can be shown that the $J$ - integral for path 5 is the same as for path 1, and the total $J$ - integral is:

$$\boxed{J_{ext} = \frac{P^2a^2}{tEI}} \tag{3.47}$$

Comparing eq. 3.39 (Pure moment) and eq. 3.47 (Wedge forces), it could be concluded that the energy release rate is depending on the crack length squared. This requires that the crack length is monitored closely throughout the test, and assumed that the force applied is adjusted correspondingly in order achieve stable crack growth.

# 3.7 DCB specimen subjected to mode mixety

Considering the DCB in figure 3.7, that is subjected to mode mixety, i.e. $M_1 \neq M_2$ and $|M_1| < M_2$.

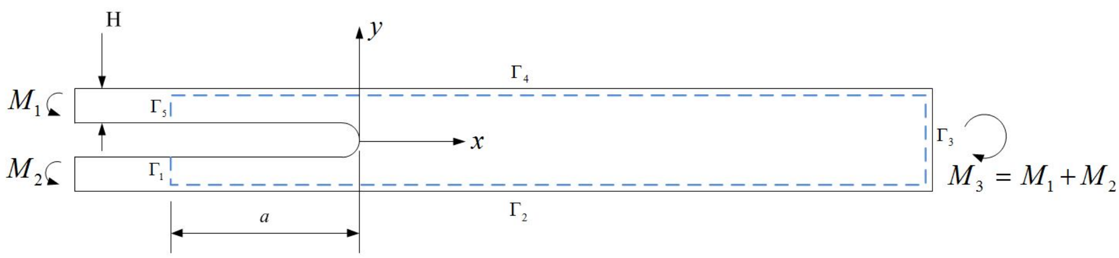


Figure 3.7: $J$ - Integral applied with uneven bending moments

From section 3.5, equation 3.38, the $J$ - integral for path 1 is expressed as:

$$J_1 = \frac{M_2^2}{2tEI_z} \tag{3.48}$$

For path 5, as:

$$J_5 = \frac{M_1^2}{2tEI_z} \tag{3.49}$$

For path 3, where $T_i$ is no longer zero, must be evaluated. Stresses in the $x$ - direction are the only present as pure moment is applied. Hence utilizing Bernoulli - Euler beam theory, the normal stress is expressed as:

$$\sigma_{xx} = \frac{M_3 \cdot y}{I_z} \tag{3.50}$$

And the moment of inertia is:

$$I_z = \frac{t \cdot (2H)^3}{12} = \frac{8H^3 t}{12} \tag{3.51}$$

Now the normal vector to $\Gamma_3$ is defined as:

$$n_3 = (1, 0, 0) \tag{3.52}$$

Stresses and strains only exists in the $x$ direction, therefore the above normal vector is inserted into the $J$ - integral and finding:

$$\begin{aligned}
J_3 &= \int_{-H}^{H} \tfrac{1}{2}\sigma_{xx}(y)\varepsilon_{xx}(y)dy - \int_{-H}^{H} \sigma_{xx}(y)\varepsilon_{xx}(y)dy \\
J_3 &= -\int_{-H}^{H} \tfrac{1}{2}\sigma_{xx}(y)\varepsilon_{xx}(y)dy \\
J_3 &= -\int_{-H}^{H} \frac{{\sigma_{xx}}^2}{2E}dy \\
J_3 &= -\frac{3M_3^2}{4H^3t^2E}
\end{aligned} \tag{3.53}$$

Substituting $M_3 = M_1 + M_2$, $J_3$ becomes:

$$J_3 = -\frac{3(M_1 + M_2)^2}{4H^3t^2E} \tag{3.54}$$

With;

$$J_1 = \frac{6M_2^2}{H^3t^2E} \tag{3.55}$$

And;

$$J_5 = \frac{6M_1^2}{H^3t^2E} \tag{3.56}$$

Then expressing the total $J$ - integral by summing the individual contributions to get:

$$\boxed{J_{ext} = \frac{21(M_1^2 + M_2^2) - 6M_1 \cdot M_2}{4H^3t^2E}} \tag{3.57}$$

This is shown for plane stress. For plane strain, eq. 3.57, must be multiplied with $(1 - \nu^2)$, where $\nu$ is poisson's ratio. It is important to note that the J- integral for mixed mode loading is still only depending on $M_1$, $M_2$ as well as the constants $H$, $t$ and $E$.

For pure mode II loading the two applied moments are equal and in the same direction, i.e. $M = M_1 = M_2$ in eq. 3.57. This results in:

$$\boxed{J_{ext} = \frac{9M^2}{H^3t^2E}} \tag{3.58}$$

## 3.8 Length of the fracture process zone

Another important parameter is to determine when LEFM applies. The length $L$ of the fracture process zone (FPZ), must be small compared to other specimen dimensions ($a_0$, $t$, $H$) in order to be confined in the $K$- dominant region. Here $a_0$ is the pre-made crack, $t$ is the thickness, $H$ is the beam height. According to (Andreasen, 2010), the geometry dimensions must fulfill the following:

$$L < 2.5 \cdot \frac{K_{Ic}^2}{\sigma_y^2} \tag{3.59}$$

Substituting $J_{Ic}$ into $K_{Ic}$'s place, and the yield stress $\sigma_y$, with the cohesive peak stress $\sigma_n^0$ the equation gives

$$L < 2.5 \cdot \frac{J_{Ic}E}{(\sigma_n^0)^2} \tag{3.60}$$

Sørensen (2010), established a non - dimensional parameter to describe this as:

$$\alpha = \frac{a}{L} = \frac{a(\sigma_n^0)^2}{J_{Ic}E} \tag{3.61}$$

This implies that for large $\alpha$ the length of the FPZ is small and it may be confined within the $K$ - dominant region and hence LEFM applies. This is the case for many metallic materials, but not for fiber reinforced composites where the FPZ length $L$ is long.

## 3.9 Conclusion

In this chapter the basics of the elastic fracture mechanics was shown. First the relation between the total elastic potential and the energy release rate was shown. Then the energy release rate was calculated for a DCB specimen subjected to pure moment application. Then the stress intensity factor is presented and the relation between it and the strain energy release rate is shown. Finally the $J$ - integral is presented and applied to a DCB specimen subjected to pure moments in a mode I loading setup. Followed by a DCB specimen, subjected to wedge loads in a mode I setup. This is done to show that the SERR for pure moment application is only depending on the moment and not the crack length. Furthermore a DCB specimen subjected to pure moments in a mixed mode and mode II setup is analyzed. Finally the length of the FPZ is used to evaluate if LEFM applies.

# Chapter 4

# Cohesive zone modeling

## 4.1 Introduction

This chapter gives an introduction to the cohesive zone method, and development of the cohesive laws for mode I, II and mode mixities in between.

## 4.2 The cohesive zone concept

Leaving the non-trivial concept of using the LEFM approach and complicated concept, that the stresses at the crack tip are infinitely large. The concept of using the cohesive zone model is a different approach, were a zone of finite or zero thickness is placed in front of the crack tip. The purpose of this zone is to describe the stress field more realistically without using the stress singularity approach from the LEFM. Ideally the crack front is described as two cohesive surfaces which are held together by cohesive tractions. The failure is characterized as complete separation of the two cohesive surfaces. And the process is described using a cohesive law, that relates the tractions on the surfaces to the relative opening between the surfaces (see figure 4.1).

This concept originates back to Barenblatt (1961), where he believed that the crack tip surfaces were held together by the atomic bonding forces of the material. The cohesive traction's can have a magnitude of up to the theoretical strength of the material. Essentially the method outlined by Barenblatt (1961), removes the crack tip stress intensity factor $K_I$. This model avoids using the SIF, but introduces another problem, i.e. linking different scales atomic forces and continuum mechanics. Furthermore in the Barenblatt model the cohesive zone is a small segment behind the crack front, were the actual cohesive zone model is assuming a strip in front of the crack front.

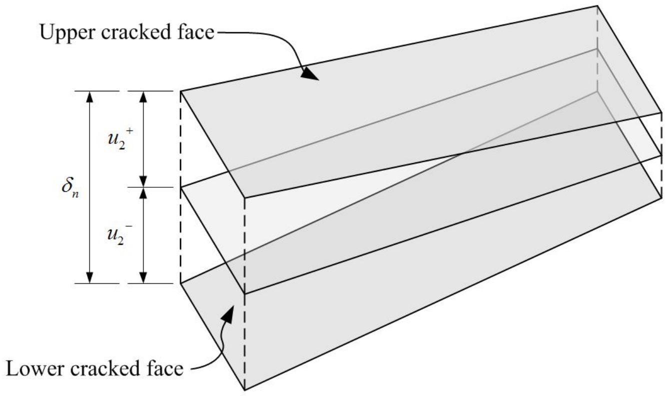


Figure 4.1: Sketch of the two cracked faces and the relative opening

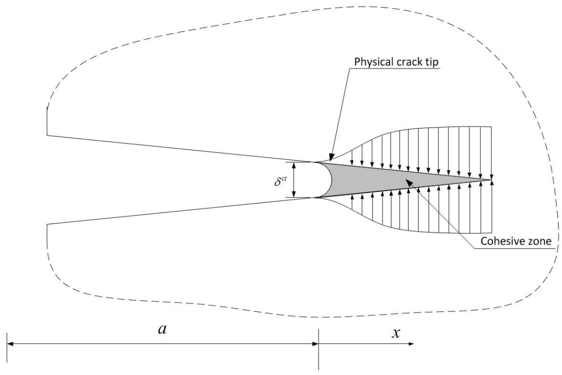


Figure 4.2: The cohesive zone in front of the crack tip

For the cohesive zone approach, in general it is, assumed that the upper and lower cracked surfaces are held together by cohesive tractions. These tractions are related to the separation of two surfaces, so that when full separation is applied, there are no tractions left on the surfaces. The cohesive law can for instance for a pure mode I loading be described by a function that relates tractions to displacements as seen in the figure 4.3.

The function can be described as (Sørensen, 2010):

$$\sigma_n = \sigma_n(\delta_n) \tag{4.1}$$

Assuming that only normal opening exists. I.e. $\sigma_n(\delta_n)$ and that $\delta_t = 0$. In the general case the normal and tangential stresses are depending on both the normal and tangential opening. I.e.

$$\sigma_n = \sigma_n(\delta_n, \delta_t) \;\wedge\; \sigma_t = \sigma_t(\delta_n, \delta_t) \tag{4.2}$$

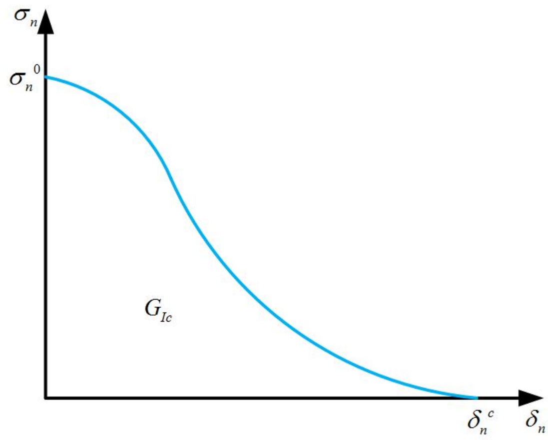


Figure 4.3: A generalized cohesive law relating tractions to displacements

### 4.2.1 Mode I cohesive law

Consider the DCB specimen with a crack, seen in section 3.5 - figure 3.5. Applying the $J$ integral on a path ($\Gamma_{loc}$) just around the cracked edges and the crack tip (figure 4.4). When the crack, initially free from bridging ligaments, is loaded. The crack will propagate when the evaluated $J$ - integral reaches the materials fracture energy $J_{loc} = J_0$.

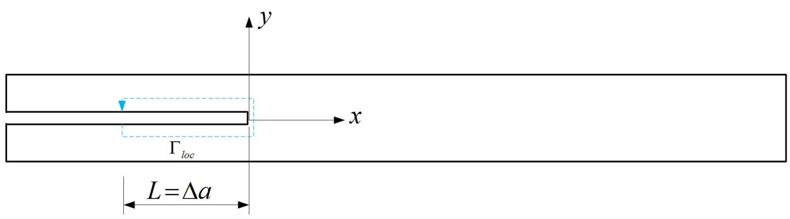


Figure 4.4: Integration path $\Gamma_{loc}$ around the cohesive zone

Were $J_0$ is the crack tip fracture energy. This is the energy which is required to make the crack propagate. Because of the path independence of the $J$ - integral Rice (1968), the $J$ - integral evaluated on the boundaries $\Gamma_{ext}$ as seen in section 3.5 is identical to $J_{loc}$. This means that:

$$J_{loc} = J_{ext} \tag{4.3}$$

During crack propagation, the fracture resistance $J_{loc}$ is denoted $J_R$. It increases until a steady state level $J_{ss}$ is obtained. This is when $\delta_n$ reaches $\delta_n^c$ and the crack at that point is completely separated. This level is not dependent on the thickness of the laminate but is a property of the given laminate (Suo et al., 1992). The area under the curve in figure 4.3 can be seen as the energy uptake in the fracture process and equals $J_{ss}$ which is equal (for single mode I) to the critical SERR $\mathscr{G}_{Ic}$.

The relation between the $J$ integral presented in equation 3.25 in section 3.4 and $\sigma_n$ is derived here:

The J integral in its original form is given as (Rice, 1968):

$$J = \int_{\Gamma} wdy - T_i \cdot \frac{\partial u_{ij}}{\partial x_{ij}} ds \tag{4.4}$$

Utilizing the path independence of the $J$ - integral, we use the path $\Gamma_{loc}$ (figure 4.4), which is located just around the cracked edge. Since $dy = 0$, $wdy = 0$ vanishes and hence the integral becomes (Bak, 2012):

$$J_{loc} = -\int_{\Gamma_{loc}} \sigma_{ij} n_j \cdot \frac{\partial u_i}{\partial x} dS \tag{4.5}$$

Splitting up the integral in two integration segments were the first is $x = -L \rightarrow 0$ and $x = 0 \rightarrow -L$ as:

$$J_{loc} = -\int_{-L}^{0} \sigma_n(\delta(x)) \frac{\partial u_2^-}{\partial x} dx - \int_{0}^{-L} (-)\sigma(\delta_n(x)) \frac{\partial u_2^+}{\partial x} (-)dx \tag{4.6}$$

Rewriting:

$$J_{loc} = \int_{-L}^{0} \sigma_n(\delta(x)) \frac{\partial u_2^+}{\partial x} dx - \int_{-L}^{0} \sigma_n(\delta_n(x)) \frac{\partial u_2^-}{\partial x} dx \tag{4.7}$$

And combining the two integrals:

$$J_{loc} = \int_{-L}^{0} \sigma_n(\delta(x)) \frac{\partial(u_2^+ - u_2^-)}{\partial x} dx \tag{4.8}$$

Expressing the separation of upper and lower cracked surfaces $(u_2^+ - u_2^-)$ as $\delta_n(x)$ the integral becomes:

$$J_{loc} = \int_{-L}^{0} \sigma_n(\delta_n(x)) \frac{\partial \delta_n(x)}{\partial x} dx \tag{4.9}$$

Substituting $\frac{\partial \delta_n(x)}{\partial x} dx = d\delta_n$. Hence changing the integration limits 0 and $-L$ with $\delta(x = 0)$ and $\delta(x = -L)$ we get:

$$J_{loc} = \int_{\delta(x=0)}^{\delta(x=-L)} \sigma_n(\delta_n(x)) d\delta_n \tag{4.10}$$

Substitution of the variables for $x = -L$ (Physical crack front) the integration limits will now be from 0 to the crack end opening $\delta_n^*$:

$$J_{loc} = \int_0^{\delta_n^*} \sigma_n(\delta_n) d\delta_n \tag{4.11}$$

Next the $J$ - integral for mixed mode loading is differentiated wrt. the crack opening components $\delta_n$ and $\delta_t$ in order to get the stresses. This is only shown for a mixed mode relation similar to single mode I or II.

### 4.2.2 Mixed mode cohesive law

In section 4.2.1 it was assumed that the tangential opening $\delta_t = 0$. But generally, the crack will most likely be subjected to some form of mixed mode loading. In this case restricting the mode mixity to modes between mode I and mode II. The derivation of the relation between $J$ - integral and the stresses and displacements are shown here.

Normal and tangential openings can be described as (Sørensen, 2010):

$$\begin{aligned} \delta_n &= u_2^+ - u_2^- \\ \delta_t &= u_1^+ - u_1^- \end{aligned} \tag{4.12}$$

Again the integration path is located just around the fracture process zone shown in figure 4.5 b).
In figure 4.5 b) the integration paths $\Gamma_{loc} = \Gamma_1 + \Gamma_{tip} + \Gamma_2$. Assuming $dy = 0$, and with the outward normals $n_1 = (0, -1, 0)$ and $n_2 = (0, 1, 0)$ as well as $dS = dx$ for $\Gamma_1$ and $dS = -dx$ for $\Gamma_2$ the integral gives:

$$J_{loc} = -\int_0^{-L} \sigma_{i2} \frac{\partial u_i^-}{\partial x} dx + J_{tip} + \int_0^{-L} \sigma_{i2} \frac{\partial u_i^+}{\partial x} dx \tag{4.13}$$

Collecting terms gives:

$$J_{loc} = \int_0^{-L} \sigma_{i2} (\frac{\partial u_i^+}{\partial x} - \frac{\partial u_i^-}{\partial x}) dx + J_{tip} \tag{4.14}$$

Combining eq.4.12 and eq. 4.14 gives:

$$J_{loc} = \int_0^{-L} \sigma_{12} \frac{\partial \delta_t}{\partial x} dx + \int_0^{-L} \sigma_{22} \frac{\partial \delta_n}{\partial x} dx + J_{tip} \tag{4.15}$$

Substituting the variables and inserting $\sigma_n = \sigma_{22}$ and $\sigma_t = \sigma_{12}$ gives:

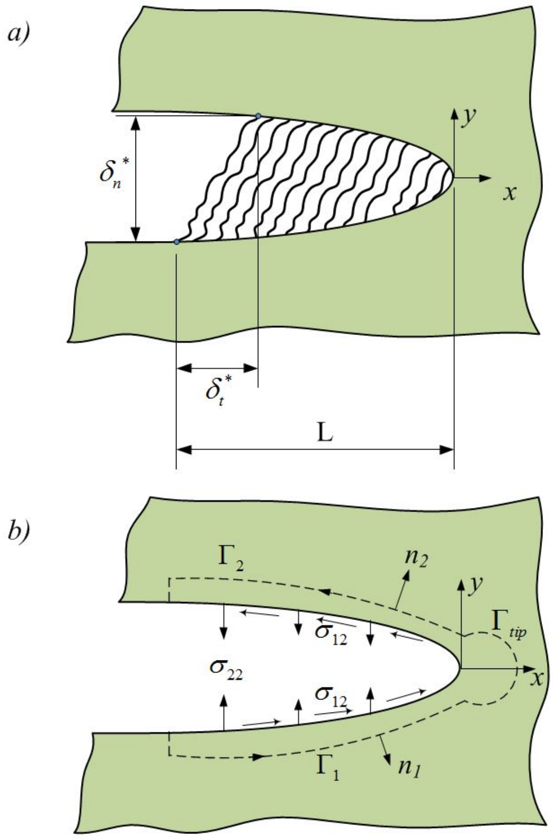


Figure 4.5: Crack subjected to mixed mode crack opening displacement. a) Normal and tangential end opening displacements and b) Definition of the J - integral path $\Gamma_i$.

$$J_{loc} = \int_0^{\delta_t^*} \sigma_t(\delta_n, \delta_t) d\delta_t + \int_0^{\delta_n^*} \sigma_n(\delta_n, \delta_t) d\delta_n + J_{tip} \tag{4.16}$$

First when the crack is initially unloaded $J_{loc} = 0$. Then when the crack is subjected to a load equal to the fracture energy of the material, the crack will propagate. This level is the initiation strength known as $J_0$, and is equivalent to the fracture strength for a non-bridged crack. This is occurring when $J_{loc} = J_0 = J_{tip}$. Then as the crack propagates further the energy uptake in the crack will be equal to the fracture resistance: $J_{loc} = J_R$ as described previously. This resistance increases until the crack will reach a certain length, were $J_R$ is constant at a steady state level, i.e. $J_R = J_{ss}$. At this point the cohesive zone is fully developed, and the crack will simply translate through the specimen as shown in figure 4.6.

Assuming a potential function $\Phi$ can be used to derive the cohesive tractions. The requirement is:

$$\Phi(\delta_n, \delta_t) \quad \wedge \quad \Phi(0,0) = 0 \tag{4.17}$$

Then according to (Kreyzig (2011) p. 423) the proof exists, that the potential exists for the integral $J_R$ if:

$$\frac{\partial \sigma_n}{\partial \delta_t} = \frac{\partial \sigma_t}{\partial \delta_n} \tag{4.18}$$

From this the cohesive stresses, which can be assumed as functions of openings $(\delta_n,\ \delta_t)$ within the cohesive zone, but independent of position, can be described by differentiating the potential with respect to the normal and tangential openings:

$$\begin{aligned} \sigma_n(\delta_n, \delta_t) &= \frac{\partial \Phi(\delta_n, \delta_t)}{\partial \delta_n} \\ \sigma_t(\delta_n, \delta_t) &= \frac{\partial \Phi(\delta_n, \delta_t)}{\partial \delta_t} \end{aligned} \tag{4.19}$$

Inserting eq. 4.19 into eq. 4.16 and integrating:

$$J_R = \Phi(\delta_n^*, \delta_t^*) + J_{tip} \tag{4.20}$$

Here $J_{tip} = J_0$ is the initial crack tip fracture energy as indicated in figure 4.6 a).

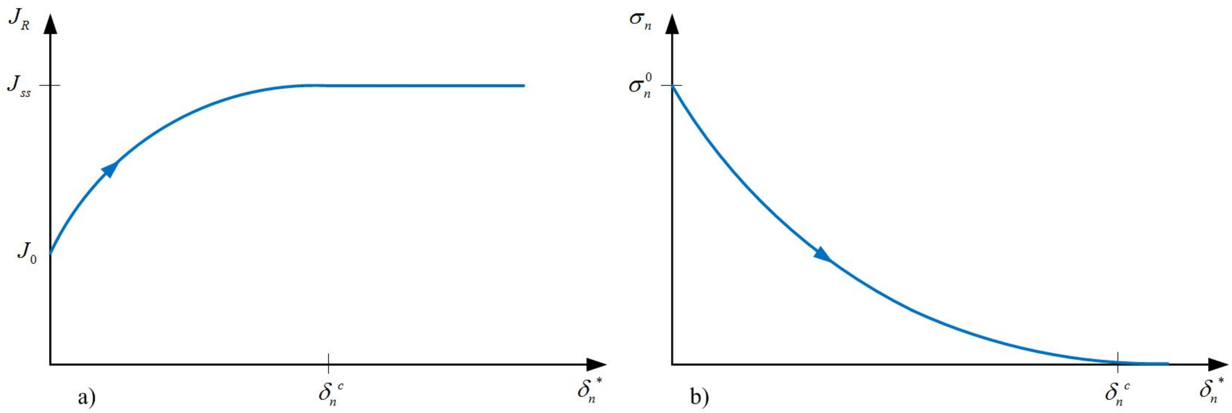


Figure 4.6: Illustration of a) the fracture resistance $J_R$ as function of opening $\delta_n^*$ and b) the cohesive tractions $\sigma_n$ as function of opening $\delta_n^*$

By combining equations 4.19 and 4.20:

$$\begin{aligned}\sigma_n(\delta_n^*, \delta_t^*) &= \frac{\partial J_R(\delta_n^*, \delta_t^*)}{\partial \delta_n} \\ \sigma_t(\delta_n^*, \delta_t^*) &= \frac{\partial J_R(\delta_n^*, \delta_t^*)}{\partial \delta_t}\end{aligned} \tag{4.21}$$

This implies that for mode mixity, the cohesive law is derived by measuring the end opening $\delta_n$, the end sliding $\delta_t$ and the applied moments $M_1$ and $M_2$ simultaneously. $J_R$ is found by utilizing the path independence of the $J$ integral, which means that $J_R = J_{ext}$ at any point in the load history. $J_{ext}$ for mode mixity is given in eq. 3.57 and reproduced here for clarity.

$$J_{ext} = \frac{21(M_1^2 + M_2^2) - 6M_1 \cdot M_2}{4H^3t^2E} \tag{4.22}$$

Differentiating the expression in eq. 4.22 wrt. the normal and tangential opening results in:

$$\sigma_n = \frac{\partial}{\partial \delta_n^*}\left(\frac{21(M_1^2 + M_2^2) - 6M_1 \cdot M_2}{4H^3t^2E}\right) \tag{4.23}$$

and

$$\sigma_t = \frac{\partial}{\partial \delta_t^*}\left(\frac{21(M_1^2 + M_2^2) - 6M_1 \cdot M_2}{4H^3t^2E}\right) \tag{4.24}$$

In practice this is done by obtaining data sets, for the recorded values, curve fitting the data to a polynomial and differentiating wrt. the opening. This is seen in chapter 8. Sørensen (2010) found good correlation between the following curve fit and test results performed for pure mode I (See figure 4.7):

$$J_R(\delta_n^*) = J_0 + \Delta J_{ss} \cdot \left(\frac{\delta_n^*}{\delta_n^c}\right)^{1/2} \tag{4.25}$$

Using eq. 4.21 to differentiate eq. 4.25 to obtain the curve fit for the stress displacement relationship:

$$\sigma_n(\delta_n) = \frac{\Delta J_{ss}}{2\sqrt{\delta_n^c \delta_n}} \tag{4.26}$$

Sørensen and Jacobsen (1998), showed through the use of micro-mechanic beam solutions that there is no decoupling of the cohesive laws for mode mixity. A short introduction to micro mechanic solutions for mode I and mode mixity is given in appendix D, where this is explained.

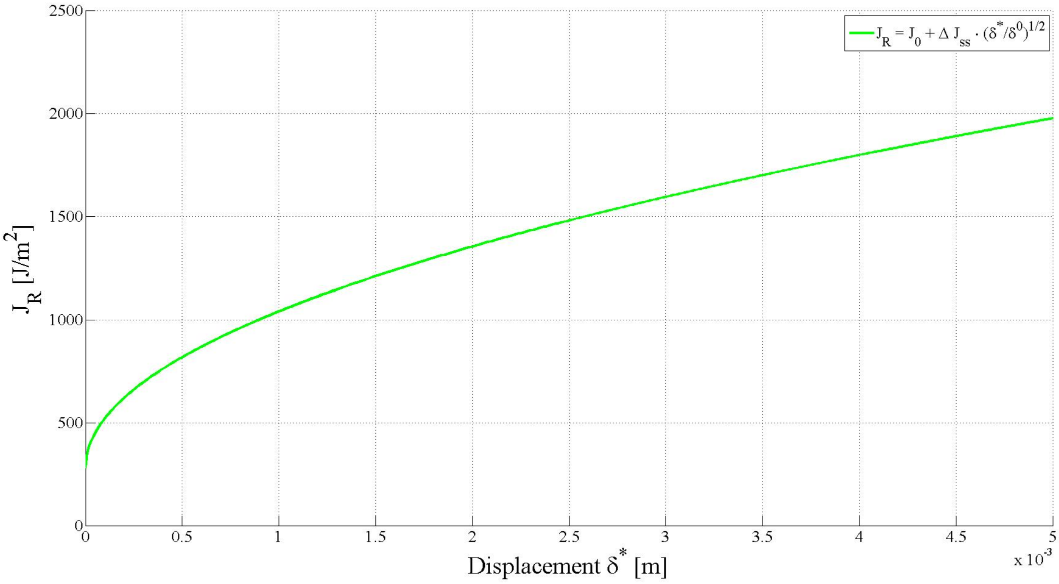


Figure 4.7: Curve fit that fits test results well (Sørensen, 2010)

## 4.3 Fitting cohesive properties to failure criteria

Different propagation criteria for delamination of fiber reinforced composites exist. Some are for example the widely used power criterion (Camanho and Davila, 2002) and the BK - criterion (Benzeggagh and Kenane, 1996). These are discussed in detail in appendix C. The BK criterion, shown in eq. 4.27 can be seen as an interpolation criterion that interpolates the fracture strength between modes I and II.

$$\mathscr{G}_{Ic} + (\mathscr{G}_{IIc} - \mathscr{G}_{Ic})B(\beta)^{\eta} = \mathscr{G}_c(\beta) \tag{4.27}$$

In order to obtain $\mathscr{G}_c(\beta)$, tests must be made to evaluate the critical energy release rates for mode I, mode II and for different mode mixities $\beta$. Then a parameter $\eta$ is found by fitting a line through the points created in a $\mathscr{G}_c - B(\beta)$ coordinate system. Where $B(\beta) = \frac{\mathscr{G}_{shear}}{\mathscr{G}_I + \mathscr{G}_{shear}}$). The energy release rates for various mode mixities for the carbon epoxy prepreg AS4/3501-6 and carbon- thermoset IM7/977-2 as well as the B-K citeria applied to them are seen in figure 4.8. The data are from the work by Camanho and Davila (2002).

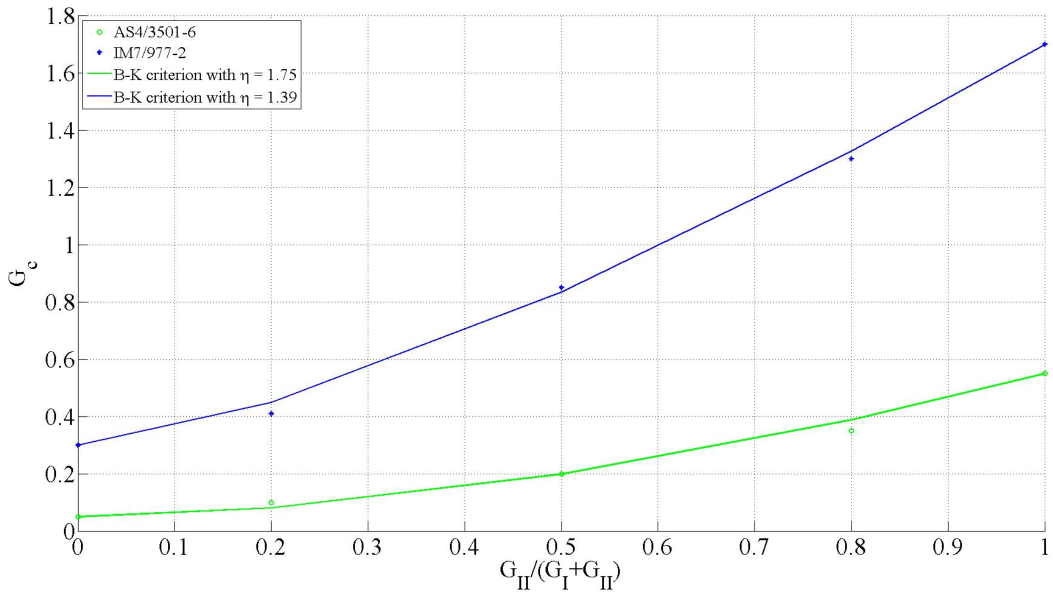


Figure 4.8: B-K criterion fit using the parameter $\eta$ for two materials

## 4.4 Conclusion

The cohesive concept is presented, based on the model by Barenblatt (1961). The cohesive law for mode I loading is derived obtaining the $J$ - integral around the crack tip as a function of the normal opening of the crack. Then using a traction potential the relation between tractions and displacements are shown for a mixed mode crack. Because of the path interdependence of the $J$ - integral, the $J_{loc}$ can be set equal to the previous calculated $J$ - integral for a path surrounding the entire body $J_{ext}$. Then by curve fitting the obtained data to a $J-\delta$ diagram, the tractions can be found by differentiating the polynomial obtained from the curve fit.

# Part II

# Development of the test tool

# Chapter 5

# Concept development

## 5.1 Introduction

The development of the test tool to test the cohesive properties of a DCB specimen is of paramount importance in this project.

This chapter is divided into a *discussion about load input*, and the importance of pure moment application. In order to understand the different methods that have been developed over the past 25 years a presentation of previously developed test methods are given in appendix A . An overview is given of the individual methods including their advantages and drawbacks compared to testing layered fiber composites as in the current case. For the test setup created by Bent Sørensen and his team, the method is analyzed in detail using free body diagrams.
In order to find the best solution amongst the concepts a *requirement analysis* is presented, which is showing the requirements the test tool must be able to fulfill. Different concepts have been developed and can be found in Appendix B. In the appendix, the concept that fulfills all requirements as well as is given the best grade based on a set of criteria, is chosen. The chosen concept is shown, and the details of the final design are presented.

## 5.2 Discussion about load input

One of the most used methods to test DCB specimens is the wedge method, for mode I DCB testing. A sketch of the test method can be seen in figure 5.1.
This method has been standardized by ASTM (ASTM, 2007) and ISO 15024:2001 International Standard (2001). It is used to a high extent because it is easily used

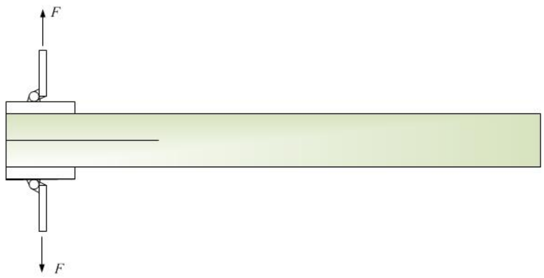


Figure 5.1: The wedge method for pure mode I testing

and adaptable to most standard tensile test machines. For mode II and mixed mode testing there are also standards available that uses a combination of a three point flexure testing device and the wedge method presented above. In figure 5.2 a sketch is shown for the by ASTM standardized apparatus that is used in for instance the paper by Xie and Waas (2006). This apparatus can test smaller specimens from nearly pure mode I to pure mode II, simply by applying a force $P$. However the method is not the most favorable method, because it is displacement controlled, which does not yield constant crack growth, because the energy release rate $\mathscr{G}$ is then depending on the crack length (Sørensen et al., 1996) as described in the introduction.

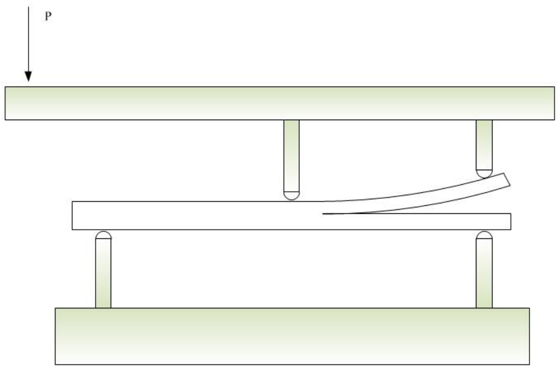


Figure 5.2: Mixed Mode Bending test method

Further complications with the wedge test method is also that the specimens need to be quite thin. The ASTM standard (ASTM, 2007) recommends specimens, not thinner than $2H = 3mm$ and not thicker than $2H =$ 5mm. This in turn means that data cannot be obtained for thick specimens, were for instance residual stresses due to hardening processes or other influences are taken into account. A remedy to this has been proposed by (Jacobsen and Sørensen, 2001). Here the opening angle must also be measured, so that the $J$ - integral gives:

$$J = \frac{2P\theta}{t} \tag{5.1}$$

$t$ is the width of the specimen, $P$ the applied force and $\theta$ the end rotation (see figure 5.3). However it can be difficult measuring crack length and in addition the rotations precisely using an inclinometer at a specific location of the two beam ends. The reason why this approach is more precise than the LEFM approach is because the fiber bridging mechanism prevents rotation of the beams. This is not accounted for using the LEFM approach as one of the assumptions is that the fracture process zone is small compared to other specimen dimensions as shown in section 3.8. Sørensen and Jacobsen (2000) showed the difference between using the $J$ - integral approach vs. using LEFM, were the main conclusion is that the LEFM method "Overshoots" the $J_R$ curve for shorter initial crack lengths. Despite using this approach, it is still difficult to obtain stable crack growth, due to the test being displacement controlled.

### 5.2.1 Influence of the initial crack length

Here the influence of the initial crack length $a_0$ is shown for the wedge method. Assuming that the fracture process zone $a$ is small (see figure 5.3) as indicated above. The energy release rate according to LEFM is written as (Andreasen, 2010):

$$\mathscr{G}_I = \frac{P^2 a_0^2}{tEI} \tag{5.2}$$

An analytic expression for the displacement of the beam end can be written as (Gere and Goodno, 2012):

$$\delta_A = \frac{2Pa_0^3}{3EI} \tag{5.3}$$

Where point A (figure 5.3) is located at the crack tip. Isolating $a$ from eq. 5.2 and inserting into eq. 5.3 and assuming that $\mathscr{G}_I = \mathscr{G}_{Ic}$, gives an analytic expression for the relation between separation at A and force applied as:

$$\delta_A(P) = \frac{2\left(\mathscr{G}_{Ic} tEI\right)^{3/2}}{3EIP^2} \tag{5.4}$$

For the elastic part, where $\delta_n^* \leqslant \delta_n^0$, the crack length $a_0$ in equation 5.2 is fixed. When the crack starts propagating, i.e. $\delta_n^* \geqslant \delta_n^0$ then eq. 5.4 governs. This can be seen in figure 5.4. Specimen data used are: $H$ = 3.8mm, $a_0$ = 30mm and 60mm, $t$ = 22mm, $E$ = 37GPa and $\mathscr{G}_{Ic} = 0.5N/mm$.

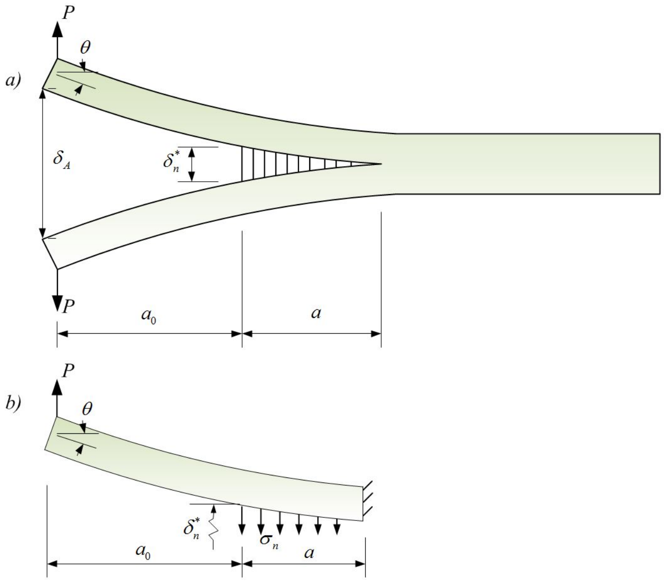


Figure 5.3: a) DCB specimen subjected to wedge forces, b) simplified DCB specimen arm, were the bridging tractions are replaced by a uniform traction $\sigma_n$

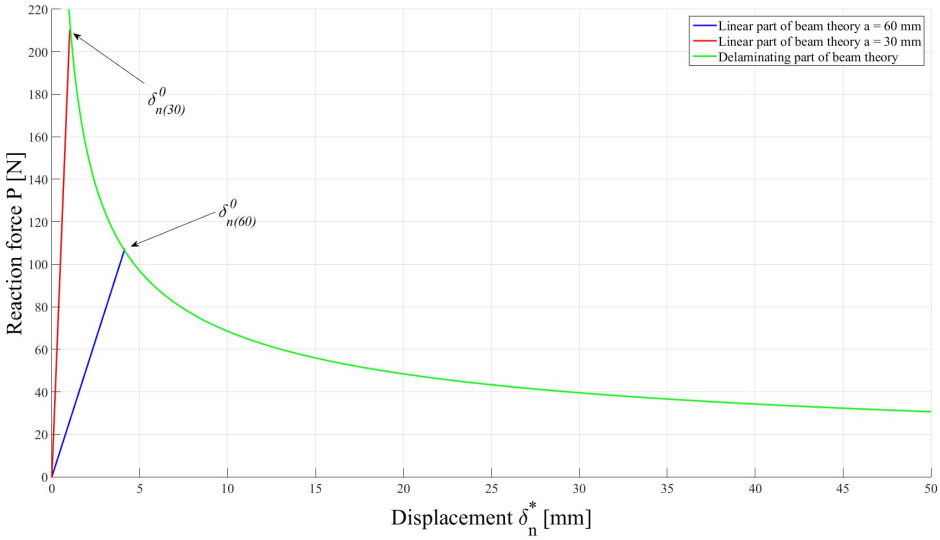


Figure 5.4: The force reaction is plotted vs. the end displacement for the wedge method subjected to pure mode I

Using pure moment applied to the two beam ends, it was shown in chapter 3, that the difficulties concerning measuring the crack length can be avoided as the energy release rate $\mathscr{G}$ is independent of the crack length under constant or fixed loads. This makes the measurement of $\mathscr{G}$ easy compared to the method outlined by (ASTM, 2007). In the following hence only pure moment application is considered.

## 5.3 Requirement specification

Here the requirements towards the new test tool is specified. The specifications build on utilizing the principle of applying pure moment to the free ends of the specimens in order to obtain Modes I through Mode II and Mixed Mode ratios in between. Mode I opening is seen in figure 5.5a. Mixed mode crack opening is seen in figure 5.5b.

The requirements are paramount to the function of the test tool and no exceptions from them can be made when evaluating the concepts that are presented in appendix B. If any of the concepts presented do not fulfill the following requirements, they will be deemed useless, and will not be developed further in detail:

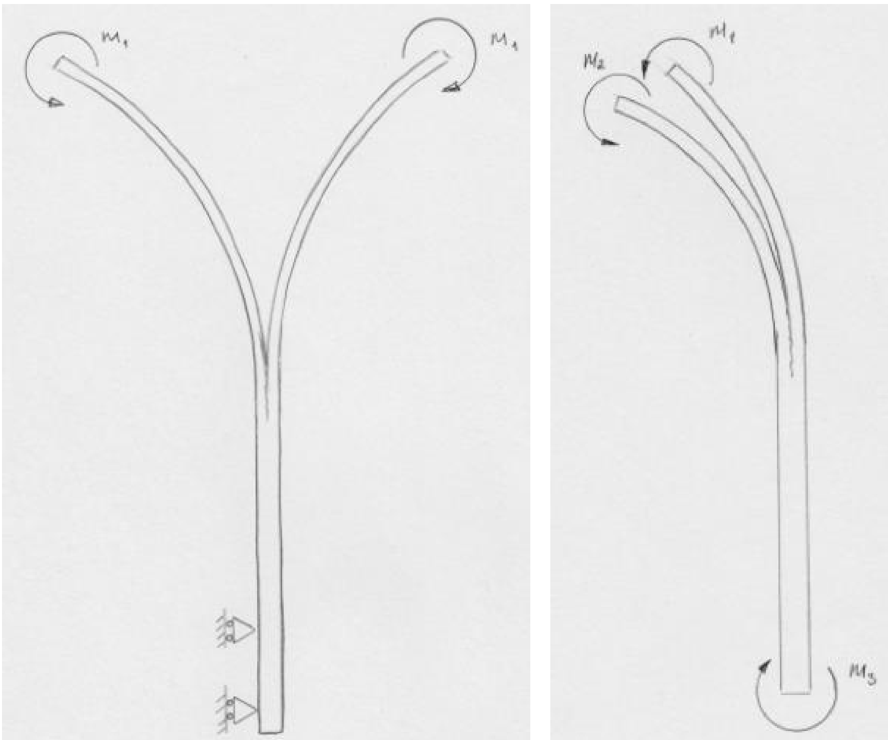

(a) (b)

Figure 5.5: Illustration of Pure Mode I, and Mode mixety

- Pure moment application. The test tool in the concept must be able to subject the specimen to pure moment, so that crack opening modes, ranging from pure mode I to almost pure mode II can be obtained. The requirement "Almost pure mode II" is used as recent research has shown that under pure mode II loading a normal opening of the crack will exist. This is assumed to be due to roughness of the crack interfaces (Sørensen and Goutianos, 2014).

- The test tool should impose as small shear and normal loads to the specimen as possible in the process, when the specimen opens with a mode I crack or is bend in a mixed mode crack condition.
- It must be able to be used with a standard tensile test machine with a window opening of approximately 600 $mm$ $x$ 400 $mm$
- The test tool must be able to withstand the loads that is subjected to during the static testing process as well during fatigue analysis.
- The test tool must be able to restrain the specimen correctly in any load case. I.e. when the specimen is subjected to a mixed mode scenario as shown in figure 5.5b, it must be able to support the moment $M_3$ as shown.
- The tool must support specimens sizes ranging from (*2H x t x L*) 5 $mm$ $x$ 20$mm$ $x$ 200 $mm$ up to 50 $mm$ $x$ 30$mm$ $x$ 800 $mm$.
- Frictional forces in the test tool must be small enough to be negligible.

## 5.4 Chosen concept

From the developed concepts, that are shown in appendix B, the concept presented here (Concept 5) had the highest score, based on the criteria that was listed in the appendix.

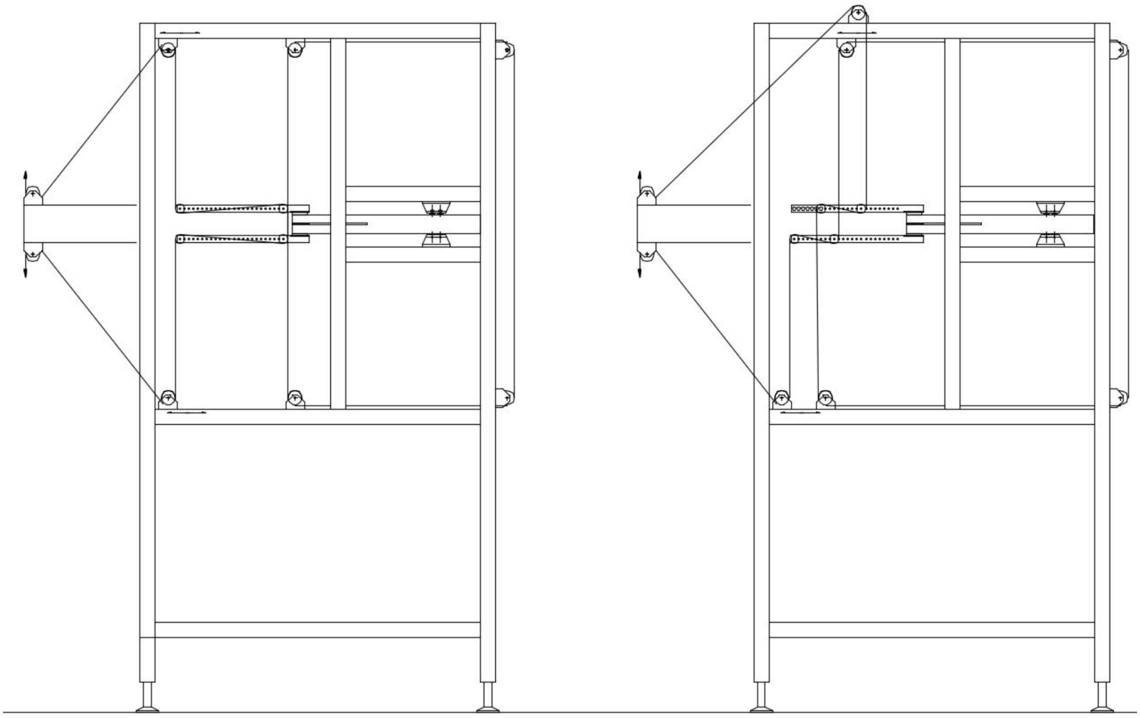

Figure 5.6: Concept 5 Mode I and Mode II setup

The concept shown in figure 5.6, is based on applying loads to the moment arms using wires. The main difference between this setup and the one shown in appendix A by Bent Sørensen and his team, is that the moment arms are oriented parallel with the specimen. This means that when the specimen opens and the moment arms rotate. The angle of the wires will be subjected to secondary effects of the vertical displacement of the moment arms. This is illustrated in figure 5.7. Here the relation between the rotational angle and the horizontal displacements is:

$$u_{x1} + u_{x2} = s \cdot (1 - cos(\theta)) \tag{5.5}$$

Despite the simple relation it is not a trivial task to determine $u_{x1}$ and $u_{x2}$ individually as they are dependent on the friction in the roller support and the wire length. I.e. there are infinitely many solutions.

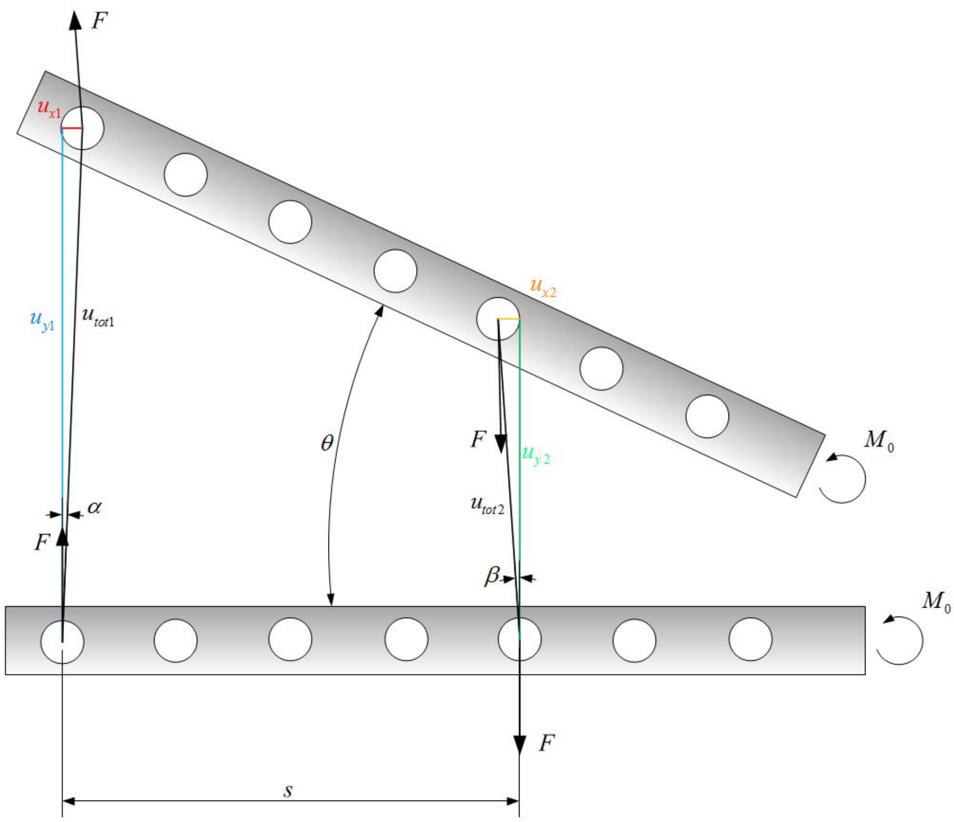


Figure 5.7: Rotational angles and displacements of a moment arm

### 5.4.1 Comparison with the test rig concept by B.F. Sørensen

The test rig concept made by Bent Sørensen and his team (Sørensen and Jacobsen, 1998) is analyzed in depth in appendix A.2.3. This shows that determining the actual moment input to the test specimen is highly depending on that the wires are very long. I.e. small angular displacements of the wires. Further it requires that the opening of the specimen is small. The later implies using thick specimens for testing. Comparing the mentioned test rig to the proposed concept, this concept has the clear advantage that shorter wires can be used, and that the opening of the specimen (rotation during mode II) does not influence the rotation of wires as much as the existing rig. Using shorter wires, it is assumed that the test rig is able to support fatigue analysis to a certain degree. A detailed analysis of the chosen concept is presented in section 6.2.

## 5.5 Detailed development

In the following sections the details of the test tool is presented. First the details about the design of the frame structure is discussed. Then the wire rollers are presented. followed by the roller support structure. Finally the moment arms are presented. Calculation of natural frequency, for the frame, as well as static and fatigue calculations for the different parts are found in appendix E. The entire system including the wire path can be seen in figure 5.8b. But first the suitable wire is chosen.

### 5.5.1 Choice of wire

In order to apply the forces, a suitable wire is chosen. Several different methods were considered. First a set of requirements were listed, which are:

- Must have a relatively high modulus of elasticity, in order to be able to perform fatigue studies, and so that there is a close relation between displacement of the test machine cross head and opening of the specimen.
- High breakage strength. Wire loads up to 2500 N can be applied for the largest specimens, according to appendix E.
- Lightweight - The wire should be as light as possible in order not to influence the results.
- Compliant when bend - The wire should be easily bend around the rollers without much resistance and it must be bendable around all axises. Furthermore it should keep its shape during deformation and under load.
- Low friction - the wire should result in low friction when in contact with the rollers.

First material considered was strip steel (**SS**) Sandvik 12R11, with a width and thickness of 10 x 0.25 mm. It is very strong with a fracture strength of 1700 MPa and has a modulus of elasticity corresponding to that of regular steel. The drawback is that it can only be bend about one axis, and is therefore not suitable to the current concept.

Secondly, thin steel wire (**SW**) was considered. However, when choosing small diameters, 1.5 mm for instance where the weight is low and the bending compliance is high. There is a high level of friction between the roller and wire - which can lead to wear during fatigue analysis.

The third option considered was rope. Here different types of ropes were considered. First, Dyneema line - Ocean 7000 (**O7**) with a breaking strength of 11.7 kN for a Ø3 mm rope was considered. This however did not work as it did not retain its shape when bend around the roller. Next sleeve type ropes were considered Globe 5000 - Ø4 mm (**G5**), but they were to stiff when bend. Lastly Dyneema downhaul line - Ø3.8 mm (**DH**) was considered. The fracture strength is approximately 8 kN. It is very smooth, compliant when bend and keeps its roundness during heavy loading. As an option for smaller specimen, Dyneema line - Ocean 3000 (**O3**) was considered in a 2 mm thickness option. This line does as the thicker Ocean 7000 line not keep its roundness when loaded, but this can be neglected due to its small size.

The different materials considered and their data can be seen in table 5.1

| - | SS | SW | O7 | O3 | G5 | DH |
|---|---|---|---|---|---|---|
| Weight [g/m] | 19.625 | 11 | 5.5 | 2 | 7 | 8.5 |
| Breaking strength [kN] | 4.25 | 2.09 | 11.7 | 4 | 6.8 | 7.8 |

Table 5.1: Rope materials

The chosen wire for larger loads is the Downhaul line. With relatively low weight, compliant when bend, good strength and stiffness as well as smooth surface that reduces friction. For small test specimens, the O3 rope is the solution that fits the requirements best.

### 5.5.2 Frame structure

The purpose of the frame is to separate the rollers, and transfer loads between the specimen and the test machine and floor. The frame can either be welded or bolt assembled using standard RHS profiles. But this would require large changes when the setup is changed. For instance when large DCB specimens are to be tested, the upper rollers must be adjusted so that the distance between the upper rollers, and the specimen is the same to the corresponding lower rollers. Therefore a flexible system using aluminum profiles is chosen. This system allows for quick changes as profiles are connected through groves using T-bolts. This also allows for flexible adjustment of the position of the rollers and other equipment. The frame structure can be seen in figure 5.8b.
The frame structure has been subjected to both static analysis using finite element analysis using a 3D beam model, with the specific cross section data applied. The loads that have been applied, corresponds to 5 kN load applied to the wire set. The maximum equivalent von Mises stresses found were approximately 41 MPa. Further a natural frequency analysis has been performed. This shows that the lowest natural

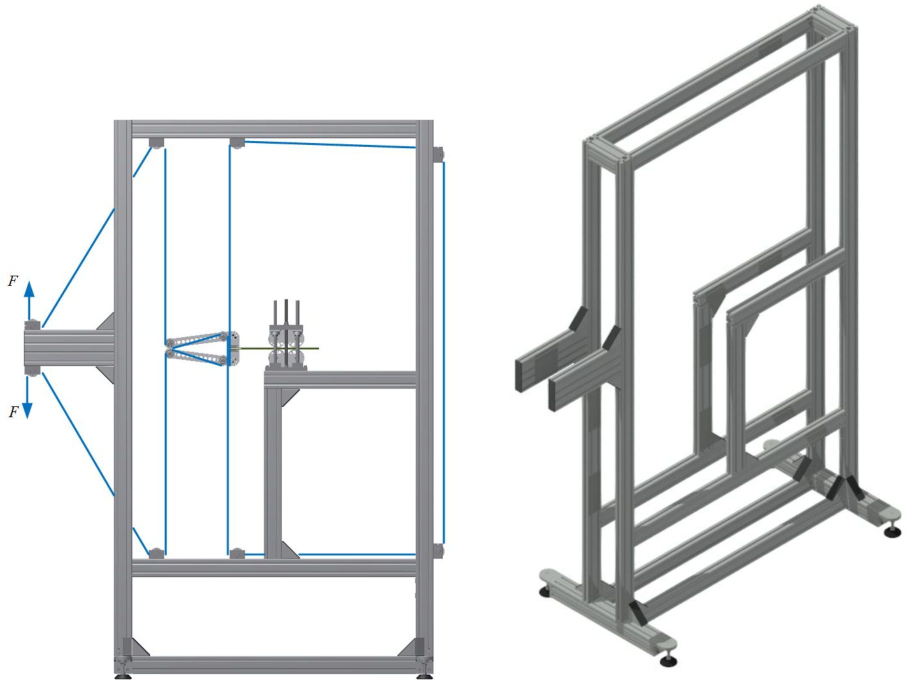


(a) (b)

Figure 5.8: a) Wire path around the system, with small specimen installed and b) the frame structure seen in isometric view

frequency is approximately 8 Hz. The input file for Ansys APDL, can be found on the accompanying DVD. A resume of the FEM calculation is given in appendix E.

### 5.5.3 Wire rollers

The wire rollers guiding the wire around the system are seen in figure 5.9. They are constructed using a solid Ø25 mm shaft, with two low friction bearings type SKF-E2-6005-2Z, and a guide roller made of aluminum on the outside. The strength of the roller assembly is calculated in appendix E.

### 5.5.4 Roller support structure

The roller support structure, seen in figure 5.10 is build with an upper and lower part. The lower part is connected to the frame using four T - bolts. The upper part can be adjusted by changing the position of the four M12 nuts on the two threaded rods. Four nuts are used in order to position the upper part so that it barely touches the specimen. The 12 wheels, running on 4 individual shafts, are fitted with ultra low friction bearings from Ceramic speed. There is one bearing per wheel, in order to ensure minimum of friction due to fabrication tolerances. The wheels

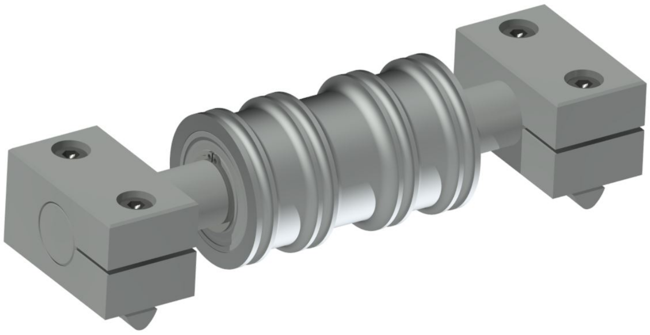

Figure 5.9: Wire rollers

are manually optimized in order to minimize the mass moment of inertia about the rotational axis, and still posses enough strength to support the largest specimens. Two compressional springs are inserted on the top part to reduce the clamping stiffness. During mixed mode loading or mode II, the specimen is pushing upwards on the upper - rear wheel set. If there are small height differences on the specimens - the springs will allow the translation in this position easier. Furthermore they ensure that the nuts stay in their position during fatigue loading of the specimen.

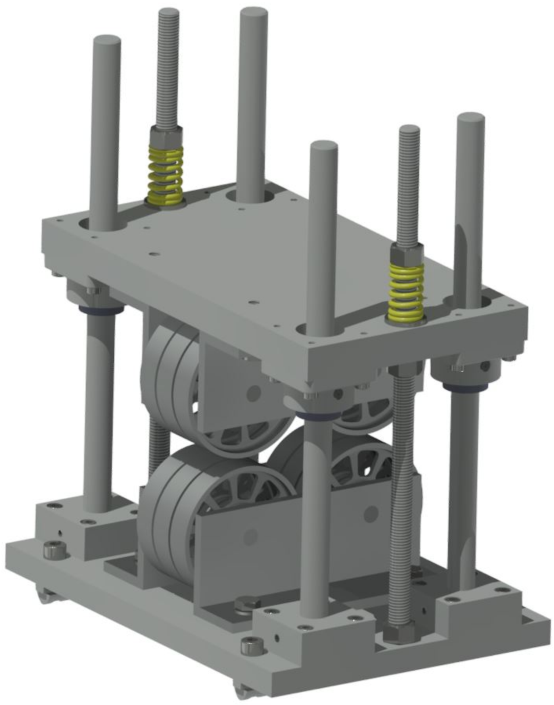

Figure 5.10: The roller support structure

The strength of the roller support structure is calculated in appendix E

### 5.5.5 Moment arms

Two different configurations of moment arms, have been developed. The smaller configuration (shown in figure 5.11) is used for specimens with a height up to $2H = 30$mm and thickness up to $t = 25$mm. The larger configuration (not shown) is used for 30mm $\leqslant 2H \leqslant$ 50mm and thickness up to $t = 30$mm. They are designed so that the distance between the rollers can be adjusted with a distance of 20 mm in order to create different mode mixities. The moment arm is connected to the specimen using a special bracket, that is glued or screwed into the specimen, depending on the height $H$ of the moment arms. Thinner specimens are glued, larger are screwed. The bracket is connected to an interface, that allows the moment arm to be positioned $\pm 10°$ with 2.5° jumps. This helps reduce the variation of moment when the moment arm rotates. This is further discussed in section 6.1.

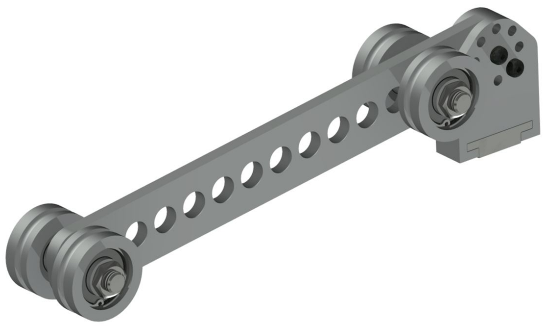

Figure 5.11: The small configuration of the moment arms

The dead load of the moment arms is balanced out using a simple roller system. The wire, running over a roller is connected to one of the holes in the moment arm, so that it is in balance. Then a counterweight is connected to the other end of the wire. The response time of this system, when fatigue analysis is performed, is assumed to be the same as the rest of the wire system in the structure. The moment arm assembly is verified in appendix E for both static as well as fatigue loading. For fatigue loading the dimensions of the specimens tested should be smaller as the strength is greatly reduced. Using the large moment arms and mode I loading, the specimen height should not exceed 2H = 28 mm and t = 25 mm. For mode II; 2H = 12 mm and t = 25mm.

## 5.6 Conclusion

In this chapter the arguments for using pure moments are given based on that it can be difficult to capture the crack length as the crack propagates. Jacobsen and Sørensen (2001) introduced a method to use the $J$ - integral approach with the wedge method, by measuring the opening angle. However problems exists, as it is not straight forward to measure the angle. Furthermore it will still result in unstable crack propagation. Then a requirement specification is given, followed by a comparison between the chosen concept and the test rig by B.F. Sørensen and his team. Here it was seen that the proposed concept uses shorter wires, which might make it more applicable to fatigue testing. Also orienting the moment arms parallel to the specimen results in smaller rotations of the wires, which makes the errors in spurious shear forces smaller. Finally the details of the new test tool are presented.

# Chapter 6

# Validation of moment application

## 6.1 Introduction

In order to verify that the force, introduced from the test machine, is converted into the expected moment, a device has been fabricated, which can be seen in the two figures below:

(a) 3D model

(b) Device fitted with strain gauges

Figure 6.1: Test device

The device consists of two moment arms that are 5 x 22 mm flat steel bars. These bars are connected in one end, in order to simulate a DCB specimen with a long crack. The bars are fitted with two strain gauges each to form two individual Wheatstone half bridge setups. These strain gauges then measure the strain in the bars directly, and the moment in each of the bars can be calculated and verified individually.

First the setup is evaluated analytically, then the strain gauge and load cell test results are presented, followed by finite element analysis of the test specimen and finally the DIC results are presented.

## 6.2 Analytic determination of the influence of angles and rotations

When one of the DCB specimen arms rotate, as the crack grows, the horizontal distance between the rollers is getting shorter. This means that the specimen will move on the rollers. This is illustrated below in figure 6.2.

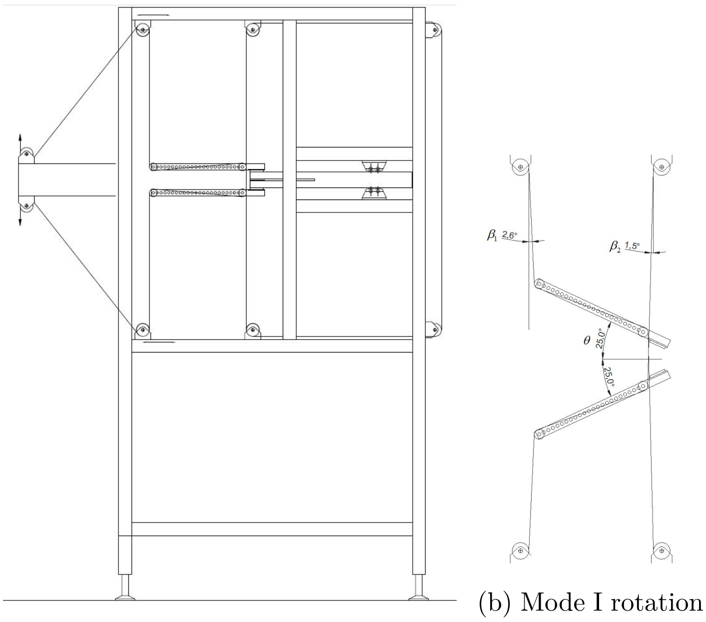


(a) Final Concept - Mode I

(b) Mode I rotation of moment arms

Figure 6.2: Overview of the final concept for mode I

For instance if the moment arms, with an initial horizontal distance $L_0$, are subjected to mode I opening, and rotate 30 degrees, the horizontal distance $L$ is now 260 mm. This is shown in figure 6.3.

I.e. the specimen should in the optimum situation move 20 mm, to get into equilibrium, with angles $\beta$ and $\alpha$ being equal (figure 6.5). This means that the two vertical wires would rotate equally and be at an angle of approximately 2.2°.

Distributing the angles evenly is not possible, since one of the wires is longer than the other as seen in figure 6.2a. Furthermore, the distribution of distances $u_{x1}$ and $u_{x2}$, as mentioned in chapter 5, is highly dependent on the frictional resistance in the roller support structure. Therefore it is not possible to calculate the rotational angles $\alpha$ and $\beta$ analytically.

The equilibrium conditions for the rotated moment arm, is shown as:

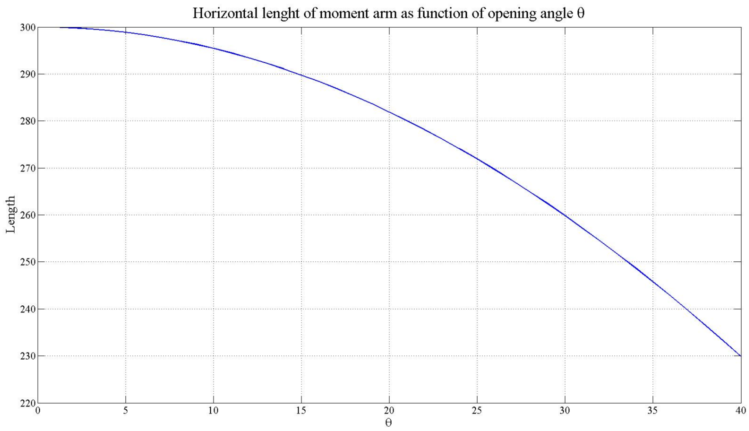


Figure 6.3: Horizontal lenght between rollers $L$ (Figure 6.6)

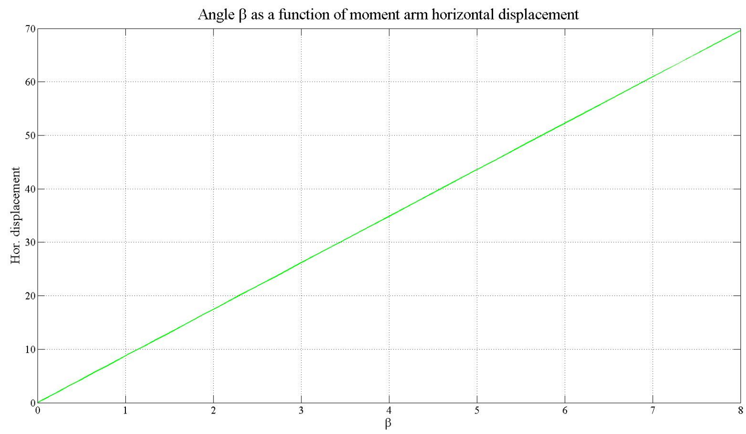


Figure 6.4: Vertical angle as function of rotation

$$N = F\cdot sin(\theta + \beta) - F\cdot sin(\theta + \alpha) \tag{6.1}$$

$$V = F\cdot cos(\theta + \beta) - F\cdot cos(\theta + \alpha) \tag{6.2}$$

$$M = F\cdot cos(\theta + \beta)\cdot (a + b) - F\cdot cos(\theta + \alpha)\cdot b \tag{6.3}$$

In the worst case, with very thin specimens, the maximum rotation of the DCB specimen arms is assumed to be 40 degrees from horizontal. This gives a shortening of the horizontal distance between rollers of 70 mm (seen in figure 6.3). In turn, assuming that the specimen is moving horizontally in the roller support, so that $\beta = 0°$ and $\alpha$ is non-zero. Then this would results in an angle of $\alpha = 8°$ (seen in figure 6.4). Using a unit force ($F = 1N$), and the distances $a = 1m$ and $b = 0.1m$, the equations above lead to:

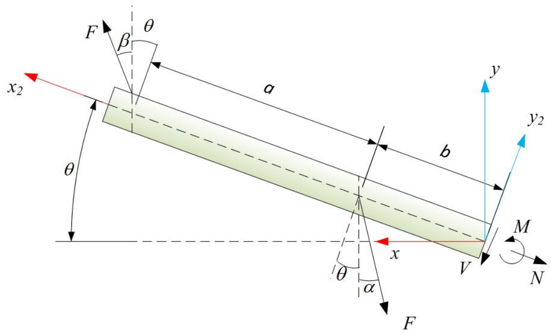


Figure 6.5: Free body diagram of moment arm rotated

$$N = 0.1N \tag{6.4}$$

$$V = -0.1N \tag{6.5}$$

$$M = 0.66Nm \tag{6.6}$$

This shows that the normal and shear forces, in the worst situation will vary a maximum of 10%. The moment on the other hand, which should be 1 Nm, is primarily depending on the rotational angle $\theta$, and not affected much by the angles $\beta_1$ and $\beta_2$. This is because the horizontal distance $L$ is affected a lot by the rotation $\theta$ as seen in figure 6.6.

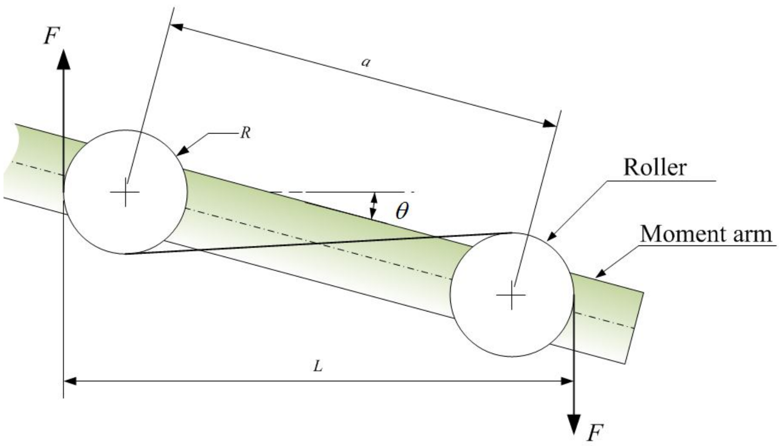


Figure 6.6: Relation between length $L$ and angle $\theta$

The relation between the length $L$ and the rotational angle $\theta$ is calculated as follows:

$$L = 2R + a \cdot cos(\theta) \tag{6.7}$$

This must be considered for the tests. Increasing the ratio between $a$ and $b$, with

$a >> b$, reduces the error in moment as can be seen from eq. 6.3. I.e. when $a >> b$, then the term $(a + b) \cong a$. This means that the moment is calculated as:

$$M = F \cdot L = F \cdot (2R + a \cdot cos(\theta)) \tag{6.8}$$

Using the possibility of presetting the moment arms opposite to the rotation direction. As for instance setting the moment arms $-10°$, if the opening is expected to be $+20°$. The maximum error will be $\approx 1.5\%$, which is acceptable.

## 6.3 Strain gauge and load cell results

The strains measured in the strain gauges, can easily be transformed into the moment through the use of ordinary beam theory (Bernoulli Euler) as

$$M = -\frac{\sigma_{xx} I_{zz}}{y} \tag{6.9}$$

Using Hooke's law, i.e. $\sigma_{xx} = E\epsilon_{xx}$ and the moment of inertia $I_{zz} = \frac{1}{12}tH^3$ and inserting into 6.9 we get:

$$M = -\frac{1}{6}E\kappa\epsilon_{xx}tH^2 \tag{6.10}$$

Here the bridge constant is $\kappa = 2$. The thickness of the arms are $t = 22$ mm, and the height is $H = 5$ mm. Hence the moment is calculated based on measured strains as:

$$\boxed{M = 0.0385 \cdot \epsilon_{xx}} \tag{6.11}$$

Here a factor of $10^{-9}$ is included, due to measuring $\frac{\mu m}{m}$ and converting the moment into $[Nm]$. The moment $M$ is then converted to force as follows:

$$F = \frac{M}{L} = \frac{E\kappa\epsilon_{xx}tH^2}{6(2R + a \cdot cos(\theta))} \tag{6.12}$$

Here $a$ is the distance between the holes in the moment arm (see figure 6.6) and $R$ is the radius. For $L = 72\text{mm} + 2 \cdot 23\text{mm} \cdot cos(\theta)$ and using the above constants, eq. 6.12 gives the force in the wire couple, which is measured by the test machine. I.e. the wire itself will only be subjected to $F/2$. Thus the conversion factor can be assumed as:

$$\boxed{F = \frac{19.25 \cdot \epsilon_{xx}}{36 \cdot cos(\theta) + 23}} \tag{6.13}$$

Using this setup, it is unfortunately not possible to test for spurious shear forces or normal forces. This was evaluated analytically and will be compared with DIC on the same sample, which is seen in section 6.5.

The strains measured, with the test specimen installed, is compared with the force measured by the load cell in the test machine. This is seen in figure 6.7. Furthermore eq. 6.13 is introduced with $\theta = 0$. This shows that for the actual rotation, which was measured to be approximately 15° in the end of the test, that the error by neglecting $\theta$ is small (5 N). This is in good correspondence with the analytic calculations shown in section 6.2.

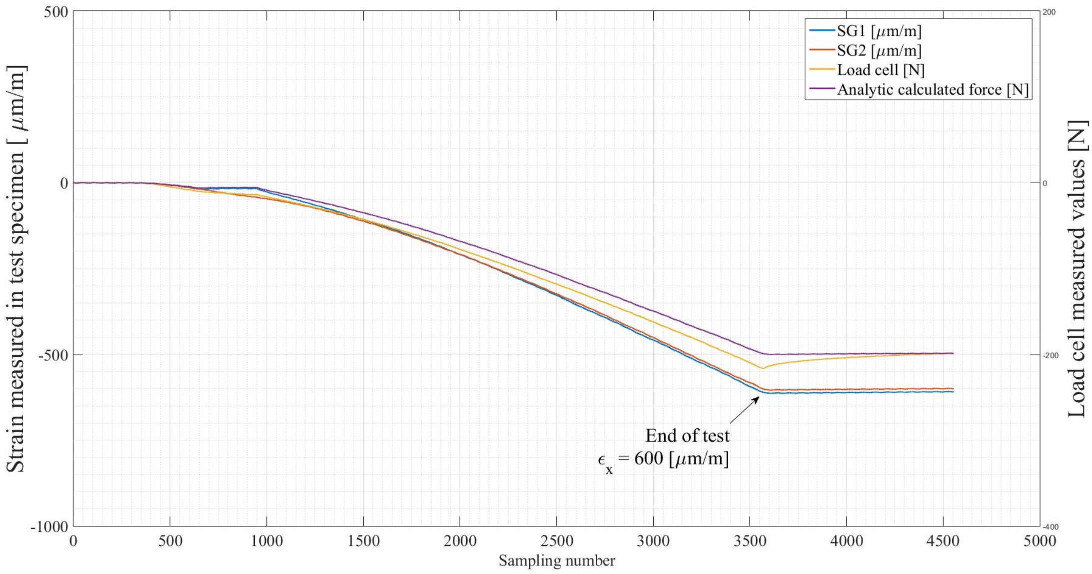


Figure 6.7: Load cell and strain gauge values during the test

## 6.4 FEA of test device

In order to analyze which loads can be applied to the test specimen, a small FE analysis has been performed of the device. Only one of the arms are modeled. It is analyzed as a 2D plane stress analysis applied with a maximum of 30 Nm of moment and the other end is restricted in all dof. This would result in stresses near the yield limit. The results can be seen in figures 6.8 to 6.10. The material the device is made of is EN10025 S355J2G3, with a specific minimum yield strength of 355 MPa. This is not to be exceeded. The deformations are compared with ordinary beam theory as:

$$\delta = \frac{M \cdot L^2}{2E \cdot I} = 24.75mm \tag{6.14}$$

Were $\delta$ is the displacement of the end, $M$ = 30Nm is the applied moment, $E$ = $200 \cdot 10^3$ MPa is the Young modulus, and $I$ is the moment of inertia of the beam. Comparing it to the FE results as seen in 6.10, the difference is 0%, which is acceptable.


Figure 6.8: Boundary conditions of FE model of the device

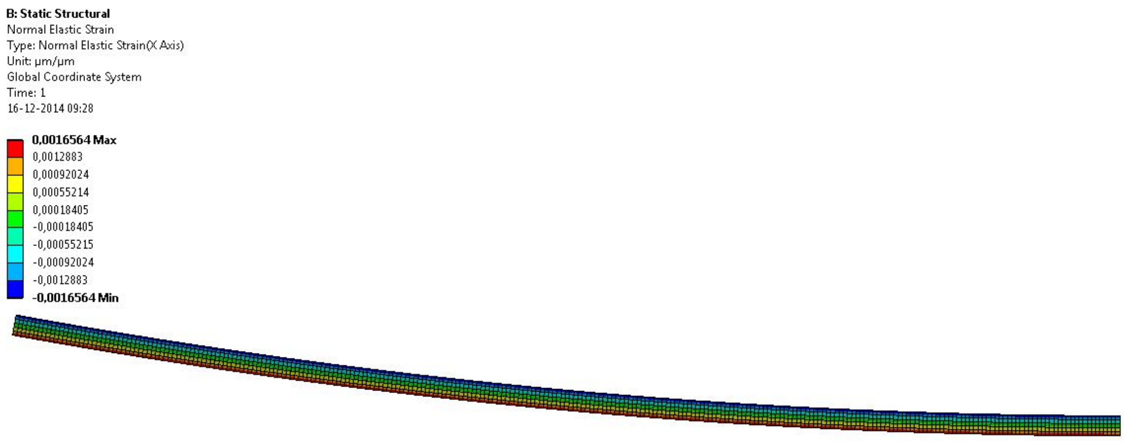


Figure 6.9: Normal strains in the x - direction [$\epsilon_{xx}$]

The strains shown in figure 6.9 should not be exceeded during the tests.

## 6.5 DIC of test device

Digital image correlation has attained increased popularity over the recent years with advancement in computer technology and quality of digital imaging systems (Sutton et al., 2009). The technology uses a stochastic speckle pattern that is applied to the test specimen. Then by recording pictures of the initial undeformed and later deformed specimen. The displacements are mapped through software. From this, based on the undeformed speckle pattern and deformed pattern, strains can be mapped.

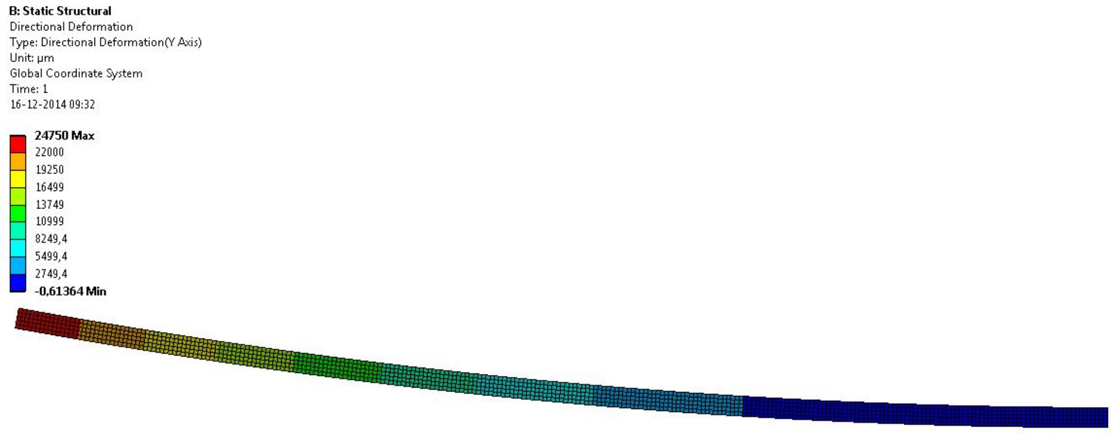


Figure 6.10: Displacements in the y direction

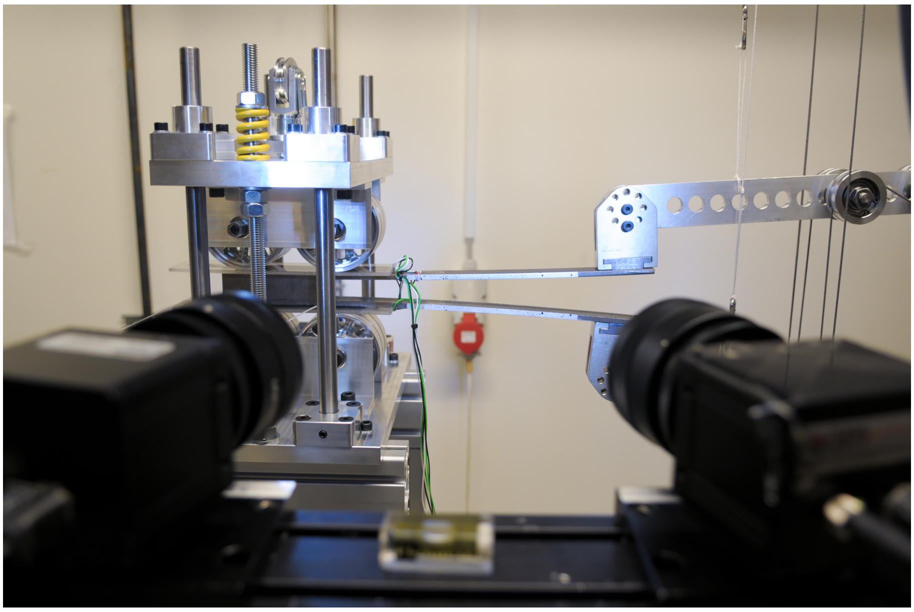

Figure 6.11: Test specimen with speckle pattern applied, subjected to mode I loading

In the current work, the technology is applied to the test device. Since large displacements are occurring as the test specimen moves horizontally in the fixture, it is needed to capture displacements with a relatively high frame rate, which was chosen to be 0.5 Hz.
The goal was to capture shear strains if present and validate them against the analytical results and strain gauge results. Both 2D and 3D DIC analysis was performed. 2D analysis turned out difficult since out of plane motions were observed. This lead to non-usable plots. For the 3D analysis, calibration of the scanner is essential, to obtain proper results.

### 6.5.1 DIC of test specimen - Mode I

One of the last plots for mode I, in the 3D series with the highest load, is seen in figure 6.12a. Here the plot as well as the graph for the section shows almost zero shear strains, which indicate that no shear strains are introduced into the test specimen.

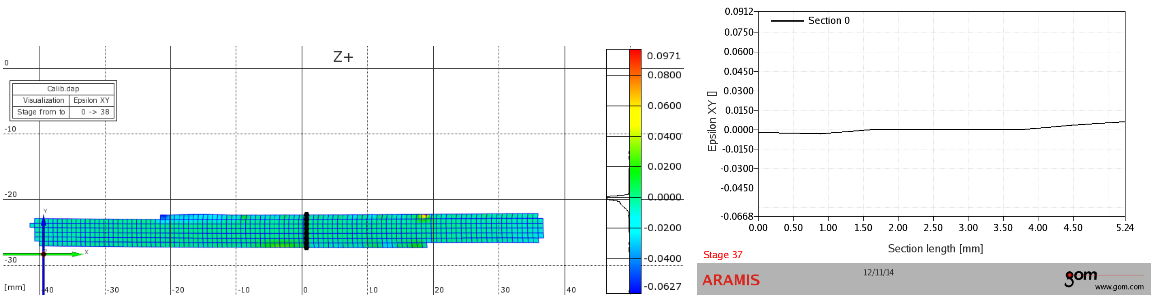


(a) (b)

Figure 6.12: DIC plot of part of the test specimen arm showing shear strains $\epsilon_{xy}$ under mode I loading

The normal strains from the DIC (figure 6.13) were compared to the measured normal strains, which was seen in figure 6.7. The normal strains seen in figure 6.13b, must be shifted down by 0.02%. Looking at the legend the distribution can be seen, where the majority of strain vary from -0.02 to +0.06. The measured strain gauge result at that loading point was, 0.04. It is therefore assumed that the results match.

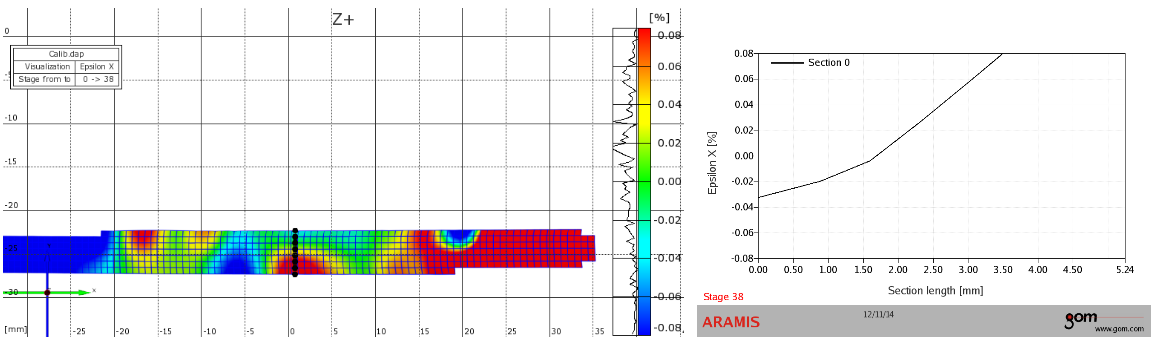


(a) (b)

Figure 6.13: DIC plot for the normal strains $\epsilon_x$ under mode I loading for the last stage

### 6.5.2 DIC of test specimen - Mode II

For mode II, the test was performed 3 times. The DIC equipment had a constraint of approximately 150 images due to RAM storage. Therefore the capture rate was set to 0.5 Hz. This meant that displacement jumps could not be captured correctly, and the software therefore not being able to compute solutions after a certain stage. The displacement jump is seen in figure 6.14.

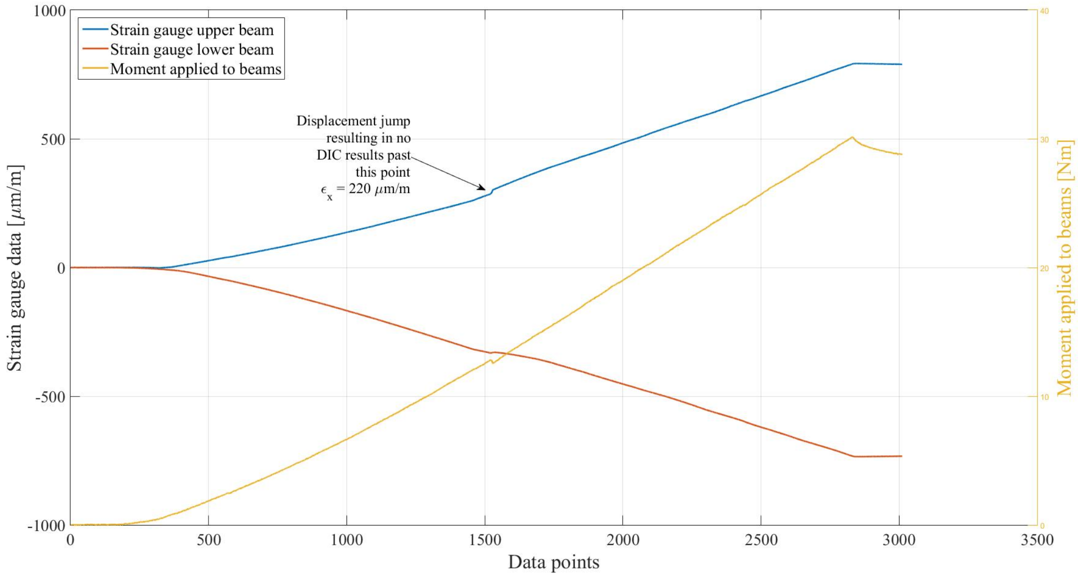


Figure 6.14: Strain gauge and load cell results for the test specimen subjected to mode II loading

Nonetheless, the results up to the indicated point in figure 6.14, showed good correlation with the DIC plots seen in figure 6.15. Here the black curve in figure 6.15b, shows that the strains can vary a lot in a plot. The yellow curve shows approximately the same strains as measured with strain gauges (seen in figure 6.14). Looking at the legend, it can be observed that the strains range from approximately -0.3 to +0.3. The strain gauge result, as indicated in figure 6.14, shows approximately the same result.

It is not a trivial task to interpret the results from DIC as it is depending on a lot of parameters. These are for instance; light, temperature variations, specimen preparation (speckle pattern), number of facets and density (resulting in noise), rigid body movement as well as the users experience. Nonetheless, it is assumed that the results are fairly correct.

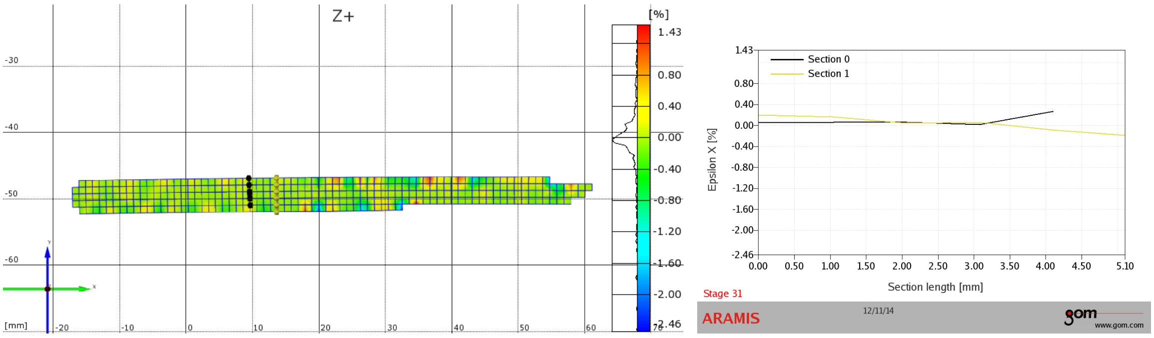


(a) (b)

Figure 6.15: DIC plot for the normal strains $\epsilon_x$ under mode II loading for the last stage

## 6.6 Conclusion

The goal of this chapter is to show that the test tool can be used to test DCB specimens under modes from pure mode I to pure mode II as well as mode mixities in-between. First the test specimen is verified analytically, where the outcome is analytical formulas used for predicting the influence of wire rotation as well as rotation of the moment arms.

A comparison between the analytical calculated force, based on strains, and the actual measured load from the load cell, during a mode I test, is given. This comparison shows a small deviation, which proves the validation of the analytic approach.

Further a finite element analysis has been performed on one of the moment arms in order to determine the maximum allowable strain, which converted to $\mu m/m = 1600$.

Digital Image Correlation (DIC) has been applied to the test specimen under both mode I as well as mode II. This was done in order to verify the strains measured using strain gauges. The correct use of DIC depend on a lot of factors, but it is assumed that the results where fairly correct. The DIC equipment had a constraint on the number of stages/ pictures that could be taken, therefore displacement jumps could not be captured properly during mode II loading.

# Chapter 7

# Sources of error and future improvement

## 7.1 Introduction

For the current setup, some of the errors that must be taken into account during tests is discussed below. This is followed by suggestions to future improvements to the test fixture.

## 7.2 Rope

Two different types of rope were used. Both the chosen downhaul line (DH) as well as Ocean 3000 line in a 2 mm. thickness version (O3) were tested. The DH line when initially loaded showed large elastic displacements. This was assumed to be due to lack of pretension from the supplier. The pretension was then later performed manually by stretching the entire rope with a force of approximately 1 kN. The result was very low elasticity.
The other rope used in the tests (O3), was already pre-stretched from the supplier and showed very little elasticity. One of the requirements for the rope, was that the friction between rollers and rope should be small. This however was seen for both types of rope not to be the case. As the rope force increased, the friction increased as well. This was measure to be approximately $10 \pm 5\%$ of the load applied. This was not acceptable.

The friction between rollers and rope can cause a difference in rope force between right and left side of the test tool. This in turn can lead to twisting of the moment arms and thereby introduction of torsion to the specimen. This is highly unwanted.

Figure 7.1: Ocean 3000 wire running around the moment arm rollers

A solution to this is either to apply wax to the entire rope or lubricate it using an silicone based lubricant as polyethylene is compatible with silicone. The later has been used in the tests.

## 7.3 Rollers

The rollers that lead the rope through the system are fitted with standard sealed SKF bearings. These bearings should result in a small amount of friction in the system due to the grease between the rollers and racetrack in the bearing. Even tough the Ø25 mm center-less shafts, that were used, where delivered with a H9 tolerance, the measured diameter was Ø25.05 mm. This resulted in higher friction than expected because the inner ring pushed against the rollers. All the shafts were subsequently grinded down below Ø25 mm. This alleviated the problem. In order to further reduce the friction in the rollers, the grease can be washed out using a high temperature degreaser- machine followed by re-lubrication with low viscosity oil.

Another problem with the rollers observed, was as indicated above for the rope, that the friction between roller and rope could result in different rope forces between the left and right side of the test tool. This could be alleviated by cutting the wire rollers in two and fitting extra bearings. This however again, requires very low friction bearings as the number of bearings in the system double. A simple solution could be to lubricate the rope, as indicated above.

## 7.4 Counter balance system

The counter balance system is designed using two weights that are fabricated so that the weight is the same as the moment arms. They are suspended from the top of the test rig in thin ropes through a winch block and connected to the moment arms in their center of gravity. This solution is based on a low cost criteria. The optimum solution would be to use a balancer system, that is provided by for instance `fodgaard.dk`. This system consists of a pre- tensioned constant force spring, attached to a wire. It reacts very fast and is considered to be the best option for both static as well as fatigue analysis.

## 7.5 Constant force in the rope

One of the issues observed in the initial tests, using the strain gauges attached to the test device. Was that due to the friction in the rollers, the rope force was not constant for the entire length. This was measured in the top and bottom beam of the test device using strain gauges. In order to verify the measurements, another load cell (HBM U9B - 2 kN) was inserted in the lower part of the test machine in a special fixture that was fabricated. Using this, both the load on the cross head and the bottom machine interface could be measured simultaneously. This interface is seen in figure 7.2.

Figure 7.2: Lower interface for the test machine with load cell

The difference between the upper cross head load cell and the lower fabricated device, with the build in load cell, showed a difference of $10 \pm 5\%$ of the applied load between the upper and lower cross head.

A solution to overcome this was made by attaching the test fixture frame directly to the lower cross head and applying the load from the upper cross head only. This is indicated in figure 7.3a and 7.3b.

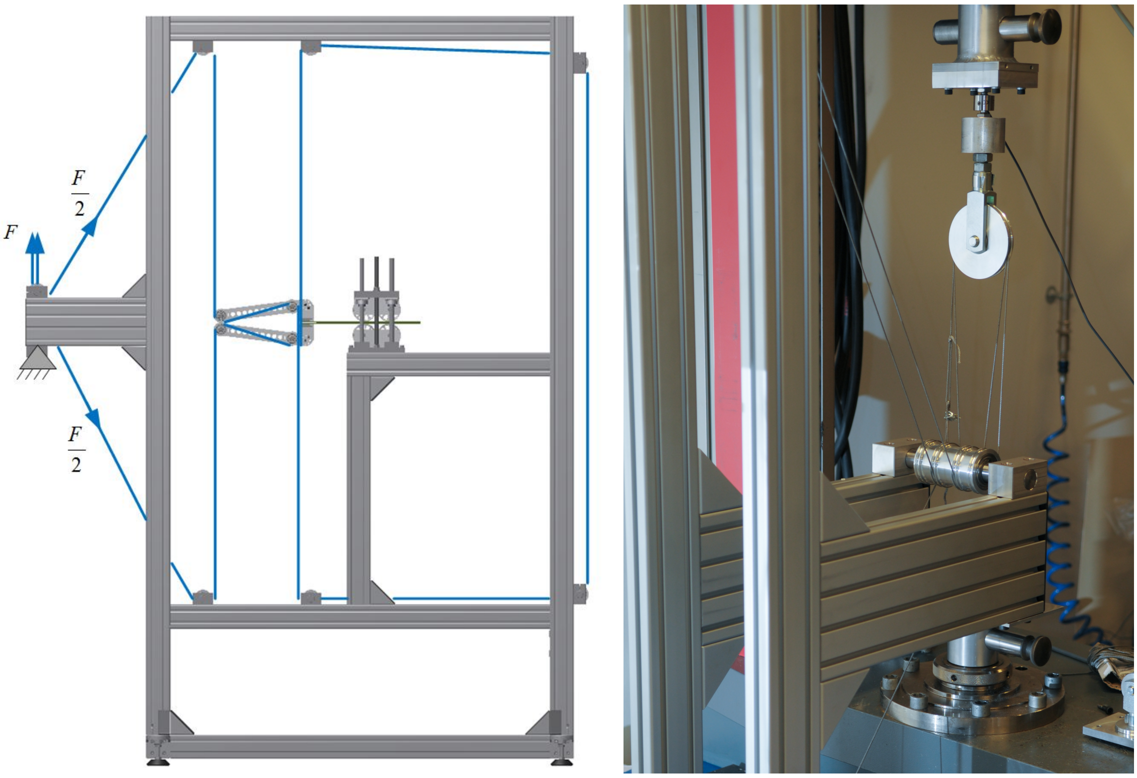


(a) (b)

Figure 7.3: New test method where the wires are assembled and loaded by the upper pulley

One of the key benefits found from this method, was that the frictional forces in the rollers were now even for the two moment arms. I.e. there was symmetry in the loading system. Further the cross head travel was reduced to half compared to the previous setup.

## 7.6 Specimen fabrication

For mode II tests, no clear test results were obtained due to large rotations and displacements. This was mostly due to thin specimens. In figure 7.4, it can be seen that the maximum load that was introduced was approximately 160 N, before a displacement jump occurred. After this the specimen rotation was so large that the roller fixture could not constrain it. The rotation for mixed mode loading is seen in figure 7.5. Here the test was stopped due to wires touching the shaft part of the opposite moment arm as seen in the picture.

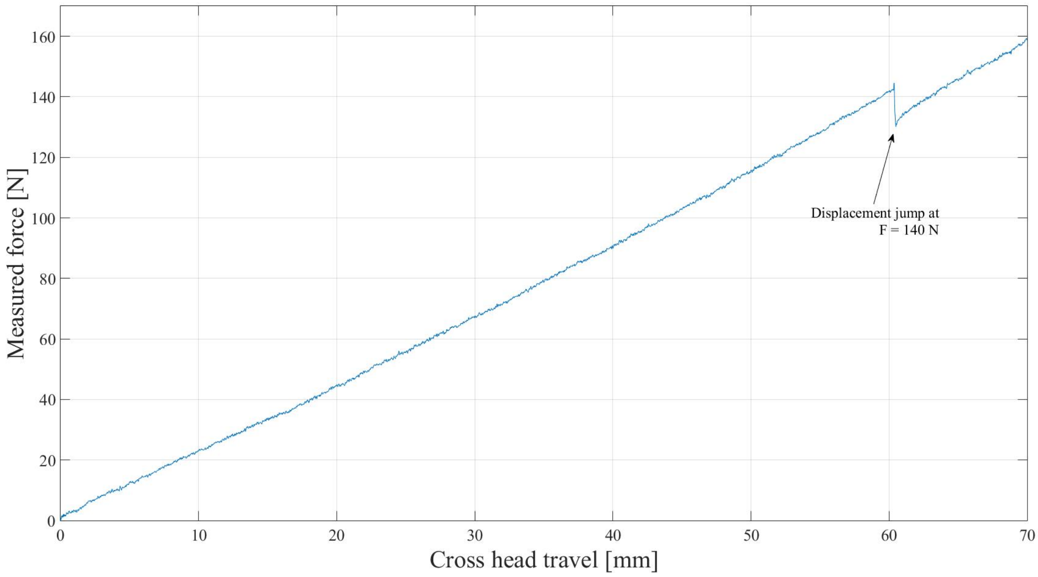


Figure 7.4: Cross head travel and measured force for mode II test no. 3

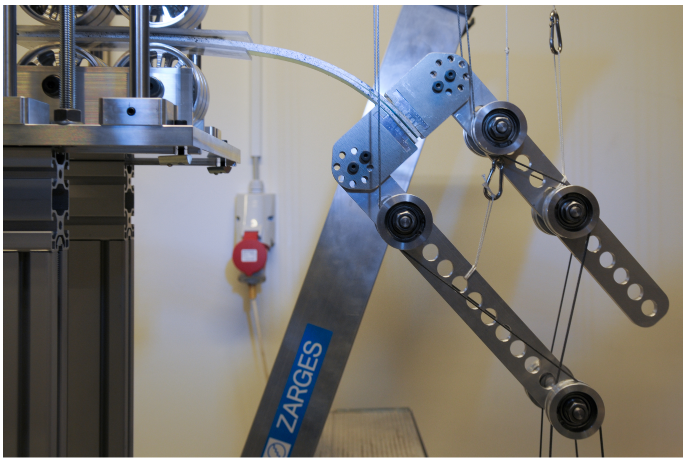


Figure 7.5: End rotation of mixed mode test with $\beta = 0.5$

This means that for mode II testing and for mode mixity testing with $\beta \geqslant 0.5$, the specimen thickness should be considered. Furthermore the presetting of the moment arms opposite to the rotation direction should be considered as well.

## 7.7 Brackets

Mounting the brackets for the moment arm attachment was an issue during tests since many of them broke off. They were initially mounted using screws. But since the screws could only attach with the tip, as the thickness of the specimen arms where only 3.4 mm, they could not get enough grip. Then gluing the brackets with an epoxy based quick adhesive from the supplier Biltema A/S, was tried. This did also not produce good results. Lastly a combination of glue and adhesive produced reasonable results. For future work, HF Marine A/S has been contacted, who advised to use either G/Flex epoxy system adhesive or a thickened SIX10 epoxy by West Systems. For specimens thicker than $H = 5$ mm. Normal screws can be used as they can get a better grip in the laminate.

# Part III

# Test results, finite element analysis and comparison

# Chapter 8

# Test specification

## 8.1 Introduction

In order to obtain the cohesive zone properties of the DCB specimens two different approaches can be followed, which are outlined in figure 8.1.

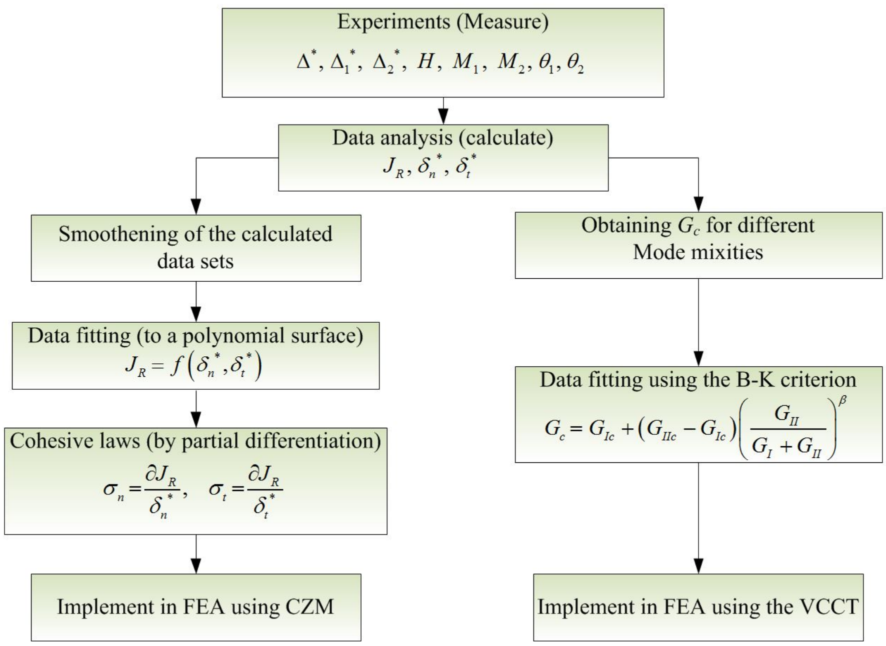


Figure 8.1: Procedure in evaluating the cohesive stresses

The first method presented on the left side of the figure is suggested by (Sørensen, 2010). Here a certain number of issues must be addressed. First there are a number of variables that must be measured. Data analysis must be performed, smoothing of the data sets must be made. Data fitting in order to obtain polynomials and last but not least the cohesive laws are created. The other method shown to the right, proposed here, takes a slightly different approach. First the same number of variables must be measured, then data analysis is performed, followed by obtaining $J_{ss} \cong \mathscr{G}_c$ for different mode mixities. These data are then plotted in a $\beta - \mathscr{G}_c$ diagram and fitted using the B-K criterion. The difference between the two methods is that the method where the outcome is the cohesive tractions, they can be implemented in finite element analysis using the cohesive zone method (CZM). The proposed method, which builds on the work of (Camanho and Davila, 2002) and (Benzeggagh and Kenane, 1996), uses pure moments to find the critical ERR for different mode mixities. These are then implemented in finite element analysis using the VCCT.

## 8.2 Test specimens

The test specimens are made using 1210 $g/m^2$ unidirectional E-glass fiber mats with 5 % transverse strength and Poxy systems GL2 epoxy resin. The specific data for the mats and epoxy are shown in table 8.1.

| - | Fiber | Epoxy |
|---|---|---|
| Weight $[g/m^2]$ | 1210 | - |
| Density $[kg/m^3]$ | - | 1171 |
| Modulus of elasticity $E_{11}$ [MPa] | 73000 | 3490 |

Table 8.1: Mat and epoxy material data

A plate consisting of 8 layers of UD fibers, with a 20$\mu$m film placed between the middle layer along one edge as a crack starter, was manufactured using the Vacuum Assisted Resin Transfer Molding (VARTM) technique. A picture can be seen in figure 8.2. The plate was then cured at room temperature for 24 hours and post cured 16 hours at 80°C according to manufacturers specification. The plate was then cut into strips of approximately 25 mm width using a stationary table saw with a diamond cutting blade. Followed by a grinding process to obtain equal widths of $24 \pm 0.2$mm.
The overall macro scale laminate properties, that were calculated, is seen in table 8.2.

## 8.3 Measuring mode I opening

In order to obtain the cohesive law for mode I opening, the opening of the crack tip ($\delta^*$) must be measured together with the moment applied to the specimen. Measuring the moment is quite easy, as the force is output directly from the test

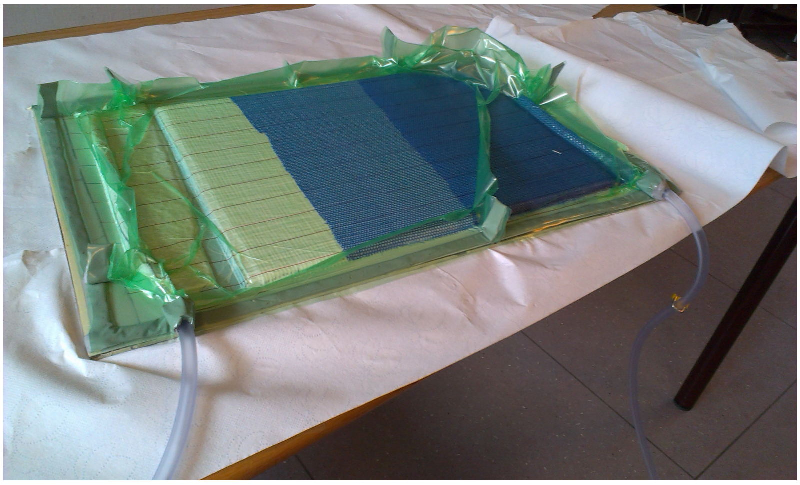

Figure 8.2: Specimen manufacturing using the VARTM process

| - | - | E - glass / epoxy |
|---|---|---|
| Density $[kg/m^3]$ | $\rho$ | 1972 |
| Longitudinal modulus $[GPa]$ | $E_{11}$ | 41.18 |
| Transverse modulus $[GPa]$ | $E_{22}$ | 6.4 |
| In-plane Poisson's ratio | $\nu_{12}$ | 0.19 |
| Transverse Poisson's ratio | $\nu_{23}$ | 0.27 |
| Fiber volume fraction | $V_f$ | 0.55 |
| Ply thickness [mm] | $t_k$ | 0.95 |

Table 8.2: Macroscale laminate properties

machine and must be multiplied by the distance between the rollers $L$ as was seen in figure 6.6. For mode I opening, only the opening of the specimen is measured. This is measured using a self made clip gauge, using strain gauges set up in a Wheatstone bridge. See figure 8.3a. The relation between the strains measured in the clip gauge and the end opening is taken from ordinary beam theory. When a cantilevered beam opens due to a force $F$, the displacement is:

$$v = \frac{F \cdot L^3}{3EI} \tag{8.1}$$

The strain at the fixed end can be calculated from $\sigma_{xx} = -\frac{M \cdot h}{2I}$, were $h$ is the thickness, and using Hooke's law:

$$\epsilon_{xx} = \frac{F \cdot L \cdot h}{2EI} \quad \Longrightarrow \quad F = \frac{2\epsilon_{xx} EI}{Lh} \tag{8.2}$$

The end opening can then be calculated by inserting 8.2 into 8.1 and simplifying:

$$v = \frac{2\epsilon_{xx} L^2}{3h} \tag{8.3}$$

Introducing the thickness for the clip gauge arms (h = 0.4 mm), the length from where the pins are connected to the center of the strain gauges (45 mm), and realizing that the entire opening $\Delta^*$ is the double of $v$. Furthermore with a bridge factor for the current Wheatstone bridge $\kappa = 4$, then equation 8.3 reduces to:

$$\Delta^* = 2 \cdot v = 27000 \cdot \epsilon^*_{xx} \tag{8.4}$$

Were $\epsilon^*_{xx}$ is the measured strain from one strain gauge in $\left[\frac{mm}{mm}\right]$. However calibrating the clip gauge, using a caliber, resulted in a correction value applied to eq. 8.4, so that the number multiplied with the SG 120  full bridge output $\epsilon \left[\frac{\mu m}{m}\right]$ was 0.032 instead of 27.000.

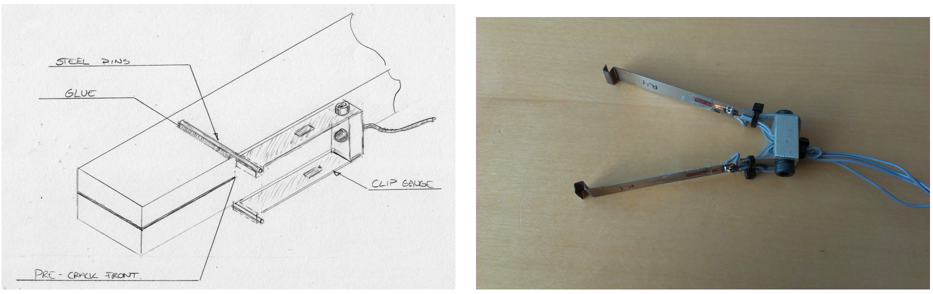


(a) Sketch of the measuring principle (b) Photo of the fabricated clip gauge

Figure 8.3: The clipgauge

A problem arises when the specimen deforms. Then the measured distance $\Delta^*$ is not equal to $\delta^* + 2H$, which is due to the rotation of the specimen arms. This is illustrated in figure 8.4.

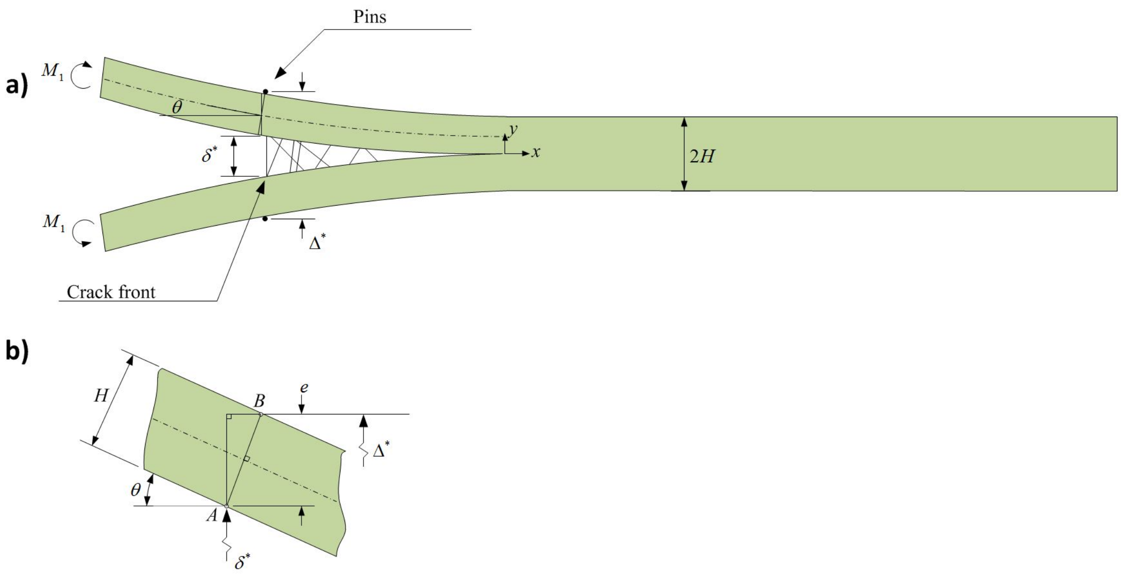


Figure 8.4: Opening of specimen under mode I loading

A small correction must be made according to figure 8.4 b), which can be expressed as:

$$\delta^* = \Delta^* - 2 \cdot e \tag{8.5}$$

Were $\theta$ is the rotation of one DCB arm. And $e$ in figure 8.4 b), is expressed as:

$$e = H \cdot cos(\theta) \tag{8.6}$$

This however is neglected due to impracticalities measuring the angle real time. In the tests the clip gauge was simply zeroed at the beginning of the test. Another issue considered is the rotation of lines initial perpendicular to the normal. I.e. point $B$ in figure 8.4 is translating further in the $+x$ - direction. This could have been avoided, by placing the pins in the neutral axis of the beams, but this is unfortunately not possible with thin specimens. But here it is also considered negligible as the rotation due to elasticity can be determined using ordinary beam theory and will give a small contribution for thin specimens. The relation between curvature of the beam neutral axis and strain is $\epsilon_{xx} = y/\rho$, where $\rho$ is the curvature.

### 8.3.1 Test procedure for mode I

The following procedure must be followed for mode I tests:

1. Install pins at the crack tip. For specimens with a thickness $H \leqslant 5$mm the pins are mounted using glue on the surface. For thickness $H > 5$mm, the pins are inserted with glue into drilled holes at neutral axis in the beam ends, perpendicular to the crack tip.

2. Install brackets on specimen using glue or screws. For smaller specimens with $H \leqslant 4$mm use a thickened epoxy like SIX10 by West Systems.

3. Mount the plastic plates on the test specimen using thin double adhesive tape in order to reduce the friction between rollers and specimen

4. Install moment arms on the test specimen

5. Install the specimen in the roller fixture and in the wire setup

6. Adjust the wires, so that they are all vertical

7. Mount the clip gauge to the pins

8. Measure the strain in $[\mu m/m]$ from the clip gauge and the force $[N]$ from the test machine simultaneously

9. Convert the measured force into moment $[Nmm]$ using eq. 6.8, or if the angles are neglected, simply use $M = F \cdot L$, where $L = a + 2 \cdot R$ and $a$ and $R$ are the distance between rollers and radius of rollers respectively (see figure 6.6)

## 8.4 Measuring mixed mode / mode II opening

For mixed mode and mode II opening the following variables must be measured: $\Delta_y$, $\Delta_x$, $\theta_1$ and $\theta_2$ (see figure 8.5). Then the variables $\delta_n$ and $\delta_t$ are derived as follows:

$$\theta_3 = \tfrac{1}{2}(\theta_1 + \theta_2) \tag{8.7a}$$
$$BD_x = \tfrac{H}{2} sin(\theta_2) \tag{8.7b}$$
$$BD_y = \tfrac{H}{2} cos(\theta_2) \tag{8.7c}$$
$$AC_x = \tfrac{H}{2} sin(\theta_1) \tag{8.7d}$$
$$AC_y = \tfrac{H}{2} cos(\theta_1) \tag{8.7e}$$
$$\delta_x = \Delta_x - (AC_x + BD_x) \tag{8.7f}$$
$$\delta_y = \Delta_y - (AC_y + BD_y) \tag{8.7g}$$
$$\delta_c = \sqrt{\delta_x^2 + \delta_y^2} \tag{8.7h}$$
$$\theta_4 = acos\left(\frac{\delta_x}{\delta_c}\right) \tag{8.7i}$$
$$\theta_5 = \theta_3 + \theta_4 \tag{8.7j}$$
$$\theta_6 = \tfrac{\pi}{2} - \theta_5 \tag{8.7k}$$
$$\delta_t = \delta_c \cdot sin(\theta_6) \tag{8.7l}$$
$$\delta_n = \delta_c \cdot cos(\theta_6) \tag{8.7m}$$

The global relative displacements and angles can all be measured using DIC. The previous methods used by (Sørensen and Jacobsen, 2009), where two linear variable displacement transducers (LVDT) is used, is fairly complicated to set up. Furthermore the measurements are sensitive to small errors as for instance a rough surface on the special bracket that is mounted, could prevent the LVDT's to change position.

Then the energy release rate $J_R$ can be calculated based on the end opening (sliding

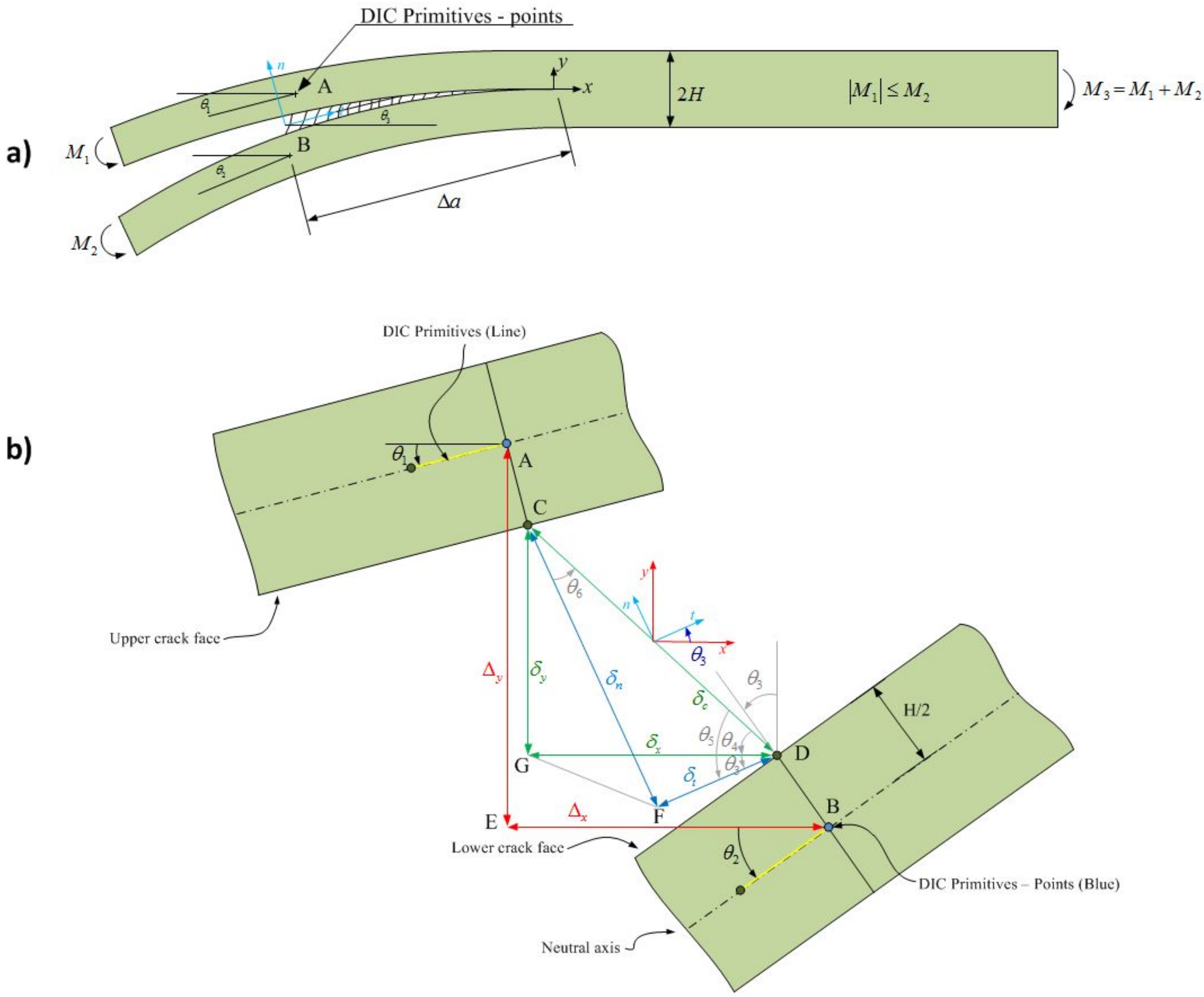


Figure 8.5: Opening of specimen under mixed mode loading

for mode II and mixed mode) and the external applied moment by applying eq. 4.23 and 4.24 as indicated in section 4.2.

### 8.4.1 Test procedure for mode mixity and mode II

The test procedure for mode mixity and mode II is similar to the test approach for mode I. Here a suggestion is made to use DIC to measure displacements and rotations of the specimen arms as was discussed in section 8.4. This is performed in order to calculate the normal opening ($\delta_n$) and tangential sliding ($\delta_t$) of the crack tip.

1. Prepare the specimens with a speckle pattern suitable for DIC
2. Install brackets on specimen using glue or screws as described for mode I testing

3. Mount the plastic plates on the test specimen using double adhesive tape in order to reduce the friction between rollers and specimen
4. Install moment arms on the test specimen
5. Install the specimen in the roller fixture and in the wire setup approapriate for the mode mixity or mode II setup
6. Adjust the wires, so that they are all vertical
7. Using DIC, measure the displacement of points on the neutral axis of the two beams, perpendicular to the crack tip, simultaneously with the force from the test machine
8. Convert the measured force into moment $[Nmm]$ using eq. 6.3, or if the angles are neglected, simply use $M_1 = F \cdot L_1$ or $M_2 = F \cdot L_2$ where $L_{1,2} = a_{1,2} + 2 \cdot R$. Here $a_{1,2}$ is the distance between the rollers for moment arm 1 and 2 respectively. $R$ is the radius of the rollers (see figure 6.6)

## 8.5 Conclusion

This chapter outlines a test specification for testing mode I, mode II or mode mixity for DCB specimens. First a new procedure was proposed where instead of fitting the $J_R$ data to a polynomial surface, the data is fitted to the B-K criterion. Then the test specimens and the manufacturing process were described. For mode I tests a description of how to attach and measure the opening using the fabricated clip gauge is given. Then for mixed mode and mode II a derivation is given how to obtain the normal - and tangential sliding of the crack tip when tracking four points on the specimen. Test procedures are given for both mode I and mixed mode including mode II.

# Chapter 9

# Test results

## 9.1 Introduction

Here the test results for mode I, mode II, and mode mixity are shown. The following tests were performed:

- 6 test with full mode I, where 4 tests were completed
- 3 tests in a full mode II setup, where no tests were completed
- 2 tests with a mode mixity ratio of $\beta = 0.5$, where both were partly completed

All tests were performed using a Zwick 100 kN electro mechanical testing machine.

## 9.2 Mode I setup

Mode I testing was the easiest of the tests that were performed. This was due to easy installation of the clip gauge, thereby being able to measure the opening of the initial crack tip. Furthermore the load from the test machine was recorded using the previously described HBM U9B load cell. This made it possible to record both the opening and the load introduced on the same data acquisition tool, which was a HBM Spider8.

The moment arms, attached to the specimen brackets, where initially preset to $-10°$. This resulted in a final $+10°$ opening for continuous crack propagation. Hence no need for correcting the moment using $\theta$, as indicated by eq. 6.8, was needed. The setup before loading is seen in figure 9.1

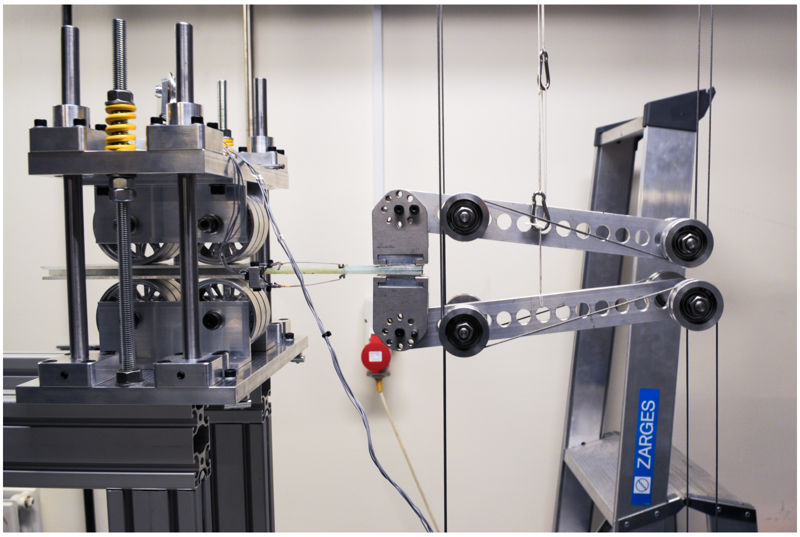


Figure 9.1: Setup for mode I testing. Moment arms preset $-10°$ compared to rotation direction

The test results for the moment measured vs. the crack tip opening is seen in figure 9.2. Here it is seen that tests 3 and 4 almost achieved stable crack propagation before the tests were aborted due to brackets breaking off.

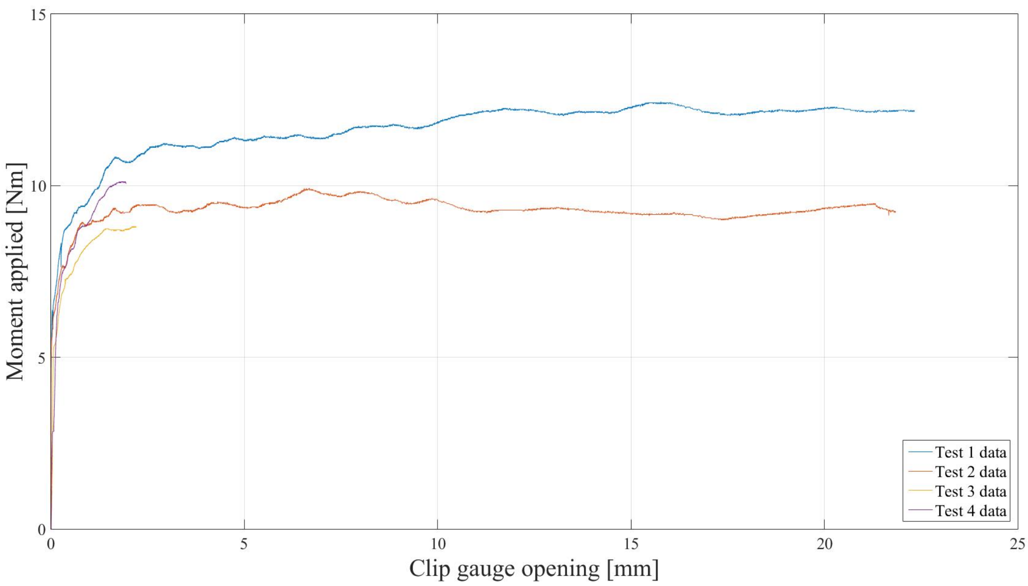


Figure 9.2: Measured moments for mode I tests and clip gauge displacement

In figure 9.3, the $J_{ext}$ is plotted for the four tests. A power curve is fitted to each of the tests as well as a median of all four. Furthermore, the computed $J_{ext}$ from a finite element test using $\mathscr{G}_{Ic} = 1500\frac{J}{m^2}$ is plotted. This was equivalent to $J_{ss}$. The finite element analysis is described in the next chapter. For the median line, the following power law has been fitted with $n = -0.92$ (Sørensen, 2010):

$$J_R = J_0 + \Delta J_{ss} \left( \frac{\delta_n^*}{\delta_n^c} \right)^{n+1}, \quad \text{for} \;\; 0 < \delta_{\mathrm{n}}^* < \delta_{\mathrm{n}}^{\mathrm{c}} \tag{9.1}$$

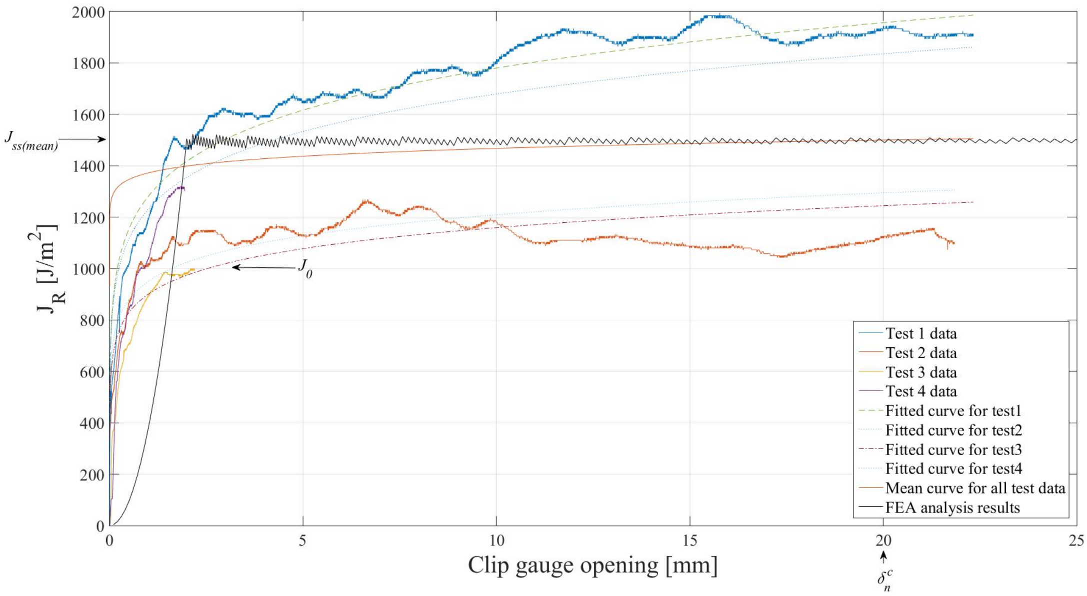


Figure 9.3: Measured moments for mode I tests and clip gauge displacement

This equation is essentially the same as presented earlier in eq. 4.25. In order to obtain the cohesive tractions, the median curve fit for the $J$- integral, shown in 9.3 is differentiated, with respect to the opening using eq. 4.23. This is shown in eq. 9.2 (Sørensen, 2010):

$$\sigma_n(\delta_n^*) = (n+1) \cdot \frac{\Delta J_{ss}}{\delta_n^c} \cdot \left( \frac{\delta_n^*}{\delta_n^c} \right)^n \tag{9.2}$$

The differentiated function, shown in eq. 9.2, is plotted in figure 9.4. Here it is seen that a singularity exists as $\delta_n^* = 0; \sigma_n \to \infty$. This is assumed not to be physically acceptable. Sørensen (2010), suggests to use micro mechanics as described in appendix D in order to obtain the crack initiation stress $\sigma_n^0$. This is however outside the scope of this work. This further shows that it is difficult obtaining the initiation stress, which is used with the cohesive zone method in FEA.

## 9.3 Mode II setup

Mode II was first verified using the test specimen (seen in figure 9.5) as was previously discussed in section 6.5.2. A plot of the measured strains together with the

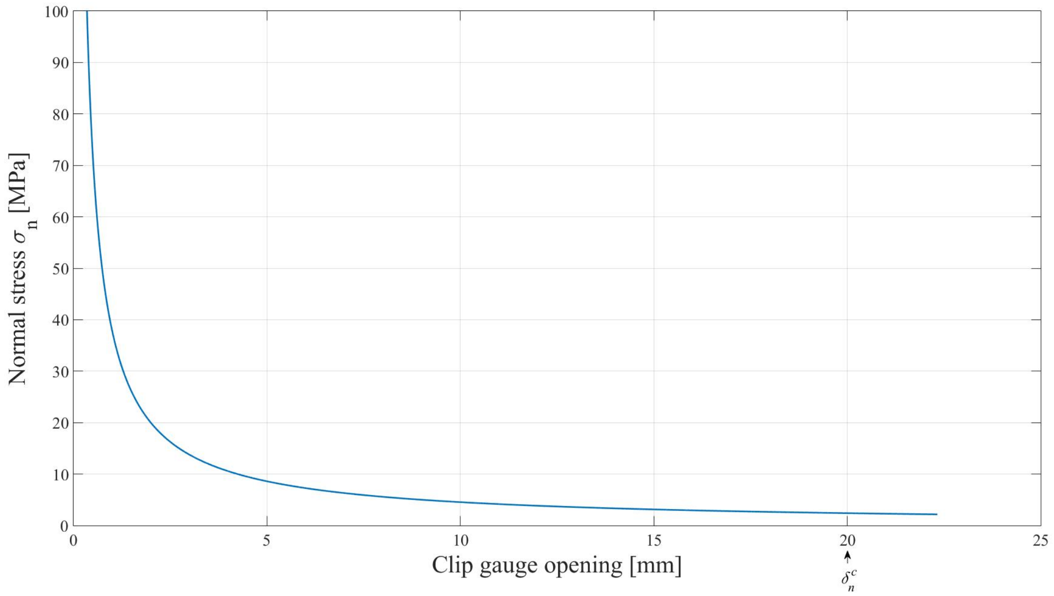


Figure 9.4: Normal stress as a function of opening $\sigma_n(\delta_n^*)$

moment applied to the beam ends was shown in figure 6.14.

As mentioned previously no crack propagation was recorded in any of the 3 tests performed. The output from the test machine, can be seen in figure 9.6.

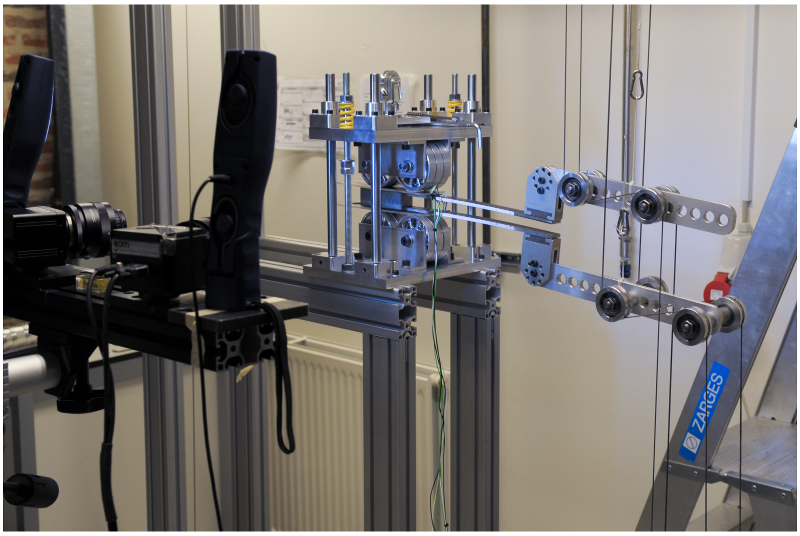


Figure 9.5: Setup for validating Mode II loading with DIC and strain gauges

Here it is assumed that the stiffness and hence the thickness of the specimens plays a large role. If the stiffness is not high enough, too large rotations will occur. This implies that the moment reduces as the specimen rotates as indicated by eq. 6.8. Another effect observed, was the the laminate was "bend" where the brackets

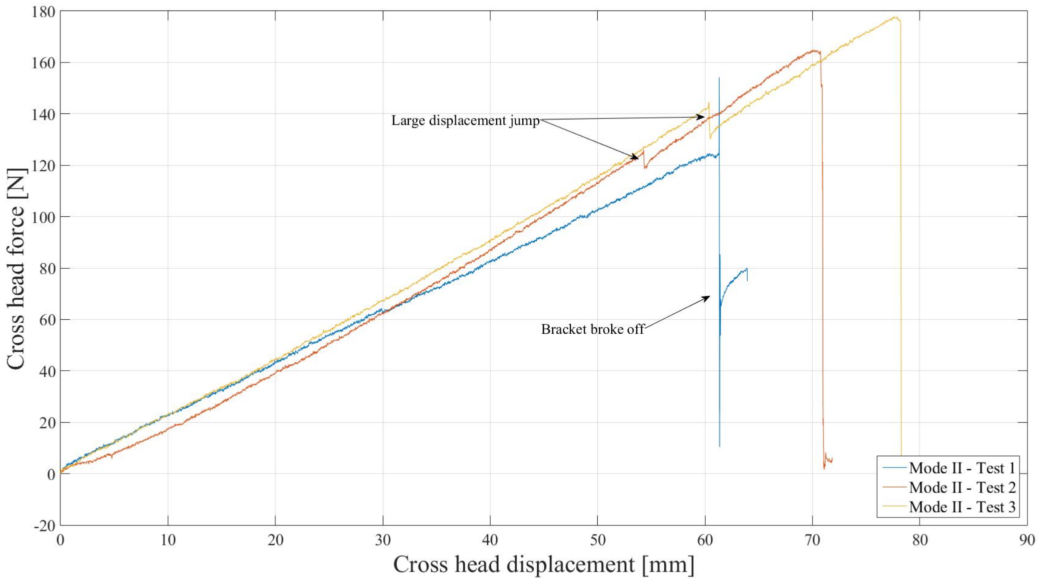


Figure 9.6: Mode II test results, showing cross head displacement and measured force

were mounted. This is seen in figure 9.7. This bending is assumed to increase the resistance for crack initiation.

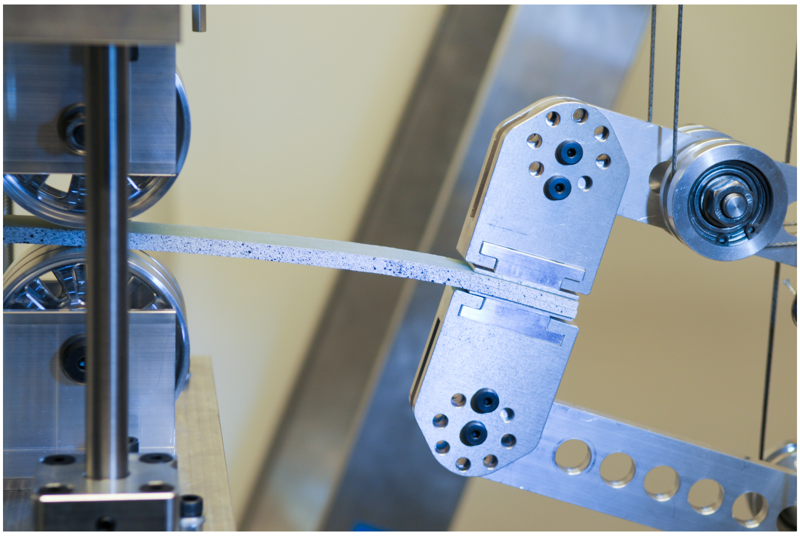

Figure 9.7: Bending of the laminate due to low stiffness at the bracket interface

The displacements and rotations were tracked using DIC up to the first displacement jump. Then the software failed to track the speckle pattern. However using stage data, it is possible to write a program that can track displacements by reading the data for individual facets. For example for Mode II - test 1, the following data (table 9.1) can be read from stage 5 and 87 for the facets with index (32,78) and

(92,79), which is located approximately at the crack tip. This is approximately at points A and B, seen in figure 8.5. Furthermore two additional points must be defined in order to obtain rotations $\theta_1$ and $\theta_2$. This was not obtainable due to the speckle pattern being of too low quality. Additionally filtering and smoothing must be applied, as the data contains noise. I.e. displacements might be wrong or differ a lot between stages. Creating the program, was outside the scope of this work, but it is recommended to study this further. Another issue is that the DIC software must be triggered by the test machine, in order to have a consistent time frame.

| St. | Index x | Index y | Undef. x | Undef. y | Def. x | Def. y | Displ. x | Displ. y |
|---|---|---|---|---|---|---|---|---|
| 5 | 32 | 78 | -42.05 | -27.75 | -42.30 | -27.66 | -0.247 | 0.085 |
| 5 | 92 | 79 | 29.14 | -27.82 | 28.90 | -27.75 | -0.24 | 0.076 |
| 87 | 32 | 78 | -42.05 | -27.75 | -46.79 | -30.377 | -4.733 | -2.63 |
| 87 | 92 | 79 | 29.14 | -27.82 | 24.76 | -36.54 | -4.86 | -8.72 |

Table 9.1: Stage data for stage 5 and 87 during mode II test

## 9.4 Mixed mode tests

The mixed mode tests were performed, using a mode mixity ratio $\beta = 0.5$. Here the specimen brackets were glued and screwed. This resulted in no brackets braking off. The output from the test machine is seen in figure 9.8.

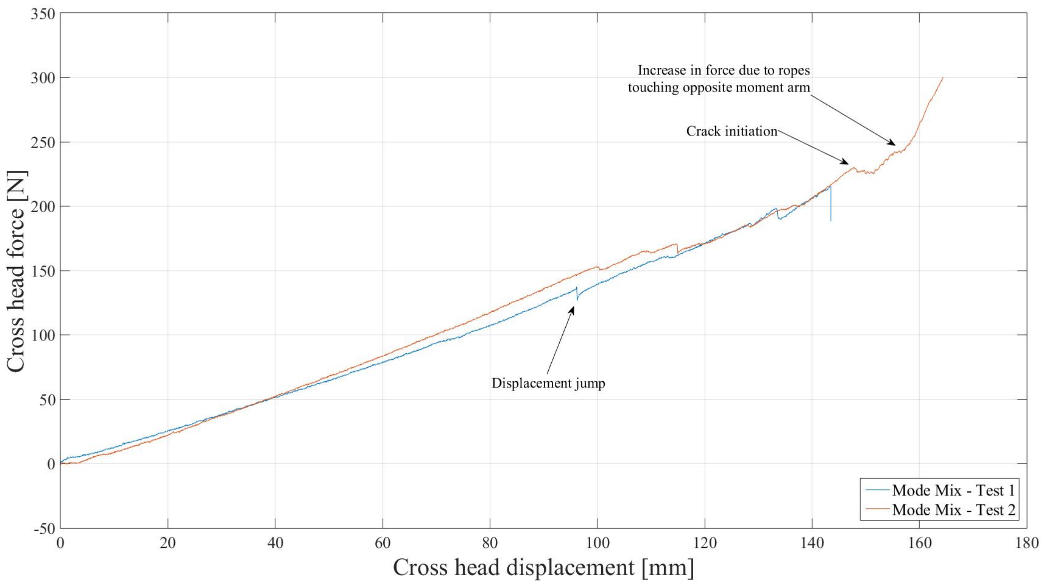


Figure 9.8: Mode mixity test results with $\beta = 0.5$, showing cross head displacement and measured force

Crack propagation was observed in the end of test 2. However the rotations were very large, which meant that no DIC capture of the specimens could be achieved at this point. The end rotations were more than 50°, which could be seen in figure 7.5.

## 9.5 Conclusion

Mode I, Mode II and mode mixity tests have been performed. For mode I testing - two highly successful tests were conducted. Two further tests didn't finish, but steady state crack propagation was indicated. The data was treated, to find a Mode I critical ERR of approximately $1500 J/m^2$. Mode II tests were inconclusive as no crack propagation was found. This is assumed to be due to low stiffness of the specimens and thereby large rotations. One of the two mode mixity tests were partly successful as crack propagation was observed. However due to very large rotations $\theta > 50°$, the tests were aborted. Data capture using DIC was investigated for mode II and mode mixity. However a number of issues were found. The frame rate should be set very high, in order to capture displacement jumps. This was not possible due to RAM limits in the computer. Further in order handle the data obtained, a program must be written, that sorts, filters, smoothens and treats the data. This is outside the scope of this work.

# Chapter 10

# Finite element analysis

## 10.1 Introduction

The use of the finite element method (FEM) in design of layered composites has attained increased attention over the recent years due to the increase in computer effectiveness and commercially available codes. This also applies for delaminations in layered composite materials. These delaminations can be analyzed, either using cohesive damage models or linear elastic fracture mechanics. The cohesive damage models, are modeled as either zero thickness or finite thickness elements, that are inserted between shell or solid elements. Using LEFM the growth of a crack can be predicted by using either the global energy approach were the SERR $\mathscr{G}$ is calculated or the local SIF approach with $K$. Both are energy methods and equivalent as shown in chapter 3. Here the VCCT also applies with the use of finite or zero thickness interface elements.

In the following a script is described, that has been made to accommodate 2D delamination analysis using the LEFM VCCT. The script has been used to plot the $J_R$ as function of the crack tip opening. This was then plotted against $J_R$ calculated from mode I tests. This was seen in figure 9.3.

## 10.2 2D VCCT script for delamination analysis

The results from the tests are used as input to a 2D plane stress finite element model. The commercial program Ansys APDL v.15.0 is used.

The chosen elements are linear 4 noded solid elements (Plane182) with enhanced strain formulation in order to reduce the effect of shear locking and incompatible modes in bending dominated problems as for the case of the DCB specimens. The interface is meshed with zero thickness 4 noded interface elements INTER202.

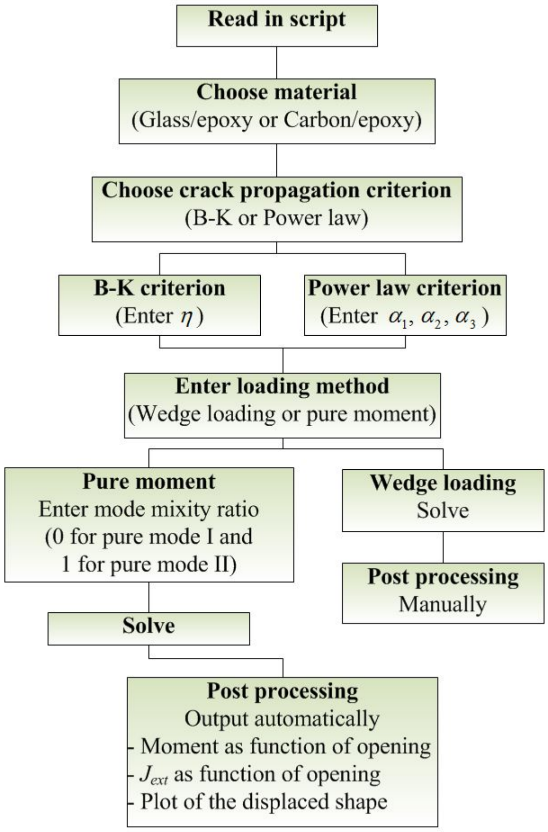


Figure 10.1: The process in using the script

Here the upper and lower nodes are initially coincident. The user can choose from glass/epoxy material data as used in the tests or data for a carbon/epoxy prepreg taken from (Ansys, 2014). The script is capable of performing wedge loading for pure mode I and apply pure moment to specimens ranging from pure mode I to pure mode II including mode mixities in-between. The script uses the VCCT and crack propagation is determined by either the classic power law or the B-K criteria. These are all explained in depth in appendix C. Here an introduction to the finite element method is given, where the governing equation is derived based on the principle of virtual work. Furthermore an introduction to delamination using FEM is given, the constitutive behavior for single mode and mode mixity is derived. Followed by a presentation of the constitutive tangent tensor. Finally nonlinear solution methods are briefly discussed and the LEFM approach using VCCT is introduced.

When running the script, which is enclosed on the accompanying DVD, the user is asked to enter if wedge loading or pure moment should be used, which of the two materials should be used, loading method (wedge or pure moment), which crack propagation criteria should be used, and the mode or mode mixity (only for pure

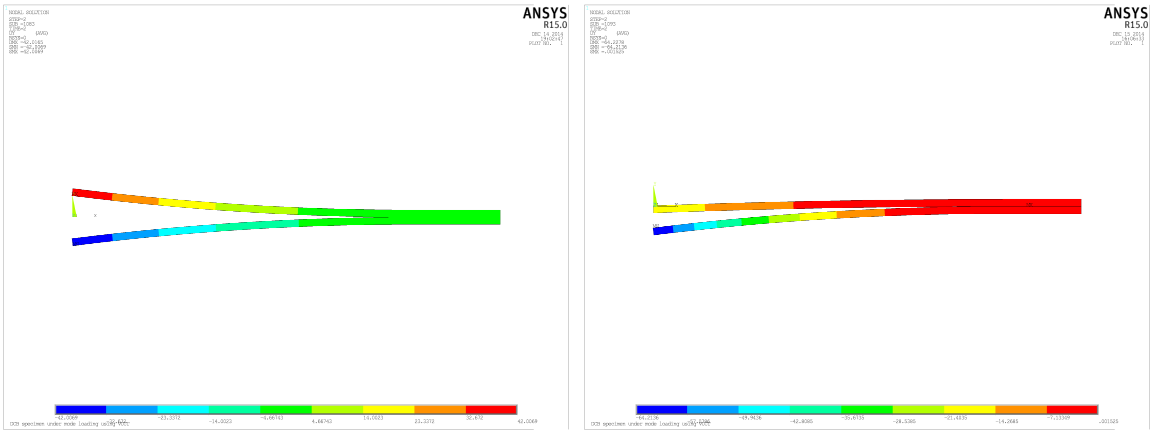


(a) Displaced shape of the specimen, for pure mode I and pure moment application

(b) Displaced shape of the specimen, for mode mixity with $\beta = 0.3$ and pure moment application

Figure 10.2: Plots made using the script

bending moment). The outline of the script is seen in figure 10.1.
The script can easily be expanded to 3D, but the focus has been on fast debugging in this work.

The test specimen has been analyzed for pure mode I using the energy release rate obtained by the tests, which was $\mathscr{G}_{Ic} = 1500 J/m^2$. In figure 10.2a the displaced shape for pure mode I loading is shown. Further a mixed mode analysis with $\beta = 0.3$, has been run with an assumed ERR for mode II of $\mathscr{G}_{IIc} = 1500 J/m^2$. The deformed shape can be seen in figure 10.2b.

The free body diagram for the script is seen in figure 10.3. Here the displacements $D^{\pm}$ are varied to obtain different mode mixities.

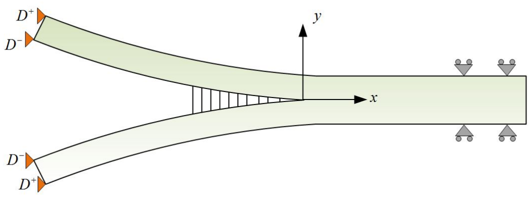


Figure 10.3: Free body diagram for finite element analysis using pure moment application

In table 10.1 a small segment of the script is given and explained in detail:

| | |
|---|---|
| AUTOTS,ON | Auto time stepping is set to on. This ensures better convergence. |
| TIME,1 | First load step is activated. |
| CINT,NEW,1 | Initiates a new calculation using the CINT with its parameters for fracture. |
| CINT,TYPE,VCCT | Uses the Virtual crack closure technique |
| CINT,CTNC,CRACK1 | A previously defined node component at the end of the precrack is called CRACK1 |
| CINT,SYMM,OFF | Defines if symmetry is used or not. Set to off here |
| CINT,NORM,0,2 | Defines the crack normal is in the y (2) direction. |
| CGROW,NEW,1 | Defines a new crack growth parameter set |
| CGROW,CID,1 | Crack contour integral calculation for ERR to be used in the fracture criterion calculation |
| CGROW,FCOPTION,MTAB,1 | Specifies that the tabular material data is used |
| CGROW,CPATH,CPATH | Defines that the crack path is a previously defined element component called CPATH |
| CGROW,DTIME,1.0e-4 | Initial time step when crack growth is initiated |
| CGROW,DTMIN,1.0e-4 | Minimum time step when crack growth is initiated |
| CGROW,DTMAX,1.0e-4 | Maximum time step when crack growth is initiated |
| NSUBST,15,15,15 | Number of substeps, initial, maximum and minimum |

Table 10.1: Small part of the script defining the crack growth parameters

## 10.3 Conclusion

Here a script has been made that utilizes the functionalities in the commercial code Ansys APDL release 15.0. The script is capable of handling wedge loaded DCB specimens as well as specimens subjected to pure moment. For the later these moments may range from mode I to mode II and mode mixities in-between. The critical energy release rate determined from mode I tests are introduced together with material properties and geometry parameters. These are then plotted against the tests for mode I loading.

# Chapter 11

# Conclusion and Discussion

The primary goal of this work was to develop a test tool able of testing DCB specimens under mode I, mode II and mode mixities in-between. The work is divided into three different parts, where the first part covers basic theory, which is needed to develop and verify the test tool. This includes the basics of the linear elastic fracture mechanics, which has been presented. Then followed by an introduction to establishing cohesive parameters for the damage zone during delamination of fiber reinforced composites. Further the approach to fitting the cohesive properties to a damage propagation criteria is explained.

In the second part, the concept of the new test tool is shown. Here a discussion about load introduction is given, and why pure moment is a requirement. This includes a discussion about previous test methods, which are shown in appendix A. Then a requirement specification is given and the chosen concept is presented. Other concepts as well as criteria for selecting the best concept can be found in appendix B. A detailed introduction to the finally developed concept is shown, where the details are explained. This is supported by analytic and finite element calculations, that are found in appendix E.

Furthermore the validation of the test tool is performed using a test device with strain gauges attached. First an analytic evaluation of the influence of the rotation of specimens is performed and what influence it has on moments, shear forces and normal forces in the specimens. Then the results from the strain gauge measurements are presented and evaluated against the introduced load from the test machine. Here it was observed that there was a good correlation between them. Finite element analysis was performed on one of the test specimen arms to find the maximum strain and displacement allowed for the test specimen. Also DIC was used to evaluate the test specimen. Here the strains from the strain gauges was compared to the DIC results. Even tough there is a large complexity in using DIC, the results where comparable.

Sources of error and future improvements to the test tool have been discussed. Here suggestions and observations are given, which could improve the test tool. One of the key issues is that the rollers should be redesigned and the bearings should be modified to reduce friction. Due to possible differences in loads between the right and left side of the test tool, which could introduce torsion, the ropes should not run on the same roller. This was alleviated in the tests by using silicone oil on all rollers. However for future test a more permanent solution should be made. The frictional force from the rollers were found by fabricating an interface, that could measure the load on the lower cross head and compare it with the load on the upper cross head. This difference was found to be approximately constant 10 $\pm 5\%$ of the load applied, which was not acceptable. Therefore the test principle was converted so the force in the ropes, were applied by the upper cross head only. Specimen fabrication was discussed as the test showed that they were to compliant during mode II and mode mixity testing. The brackets attached to the specimens were glued, screwed and attached using a combination of the two. However, it was observed, that for thin specimens different glue should be used, and recommendations were given.

In the third part, a test specification for testing is given. This includes the procedure in manufacturing the specimens, how to measure mode I, II and mode mixity crack propagation. Then the test results are presented. For mode I testing, 4 out of 6 tests were usable. Only two of the 6 tests achieved good and stable crack propagation. Here the force and crack tip opening were converted into the energy release rate as a function of opening. Fitting of data was performed and a critical energy release rate for mode I was found to be $\mathscr{G}_{Ic} = 1500 J/m^2$. For mode II testing, a phenomena was observed, where the laminate was bend at the point of attachment to the bracket. This was assumed to increase the crack initiation strength. No crack propagation was found. For mode mixity crack propagation was found for 1 specimen out of two tested. However both tests were aborted due to very large deflections. This was due to high compliance of the specimen tested. In order to be able to use the data found in tests, a finite element script has been made, capable of handling 2D analysis of specimens, subjected to wedge forces for mode I loading as well as pure moment loading with modes ranging from mode I to mode II. The script can use both the B-K criterion as well as the power law criterion to predict crack propagation.

## 11.1 Future work

One of the requirements towards the test tool, and one of the important criteria, was that it should be able to handle fatigue analysis. Fatigue analysis could only be performed with the actual specimens and in the spindle operated test machine. This meant that cross head displacements were very slow and displacements large. Therefore the use with fatigue analysis could not be validated. However there is a good assumption that it can be used with fatigue analysis for thicker specimens. This is recommended to study further.

Tracking displacements for mode mixity and mode II loading using DIC, turned out to be complex. Not only capturing enough stages (pictures) during the test with the needed precision, but also post treatment of data. For DIC, a program can be made that is able to sort and handle the data output from the test. Another idea for future work is to apply the established vision technique, and simply track clearly defined points on the specimens in order to calculate the displacements of these points. This technique does not require the high resolution from DIC, and is a lot faster since only data for the point displacements are needed.

The area of determining cohesive properties for unidirectional fiber reinforced composites is still not documented as well as the area for most metallic materials, so further work should be devoted to obtain knowledge about the damage properties using pure moment application. However in industry the layers are mostly off-axis, which results in orthotropic material properties, in contrast to the tested specimens. A large area of research is open for testing off-axis composite material properties using pure moment application. Here only recent research has been conducted but using the described wedge loading - and MMB method. This field can be expanded to cover fatigue loading and finite element implementation as well.

# Bibliography


T. L. Anderson. *Fracture Mechanics, Fundamentals and applications.* Taylor &. Francis group, 3rd edition, 2005.

Jens Henrik Andreasen. *Brudmekanik.* Aalborg Universitet, Aalborg, 2010.

Ansys. *Ansys Mechanical APDL structural analysis guide, release 15.0.* Ansys inc., 15.0 edition, 2014.

D5528 13 ASTM. Standard test method for mode i interlaminar fracture toughness of unidirectional fiber-reinforced polymer matrix composites. Technical report, 2007.

D6671 M06 ASTM. *Mixed Mode I - Mode II interlaminar fracture toughness of unidirectional Fiber reinforced Polymer Matrix Composites.* American Society of Testing Materials, 2006.

Brian Bak. Fracture mechanics for laminated composite structures. Technical report, Department of Mechanical and Manufacturing engineering, Aalborg University Denmark, 2012.

E. J. Barbero. *Finite Element Analysis of Composite Materials.* CRC Press, 1 edition, 2007.

G. I. Barenblatt. The mathematical theory of equilibrium cracks formed in brittle fracture. *Zhurnal Prikladnoy Mekhaniki i Tekhnicheskoy*, 1 (4):3–56, 1961.

M. L. Benzeggagh and M. Kenane. Measurement of mixed mode delamination fracture toughness of ud glass/epoxy composites with mixed mode bending apparatus. *Composites, Science and technology*, 56:439–449, 1996.

V. V Bolotin. Mechanics of delaminations in laminate composite structures. *Mechanics of composite materials*, 37:367–380, 2001.

P. P. Camanho and C. G. Davila. Mixed-mode decohesion finite elements for the simulation of delamination in composite materials. *NASA/TM-2002-211737*, 2002.

L. A. Carlson, J. W. Gillespie, and R. B. Pipes. On the analysis and design of the end notched flexure (enf) specimen for mode ii testing. *Int. J. Comp. Materials*, 20:594–604, 1986.

Leif A. Carlsson and John W. Gillespie. *Delaware composites design encyclopedia - Vol.6 Test Methods*. Technomic Publishing Company Inc., 1990.

Robert D. Cook. *Concepts and applications of finite element analysis*. John Wiley and Sons inc., 4 edition, 2002.

C. G. Davila, P. P. Camanho, and Moura M. F. Mixed mode decohesion elements for analyses of progressive delamination. *42nd AIAA/ASME/ASCE/AHS/ASC Structures, Structural and Dynamics conference*, 2001.

M. Dessureault and J. K. Spelt. Observations of fatigue crack initiation and propagation in an epoxy adhesive. *Int. J. Adhesion and Adhesives*, 17:183–195, 1997.

F. Ducept, P. Davies, and D. Gamby. An experimental study to validate tests used to determine mixed mode failure criteria of glass/epoxy composites. *Composites*, 28A:719–729, 1997.

Dominic Gates. Seatle Times, 2009. URL `http://seattletimes.com/html/boeingaerospace/2009565319_boeing30.html`.

James M. Gere and Barry J. Goodno. *Mechanics of Materials*. Cencage Learning, 8th si - edition edition, 2012.

X. N. Huang and D. Hull. Effects of fibre bridging on $g_{Ic}$ of a unidirectional glass/epoxy composite. *Composites, Science and technology*, 35:283–299, 1989.

ISO 15024 International Standard. *Fibre - reinforced plastic composites - Determination of mode I interlaminar fracture toughness GIc, for unidirectionally reinforced materials*. 1st edition, 2001.

Torben K. Jacobsen and Bent H. Sørensen. Mode i intra-laminar crack growth in composites - modelling of r-curves from measured bridging laws. *Composites Part A*, 32:1–11, 2001.

Z.-H. Jin and C. T. Sun. A comparison of cohesive zone modeling and classical fracture mechanics based on near tip stress field. *Int. J. of Solids and structures*, 43:1047–1060, 2005.

Arne Kildegaard. *Elasticitetsteori.* Aalborg Universitet, 5.1 edition, 2013.

Erwin Kreyzig. *Advanced Engineering Mathematics.* John Wiley and Sons inc., 10 edition, 2011.

Yeh-Hung Lai, Dwayne M. Rakestraw, and David A. Dillard. The cracked lap shear specimen revisited - a closed form solution. *Inernational journal of solids and structures*, 33:1725–1743, 1996.

Esben Lindgaard. Cohesive zone modeling with the finite element method. Technical report, Department of Mechanical and Manufacturing engineering, Aalborg University Denmark, 2012.

Stefan Mack. Eine vergleichende untersuchung der physikalisch chemischen prozesse an der grenzschicht direkt und anodischer verbundener festkoerper. *Verein Deutscher Ingenieure*, 1997.

D. Plausinus and J. K. Spelt. Application of a new constant g load-jig to creep crack growth in adhesive joints. *Int. J. Adhesion and Adhesives*, 15:225–232, 1995.

J. R. Rice. A path independent integral and the approximate analysis of strain concentration by notches and cracks. *Journal of applied mechanics*, 35(2):379–386, 1968.

Irving H. Shames and Clive L. Dym. *Energy and finite element method in structural engineering, SI edition.* Taylor and Francis Books inc., 1 edition, 2003.

S. M. Spearing and A. G. Evans. The role of fiber bridging in the delamination resistance of fiber - reinforced composites. *Acta metal mater.*, 40:2191–2199, 1992.

Bent F. Sørensen. Cohesive laws for assessment of material failure: Theory, experimental methods and application. Doctor of technices thesis, Risø DTU, 2010.

Bent F. Sørensen and Stergios Goutianos. Mixed mode cohesive law with interface dilatation. *Mechanics of Materials*, 70:76–93, 2014.

Bent F. Sørensen and Torben K. Jacobsen. Large-scale bridging in composites: R-curves and bridging laws. *Composites Part A: Applied Science and Manufacturing*, 29:1443–1451, 1998.

Bent F. Sørensen and Torben K. Jacobsen. Crack growth in composites: applicability of r-curves and bridging laws. *Plast Rubber Compos*, 29:119–133, 2000.

Bent F. Sørensen and Torben K. Jacobsen. Characterizing delamination of fibre composites by mixed mode cohesive laws. *Composites Science and Technology*, 69:445–456, 2009.

Bent F. Sørensen, Philippe Bretheh, and Peder Skov Hansen. Controlled crack growth in ceramics: The dcb specimen loaded with pure moments. *Journal of the European Ceramic Society*, 16:1021–1025, 1996.

Bent F. Sørensen, E. Kristofer Gamstedt, Rasmus C. Østergaard, and Stergios Goutianos. Micromechanical model of cross-over fibre bridging – prediction of mixed mode bridging laws. *Mechanics of Materials*, 40:220–234, 2008.

Kenneth Sørensen, Bent F.and Jørgensen, Torben K. Jacobsen, and Rasmus C. Østergaard. Dcb-specimen loaded with uneven bending moments. *Int. J. Fract*, 141:163–176, 2006.

Z. Suo, G. Bao, and B. Fan. Delamination r-curve phenomena due to damage. *J. Mech. Phys. Solids*, 40:1–16, 1992.

Michael A. Sutton, Jean Jose Orteu, and Hubert Schreier. *Image Correlation for Shape, Motion and Deformation Measurements*. Springer Verlag, 1 edition, 2009.

A Turon, P. P. Camanho, J. Costa, and C. G. Davila. A damage model for the simulation of delamination in advanced composites under variable-mode loading. *Mechanics of Materials*, 38:1072–1089, 2006.

Albert Travesa Turon. Simulation of delamination under quasi-static and fatigue loading using cohesive zone models. Doctor of philosophy thesis, Universitat de Girona, 2006.

Herbert Wittel, Dieter Muhs, Dieter Jannasch, and Joachim Vossiek. *Roloff/Matek Machinenelemente*. Springer Vieweg, 2013.

De Xie and Anthony M. Waas. Discrete cohesive zone model for mixed-mode fracture using finite element analysis. *Engineering Fracture Mechanics*, 73:1783–1796, 2006.

X. P. Xu and A. Needleman. Numerical simulations of fast crack growth in brittle solids. *J. Mech. Phys. Solids*, 42:1397–1434, 1994.

# Appendix A

# Previously developed test methods

## A.1 Mode I - Test methods

Here different test methods, that are exclusively developed for testing Mode I fracture in DCB specimens are presented.

### A.1.1 The wedge method

The DCB test method which is shown in figure A.1, is standardized by ASTM (ASTM, 2007) as well as ISO International Standard (2001).

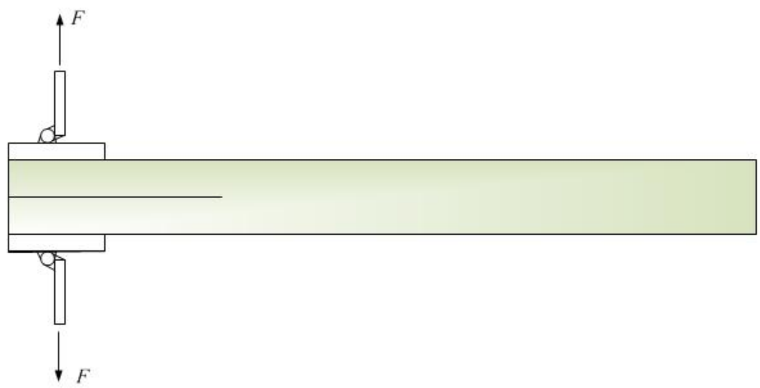


Figure A.1: The wedge method for pure mode I testing

This method uses a laminated part that is already pre-cracked. This pre-crack is made by using a thin Teflon film, which is inserted between the layers before the curing process. The specimen is fitted with hinges on both sides of the crack that are either glued or is fastened with a combination of glue and screws. These two free ends are then via the hinges connected to a tensile test machine. During the test the force and the crack length are monitored. This way the fracture toughness can be calculated, using the LEFM approach that was shown in eq. 5.2.

**The advantages are that:**

1. It is easy to install the specimen in a test machine.
2. No expensive test rig is needed.
3. It is easy to use with different test machines.
4. It is standardized by ASTM and ISO.

**The disadvantages are that:**

1. The crack front must be monitored real time, which can be difficult.
2. Nonlinearities can be present due to large deflection for low stiffness laminates.
3. The R - curve depends on the pre-crack length.
4. The crack growth is displacement based, which means that unstable crack growth might occur.

As mentioned, it has been proposed by (Jacobsen and Sørensen, 2001), that the angle of the DCB arms should be measured as it opens and rotates.

$$J = \frac{2P\theta}{b} \tag{A.1}$$

This way the energy release rate can be found using the $J$ - integral instead of using the LEFM approach $\mathscr{G}_R$. The LEFM approach requires a long precrack $a_0 > 0.25$m. Then the difference between the $J_R$ and $\mathscr{G}_R$ is less than 10%.

### A.1.2 The taper method

First developed by (Mack, 1997) the taper test method is used with electronic layered components (wafers). The method uses a very sharp tapered wedge that is pushed in between the layer of the two materials. Measuring the end opening, the force used $F$ and the crack length $a$, the free surface energy $\gamma_0$ can then be calculated. It has been proposed by (Mack, 1997) to use the method for laminated composites. This however would be difficult since the wedge would cut the bridging fibers as the taper progresses. Still the difficulties with measuring the crack length exists.

**The advantages are that:**

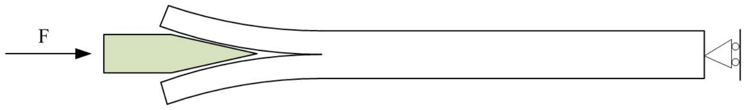


Figure A.2: The taper Method

1. It is easy to create a test tool
2. It is easy to measure the applied load $F$
3. It can be displacement controlled, using a clip on gauge and feedback into the test machine.

**The disadvantages are that:**

1. The taper can easily damage the fibers that are bridged between the layers.
2. It can be difficult to measure the crack length.
3. The test method could introduce buckling effects for DCB specimens.
4. It might be difficult to obtain stable crack growth.

## A.2 Mode II and mixed mode test methods

In this subsection different test methods, that are developed for testing Mode II and mixed mode (between Mode I and II) fracture in DCB specimens are presented.

### A.2.1 The crack lap shear method (CLS)

The CLS method used by (Lai et al., 1996), is only suitable for pure mode II testing. The method, used for testing adherents between layers, is based on constraining one beam, and subjecting the other beam to a tensile force or compression. The principle can be seen in figure A.3.

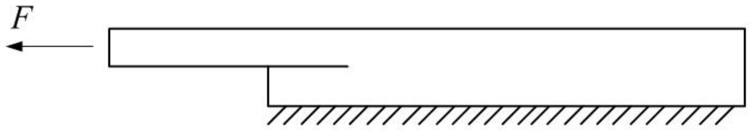


Figure A.3: The crack lap shear method

Using the force and the crack length, the energy release rate can then be calculated. The method however is impractical to use in the current work as it is not suitable with mode I or mode mixity.

**The advantages are that:**

1. It is easy to create a test tool.
2. It is easy to measure the applied load $F$ since it is directly connected to a test machine.
3. The tangential stress is measured directly for pure mode II or mode III.

**The disadvantages are that:**

1. Only applicable to single mode II or mode III loading

### A.2.2 The end notch flexure test (ENF) and Mixed mode bending test (MMB)

The end notch flexure test (ENF) is used by a lot of researchers for mode II testing. It is quite simple to set up, and is usable with a large range of test machines. Again the crack length $a$ must be monitored together with the load input $F$. This way the energy release rate $\mathscr{G}$ can be found. (Carlson et al., 1986) proposed a setup, were the principle can be seen in figure A.4.

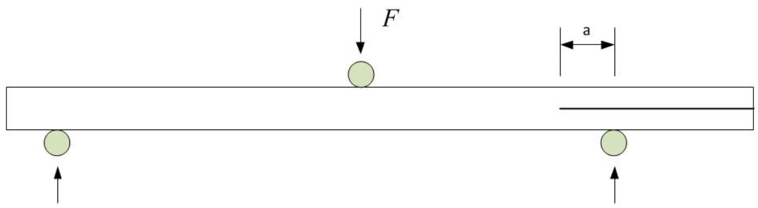


Figure A.4: The end notch flexure test method (ENF)

The method however cannot be used for mixed mode testing. Therefore the MMB method was developed (see figure A.5), based on a combination of the ENF and the wedge method, shown earlier. This is now standardized in for instance (ASTM, 2006).

**The advantages for the MMB test method is that:**

1. The test tool and method is standardized
2. It is easy to measure the applied load $F$

**The disadvantages are that:**

1. The crack length must be monitored real time.
2. The R - curves depend on the initial crack length.
3. Unsuitable for thick specimens as compressive loads in-plane into the laminate might create cracks, which make the overall structure more compliant.
4. Unstable crack growth might occur.

### A.2.3 Pure moment application

The test tool developed by Plausinus and Spelt (1995), were the first (as far as the author is aware of) to use a method where wires are used to create a state of pure moment on the DCB specimen. This method was later used by Dessureault and Spelt (1997) in fatigue studies of glued aluminum strips in a DCB configuration.

The method by Plausinus and Spelt (1995) was also used by Sørensen et al. (1996) in the analysis of ceramic DCB specimens. However in layered composite materials,

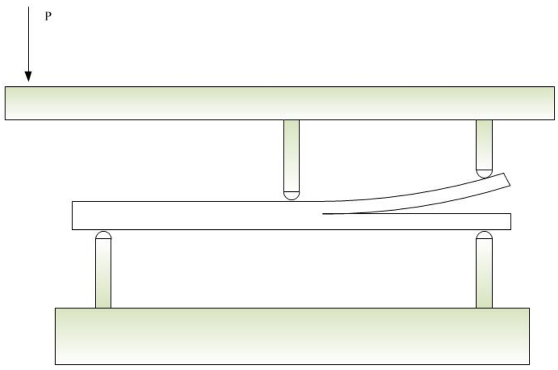


Figure A.5: Mixed Mode Bending test method

were the rotations and displacements can be large, Sørensen and Jacobsen (1998) developed a new loading method with moment arms attached perpendicular to the specimen as shown in figure A.6. Here the upper cross head where the load cells are attached, is moved upwards to increase the load on the specimen.

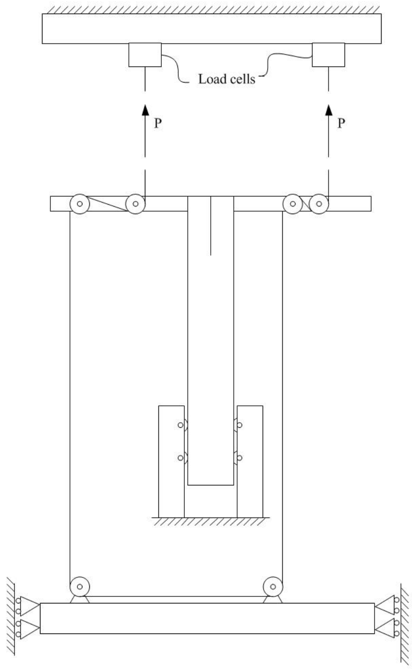


Figure A.6: Mixed mode test rig by Sørensen et al. (1996)

This method can by varying the distances between the rollers and the orientation of the wire produce a pure moment to the test specimen, varying from pure mode I to pure mode II.

The test rig (figure A.6) shows only a few weaknesses, which are that the moment applied to the specimen varies with the rotation of the moment arms. A solution that was proposed is to angle the moment arms initially opposite to the forced rotation. Thereby the error in moment due to the rotation can be divided by 2. Another requirement is that the wires must be vertical or nearly vertical through the entire test. Otherwise unwanted shear and normal forces are introduced. This demands for long wires since the wire angle is directly depending on the horizontal displacement of the DCB cracked arms. The relation between opening (horizontal deformation) of one arm and the moment is:

$$u(a) = \frac{M \cdot a^2}{E \cdot I} \tag{A.2}$$

Where $M$ is the applied moment, $a$ is the crack length and $E \cdot I$ is the stiffness of the arm.

In the following a thorough analysis of the setup used by Sørensen and Jacobsen (1998) and his team is performed. First pure mode I loading is considered, then mixed mode and pure mode II loading is considered.

### Study of the influence of angles

In order to be able to evaluate the concept in detail, a study of the influence on the interface loads between the moment arm and DCB specimen, based on the angles that the moment arms form with their initial position is presented. This has a large impact on measuring the loads and how they vary during tests.

In the following, free body diagrams are shown for the moment arms attached to the specimen, subjected to various rotations and force angles. Using the free body diagrams a study of the interface forces on the boundary between the moment arm and specimen is performed.

Generally the rotation of the moment arms are directly associated with the curvature of the beam. This can, under the assumption of small displacements and rotations as well as neglecting the deformation of the moment arm itself, be described as:

$$\theta \approx tan(\theta) = \frac{dv}{dx} = \frac{1}{E \cdot I} \int M(x)dx \tag{A.3}$$

Here the moment $M$ is the moment at the interface between arm and specimen. $E$ is the modulus of elasticity of the composite beam, and $I$ is the moment of inertia for the composite beam.

### Mode I - loading

The moment arms of the setup are shown in figure A.7 for a Mode I crack opening condition:

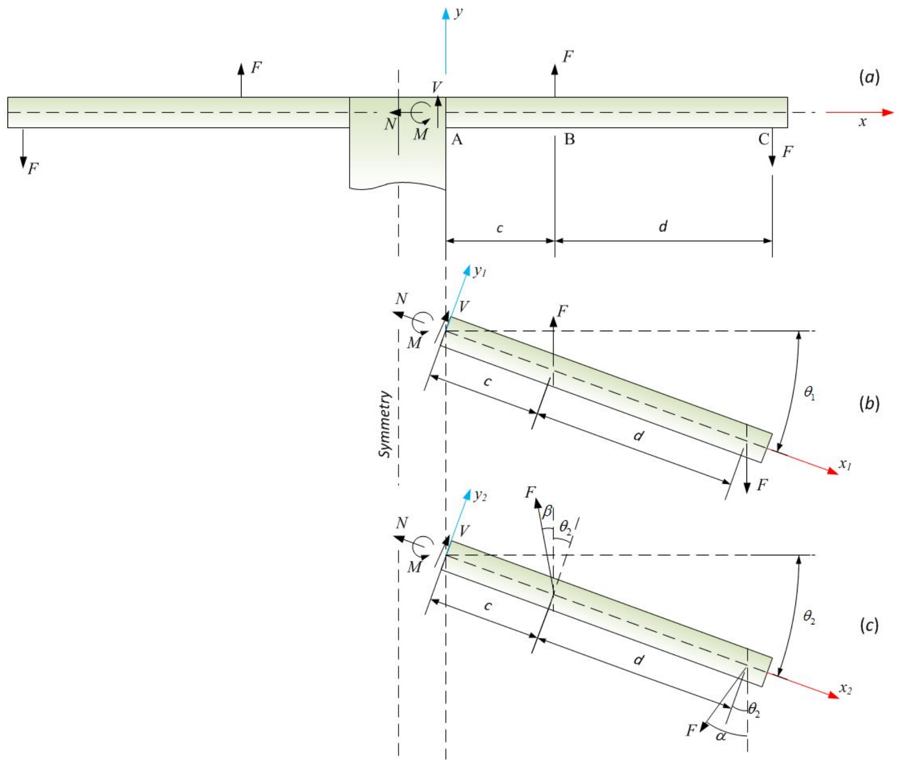


Figure A.7: Mode I free body diagram of moment arms under different rotations

Using the equilibrium equations for figure A.7(a) it shows:

$$N = 0 \tag{A.4}$$

$$V = 0 \tag{A.5}$$

$$M = F \cdot d \tag{A.6}$$

For the next situation, shown in figure A.7(b), the forces remain in a vertical orientation and the beam rotates $\theta_1$ degree. This gives the following:

$$N = 0 \tag{A.7}$$

$$V = 0 \tag{A.8}$$

$$M = F \cdot d \cdot cos(\theta_1) \tag{A.9}$$

This means that for the deflected situation the moment now becomes a function of the rotational angle $\theta_1$. In order to find out what influence this has on the moment, a unit force $F = 1$, and $d = 1$ has been applied, were the moment $M$ has been plotted as a function of angle between 0 and 45°

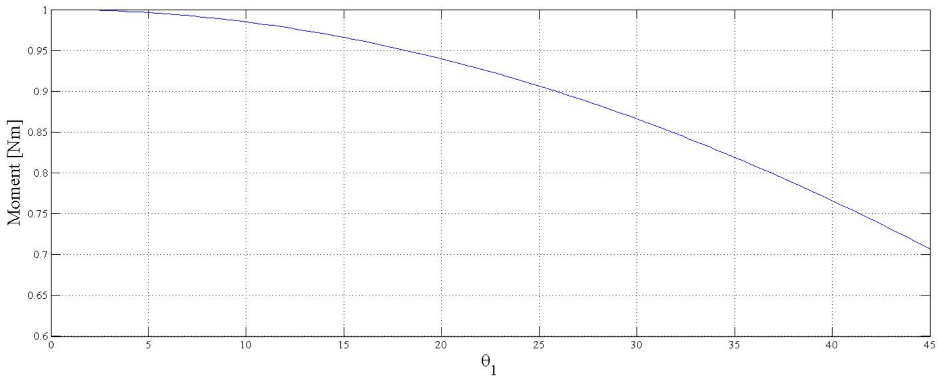


Figure A.8: The moment at the interface as a function of angle $\theta_1$

This shows that, for mode I testing, if the rotational angle is kept below 20°, the error in moment is less than 6%, which is acceptable. This is also what was shown by Sørensen et al. (2006).

In the last situation, shown in figure A.7(c), the beam rotates $\theta_2$ degrees, as well as the forces are rotated the arbitrary angles $\alpha$ and $\beta$ due to rotation of the wires. Now the interface forces are found as:

$$N = F \cdot sin(\alpha - \theta_2) - F \cdot sin(\beta + \theta_2) \tag{A.10}$$

$$V = F \cdot cos(\alpha - \theta_2) - F \cdot cos(\beta + \theta_2) \tag{A.11}$$

$$M = F \cdot cos(\alpha - \theta_2) \cdot c + F \cdot cos(\alpha - \theta_2) \cdot d - F \cdot cos(\theta_2 + \beta) \cdot c \tag{A.12}$$

As can be seen, the shear force and normal force becomes nonzero, as well as the moment is now depending on the angles. To show the effect on the interface forces, based on the angles $\alpha$ and $\beta$, varying $\pm 10°$, the following 3D plots are made for the normal force $N$, shear force $V$ and the moment $M$ using a unit force of 1 $N$, distances $c = 1$, $d = 1$ and a fixed angle $\theta_2 = 15°$. This is shown in figure A.9.
It shows that for a change in angles $\alpha$ and $\beta$ between $\pm 5°$, normal forces will be introduced to the interface, varying between $\pm 17\%$ of the force $F$ applied.
The shear force in the interface is affected less, but still varying between $\pm 5\%$ of the force $F$ applied.

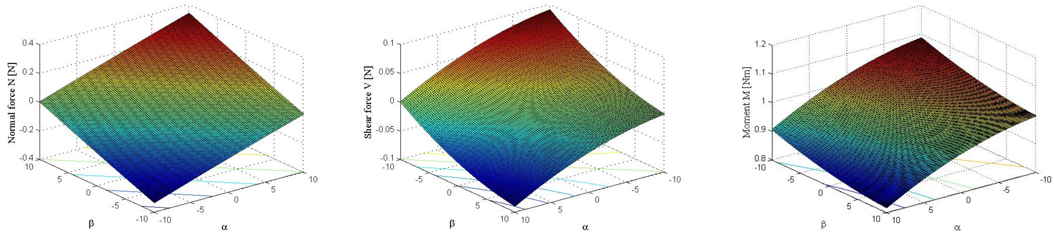


(a) (b) (c)

Figure A.9: Normal force, shear force and moment dependance on angles $\alpha$ and $\beta$

The moment $M$ is not only affected by the angle $\theta_2$ as shown previously in figure A.8, but is also depending on the two angles $\alpha$ and $\beta$. With the two angles set to vary between $\pm 5°$, the moment varies $-11\%$ up to $3\%$ of the nominal moment ($M = F \cdot d$), assuming that $c = d$. This means that there is no linear relation between the moment $M$ and the three angles $\alpha$, $\beta$ and $\theta_2$.

To illustrate this the moment has been plotted the same way as above, just using an angle $\theta_2 = 0°$. This is shown below in figure A.10, were the angles $\alpha$ and $\beta$ are varied $\pm 10°$.

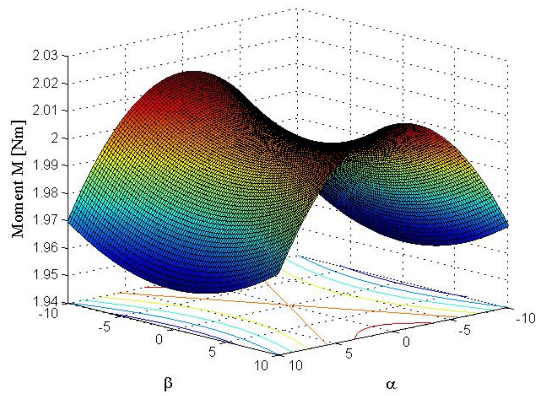


Figure A.10: The moment as a function of the angles $\alpha$ and $\beta$ with $\theta_2 = 0°$

This shows that the setup made by Sørensen et al. (2006) and his team is fairly accurate under the requirement that the wires are long or that the specimen is stiff. This way the horizontal opening of the specimen is small and hence the rotation of the wires will be small. It also shows that the proposed method by (Sørensen et al., 2006), of pre-rotating the moment arms to an initial angle equal to the final angle, will divide the error by two.

### Mixed mode - and mode II loading

For mixed mode loading the same effects as for mode I loading can be observed as presented previously. Three free body diagrams has been created. Here the left moment arm is affected by a lower moment or the opposite (pure mode II), compared to the right arm. Therefore it is shown as rotating less. The free body diagrams are shown in figure A.11.

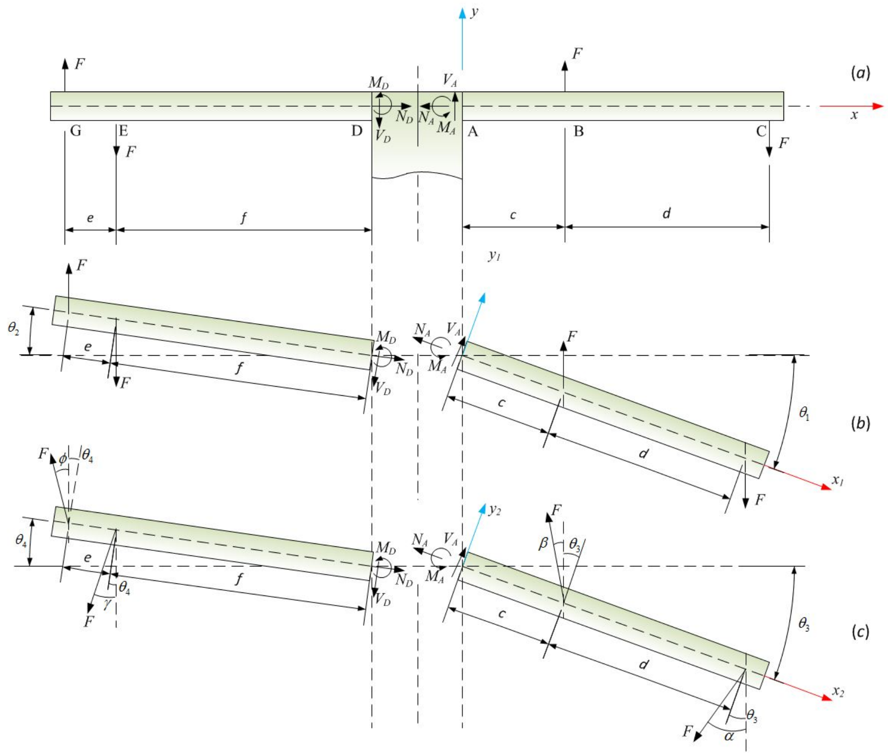

Figure A.11: Mixed mode free body diagram of moment arms under different rotations

Using the equilibrium equations for figure A.11(a) the following is obtained:

$$N_A = N_D = 0 \tag{A.13}$$
$$V_A = V_D = 0 \tag{A.14}$$
$$M_A = F \cdot d \tag{A.15}$$
$$M_D = F \cdot e \tag{A.16}$$

For the next situation, shown in figure A.11(b), the forces remain in a vertical orientation and the beams rotate $\theta_1$ and $\theta_2$ degrees respectively. This gives the following:

$$N_A = N_D = 0 \tag{A.17}$$

$$V_A = V_D = 0 \tag{A.18}$$

$$M_A = F\cdot d\cdot cos(\theta_1) \tag{A.19}$$

$$M_D = F\cdot e\cdot cos(\theta_2) \tag{A.20}$$

This shows that the two moments will not only vary based on the distances $d$, and $e$, but also on the angles $\theta_1$ and $\theta_2$. The influence of these rotational angles on the moment can be seen in figure A.12 below, were the normalized moment ($\frac{M_A}{M_D}$), using $d = e = 1$ and the force $F = 1$, is plotted against the two angles $\theta_1$ and $\theta_2$, varying from $-20°$ to $20°$.

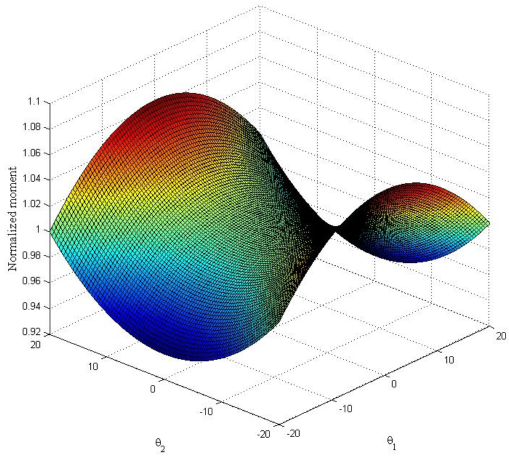


Figure A.12: The normalized moment, shows the ratio between the two moments as a function of the angles $\theta_1$ and $\theta_2$

.

It shows that for rotations of one moment arm up to 20°, and the other at 0° the error in moment is up to approximately 6.5%. This is regarded as negligible if the angles of the wires are kept at $\approx$ 0°. For thicker laminates the rotations will be less than 20° from the initial angle, and the error induced will be even smaller. If thinner laminates are analyzed it may introduce errors in the measured moments, and thereby it will be difficult to obtain steady crack growth.

In the last situation, shown in figure A.11(c), the beams rotates $\theta_3$ and $\theta_4$ degrees respectively. Furthermore the forces are rotated the arbitrary angles $\alpha$ and $\beta$ for beam $A - C$ and the angles $\gamma$ and $\phi$ for the beam $D - G$. Now the interface forces are found as:

$$N_A = F \cdot sin(\alpha - \theta_3) - F \cdot sin(\beta + \theta_3) \tag{A.21}$$

$$V_A = F \cdot cos(\alpha - \theta_3) - F \cdot cos(\beta + \theta_3) \tag{A.22}$$

$$M_A = F \cdot cos(\alpha - \theta_3) \cdot c + F \cdot cos(\alpha - \theta_3) \cdot d - F \cdot cos(\theta_3 + \beta) \cdot c \tag{A.23}$$

$$N_D = F \cdot sin(\phi + \theta_4) + F \cdot sin(\gamma - \theta_4) \tag{A.24}$$

$$V_D = F \cdot cos(\phi + \theta_4) - F \cdot cos(\gamma - \theta_4) \tag{A.25}$$

$$M_D = F \cdot cos(\phi + \theta_4) \cdot f + F \cdot cos(\phi + \theta_4) \cdot e - F \cdot cos(\gamma - \theta_4) \cdot f \tag{A.26}$$

This shows that the normal and shear forces as well as moments will depend on all the angles, which makes it difficult to control.

For mode II loading the angles $\theta_3 = \theta_4$.

**Sum up**

For mode I tests it could be seen in figure A.8, that it is acceptable to use the moment arm approach, under the condition that the forces are kept close to their initial angle ($\alpha, \beta \leqslant 5°$), through the entire test. Furthermore the angular rotations should be kept below 15°, which would keep the overall error in moment below $\approx 11\%$.

For mixed mode loading or mode II ($\theta_3 = \theta_4$, $e = d$, $c = f$ in figure A.11), the rotational angles, $\theta$ and force angles $\alpha$, $\beta$, $\phi$ and $\gamma$ should, as with mode I loading, be kept below 15° and 5° respectively, through the entire test. If the rotational angle is higher than 15°, which could occur in for instance thin specimens, the method of pre-setting the moment arms at an opposite angle can be a solution.

# Appendix B

# Concepts

## B.1 Introduction

In this appendix the different concepts for the test tool is presented. For all concepts presented here the requirements presented in section 5.3 must be fulfilled.
The concepts are presented in sections and numbered as for instance *Concept 1*. This does not imply that it is the best concept, but it only reefers to a number. Some of the concepts are developed further, in order to utilize some of the main ideas. Then these concepts are presented in sub sections (for instance *Concept 1.1*), in order to keep track on their origin.

The concepts are divided into two main groups:

1. Test tools that can be used as stand alone.
2. Test tools that utilize an external test machine.

In every section and subsection, the current concept is presented in an introduction describing the main functionalities. Then a list of drawbacks and benefits is presented and finally a small conclusion is given.
In the end all the concepts are given a grade in a morphological grading chart, and the best concept is found based on the criteria given.

## B.2 Concepts seen as stand alone systems

The main idea of having stand alone systems is that, the test rig does not depend on an available test machine for testing and that dedicated loading systems can be created. However it can be very costly to purchase the load cells, motors and other equipment to drive the system. Furthermore, software that controls the actuators and other machinery must work together with the data collection software. This might also increase the costs of the system.

### B.2.1 Concept 1

Concept 1 is based on using gear motors to create the moment that is applied to the ends of the free arms. The principle is sketched in figure B.1.

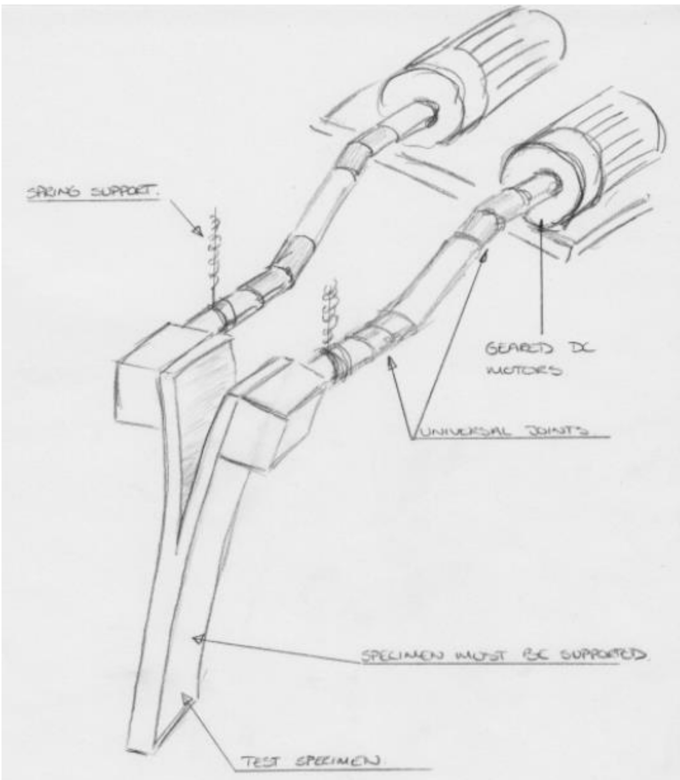


Figure B.1: Sketch of concept 1

The concept utilizes two individual geared step motors, that drives two shafts that are connected to the specimen. In order to take into account the opening of the specimens, two u-joints are inserted. If only one u - joint were inserted, there would be a large error in moment when turned. As rotating the u - joint, the input speed $\omega_1$ (figure B.2) is not the same as the output speed $\omega_2$. If the input shaft is rotated

$\phi_1$, then the output angle $\phi_2$ will depend on the angle $\alpha$ with the following minimum and maximum values (Wittel et al., 2013):

$$\phi_{2\text{max}} = \frac{\phi_1}{cos(\alpha)}; \qquad \phi_{2\text{min}} = \phi_1 \cdot cos(\alpha) \tag{B.1}$$

With the use of two joints the error can be removed. However in order to do this, a number of requirements must be fulfilled (Wittel et al., 2013):

- All the shaft parts (1, 2, and 3) must lie in the same plane. See figure B.2
- The angle $\alpha$ must be the same for both shafts.
- The two u - joints must be in the same plane. I.e. out of plane angles are not permitted.

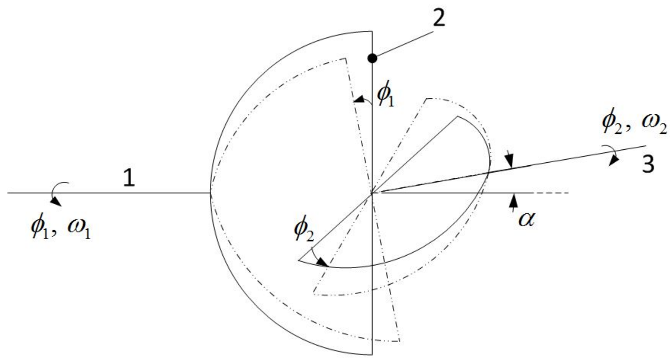


Figure B.2: u- joint free body diagram

Because of the angle $\alpha$ in figure B.3b, the connection with the specimen is subjected to moments about the $x$ and $y$ axis. Therefore a bearing system must be inserted that allows for translations in all directions except $z$. But no rotation is allowed about the $x$ and $y$ axis. One idea for a planer mechanism is the one shown in figure B.5.

Another problem arises in pure mode II loading, as can be seen in figure B.6, were $\beta$ now has a value. Hence the rotation of the two DCB specimen arms do not follow each other.

In order to track the moments and rotations applied, a digital torque transducer could be used, as for instance the T12 from HBM, seen in figure B.4.

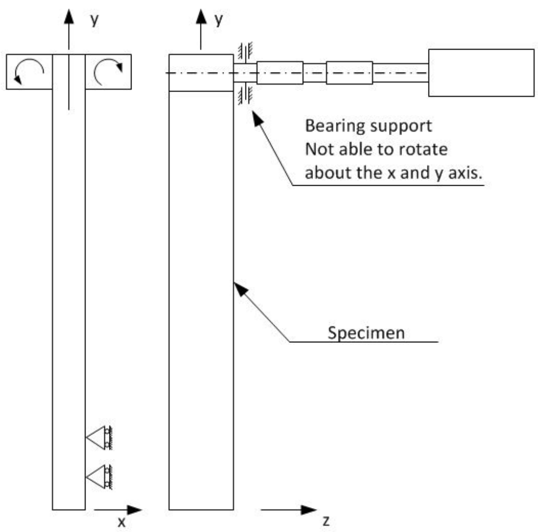


(a) Concept 1 FBD Side view

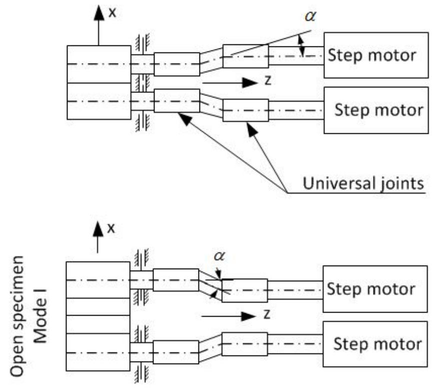


(b) Concept 1 FBD Top view

Figure B.3: Concept 1 Free body diagram

Figure B.4: Digital torque transducer T12 from HBM.com

**The advantages of the system are that:**

1. There is no size restriction on the specimens - The moment from a geared DC motor can be very large.

2. If the specimen deflects a small ammount the effect from the U-joints do not play any role.

**The disadvantages of the system are that:**

1. It does not support fatigue analysis directly.

2. Handling communication between the motor control and data acquisition software can be a challenge.

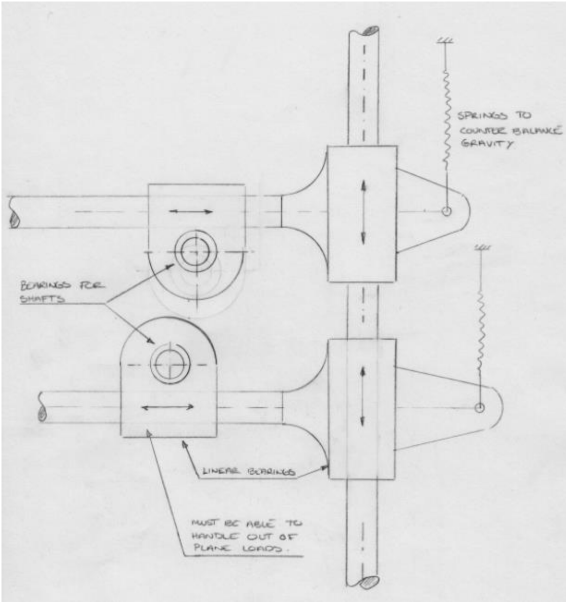


Figure B.5: Sketch of Planar Mechanism

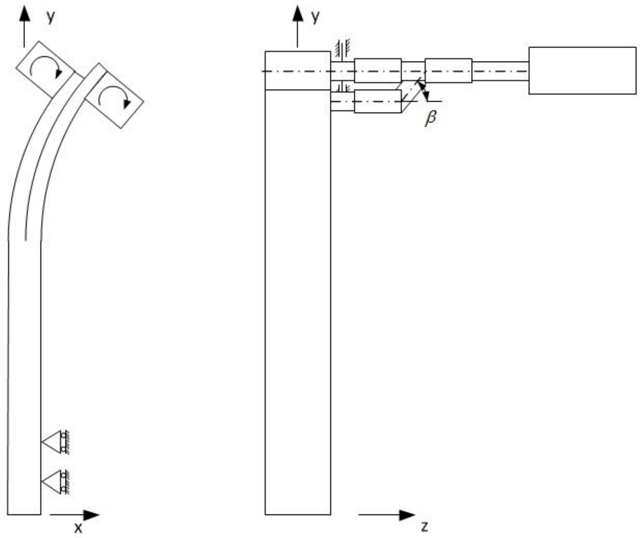


Figure B.6: Concept 4 subjected to pure mode II

3. It can not be used with smaller specimens as the large displacements will introduce angles between the shaft parts.

Concept 1 builds on the idea of using electrical motors to apply the moment directly to the specimen being tested. Doing this, problems with moments not being constant and wire angles is diminished. However since it does not support fatigue analysis directly this concept do not fulfill the requirement specification listed in section 5.3.

### Concept 1.1

Concept 1.1 is a spin off from concept 1. Instead of fixing the motors to a non movable base, they are moving with the specimen moment arm interface. This is seen in figure B.7.

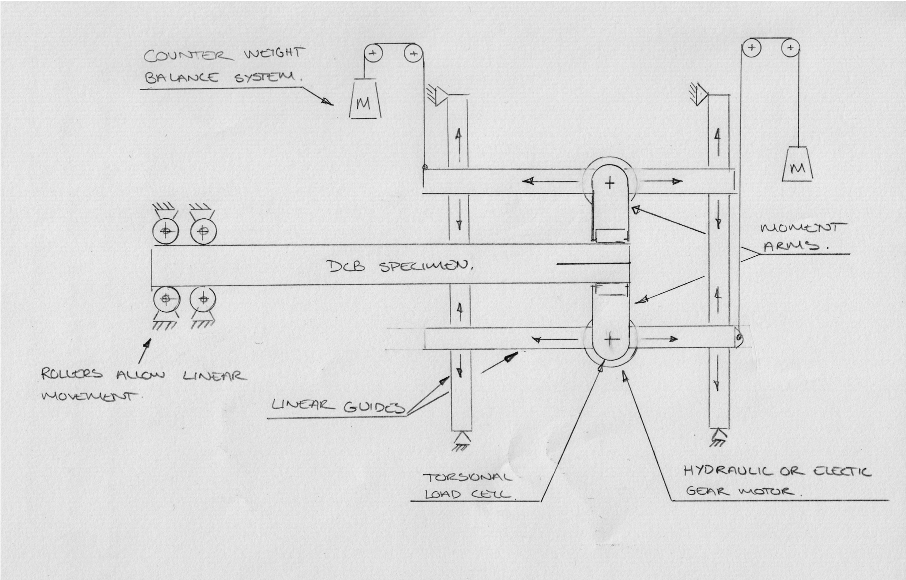


Figure B.7: Sketch of a stand alone test machine

The deflected shape and position of the different parts can be seen below in figure B.8.

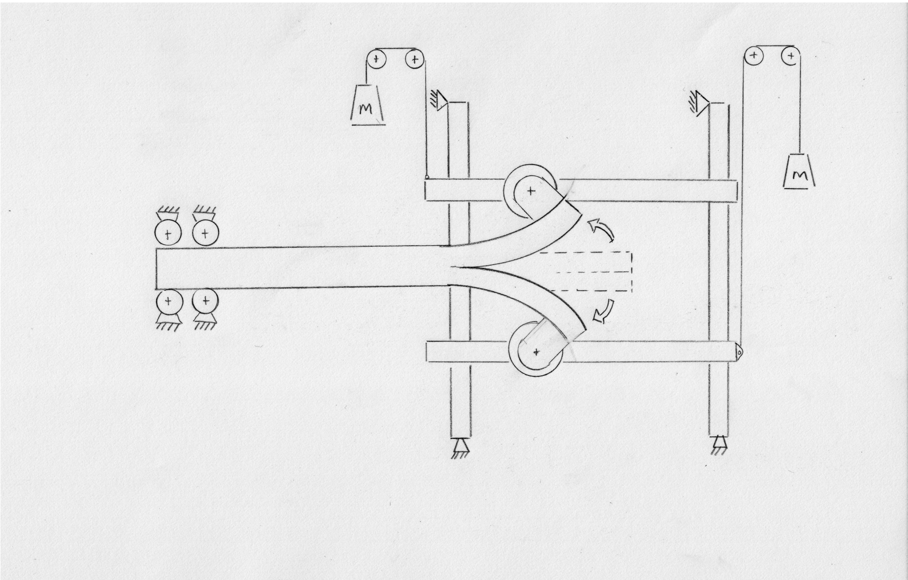


Figure B.8: Deflected shape of the specimen

The system works using a principle were electric gear motors or hydraulic motors are connected directly to the specimen using short moment arms. The motors are

suspended in a linear guide system as proposed in figure B.5 or simply using ordinary linear guides. In order to balance the loads, counterweights must be used or the system, could be positioned horizontally, so that figure B.7 would be seen from above. In order to make it capable of fatigue loading, a system like the 560LTD200 from [http://www.testresources.net/] could be stripped down and rebuilt to the new setup. These electric motors can fatigue load the DCB specimens with frequencies up to 30 Hz and 281 Nm. If higher moment loads are needed, then a hydraulic system could be employed.
On the downside is the costs of these components. The electromechanical actuators are the cheaper option and a system composed of two units is estimated to around DKK 500.000. If hydraulic motors servo valves etc. is used, the system cost could be well over DKK 1.000.000.
Another drawback is that it is quite unclear how fast the fatigue loading can be performed. There will be a lot of mass that needs to be moved fast, which might introduce spurious shear and normal forces into the system regardless of how frictionless the linear guides are performing.

**The advantages of the system are that:**

1. There is in genreral no size restriction on the specimens - The drive units can be hydraulic which can produce very large moments.

2. Existing test equipment can be bought from suppliers and modified to fit this testing rig. This also enables the use of existing motor controllers and software.

3. No spurious shear or normal forces will be introduced as the drive units are placed directly with the specimen arms.

**The disadvantages of the system are that:**

1. During fatigue analysis directly it is unclear if the mass of the drive units will influence the test specimen.

2. It will be very expensive.

Concept 1.1 shows a test rig where moments are applied directly to the specimen through either electrical or hydraulic drive units. Existing test equipment can be purchased and adapted to fit this test tool.

### B.2.2 Concept 2

Concept 2, shown in figure B.9a, is based on having a drive mechanism, electrical or hydraulic, that is connected to a gearwheel through a tooth belt or chain. The gearwheel is then connected to the free ends of the specimen.

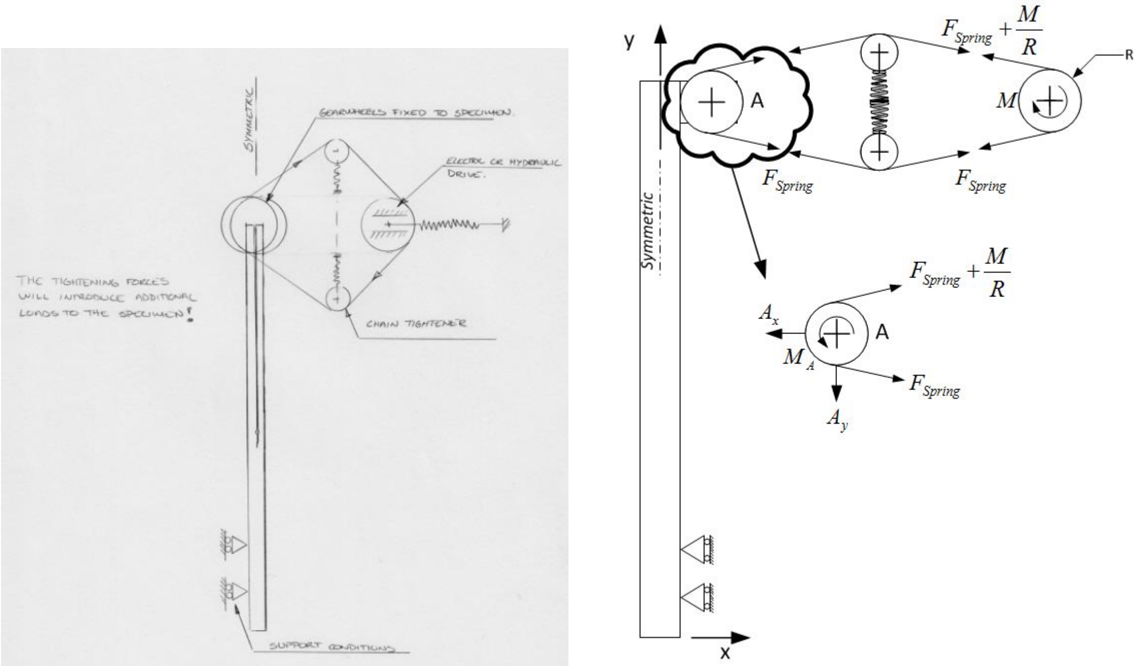


(a) Sketch of concept 2

(b) Concept 2 FBD

Figure B.9: Concept 2

Regardless if the load input will be hydraulic or electric, it will as intended introduce a moment $M_A$. Furthermore it is inevitable that it will introduce a shear load to the system $A_x$ and $A_y$ as shown in figure B.9b. Therefore *the concept is rendered useless and not developed further in detail!*.

## B.3 Concepts utilizing an external test machine

The main principle for the concepts presented in the coming sections is that they all utilize an external test machine. This can either be a machine for static tests or dynamic (fatigue) tests. The main reason for utilizing an external test machine, is because of the economical aspects. They are already installed with load cells, and actuators as well as the accompanying test software.

### B.3.1 Concept 3

Concept 3 is based on the method previously shown in figure A.6, which was developed by (Sørensen and Jacobsen, 1998) and (Jacobsen and Sørensen, 2001). Instead of using a wire mechanism, it is replaced using fixed arms. To explain the concept, which is shown in figure B.10, starting from the top and move down through the structure. The top is connected to a tensile test machine, which transfers the force into a horizontal bar where two linear bearings are attached to it. The idea with these bearings is that they should always make sure that the upper arms are vertical in order to reduce the force angles as described in the requirement specification. Through these bearings the upper connection arms are connected with the moment arms, that again is attached to the specimen. To create the force pair, the lower connection arms are connected to the main structure. The test tool is then connected to the lower part of the test machine. The lower connection arms could also be located in some sort of sliding mechanism, so that they would remain in their initial position. However it is unclear if the linear bearings or sliding mechanism has a tendency to stick, which could very easily result in angles different from the initial. The force needed to make them vertical or bring the support into place is very small, i.e. $F_x = F \cdot sin(\theta)$. This can be seen figure B.11b.
Ideally the solid connectors as seen in figure B.10, would always be vertical. However the horizontal forces will only be a fraction of the vertical force. This could in worst case mean that different loads will be subjected to the two moment arms attached to the specimen.

**The advantages of the system are that:**

1. It is using a mechanism that can have a very high stiffness
2. Adjustable to various specimen geometries
3. Connection to the test machine can be created easily

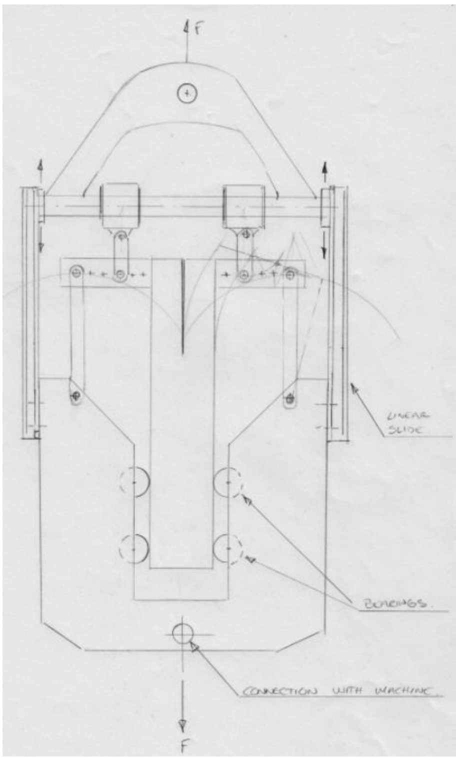


Figure B.10: Sketch of concept 3

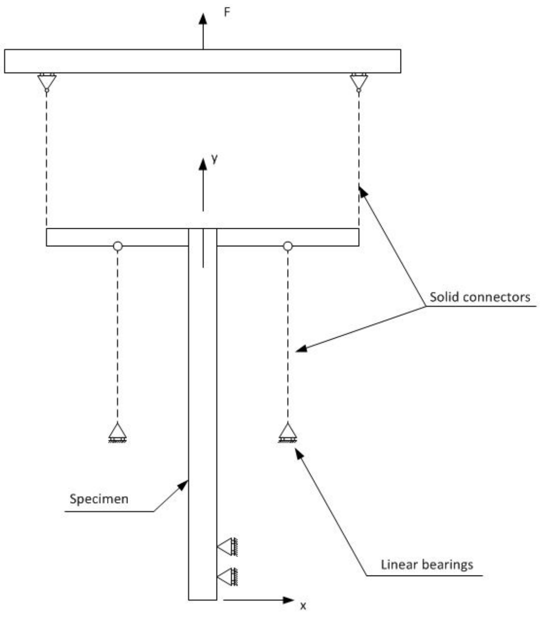


(a) Concept 3 FBD Closed

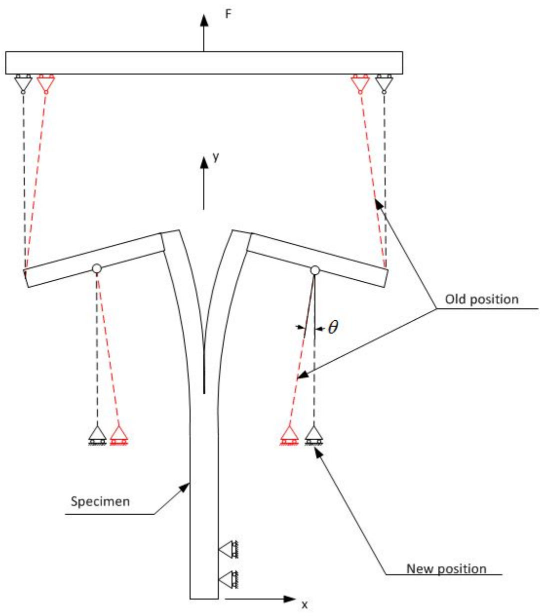


(b) Concept 3 FBD Open

Figure B.11: Concept 3 Free body diagram

**The drawbacks of the system are that:**

1. The weight of the structure could cause a problem in fatigue analysis, however

it has a very high stiffness.

2. It is unclear if the vertical arms will stay vertical under load or if some sort of stick slip behavior will be observed, which could result in unwanted angles.

3. The size of the structure does not allow for large displacements which will be seen with thin specimens

4. A large window test machine must be used.

The concept is only suitable as a test tool, if used with a large window test machine. Furthermore the test specimens should be quite thick, as the rotations of the test arms should be minimized as much as possible because if large rotations occur, spurious shear and normal forces are introduced.

### B.3.2 Concept 4

Concept 4 is based on the method shown below in figure B.12. It is a spin off, from the test rig made by (Jacobsen and Sørensen, 2001). The difference is that, the intention with this concept is, to build it into or connect it to a standard test machine. Opposed to the existing solution, that is stand alone.

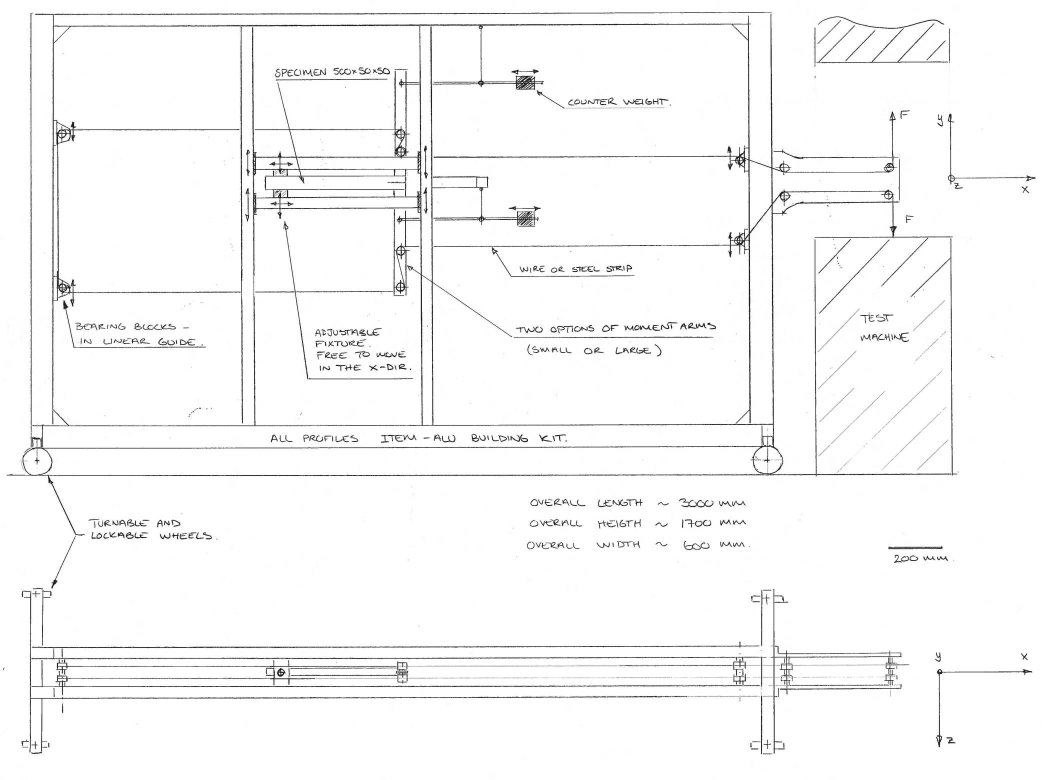


Figure B.12: Side view of concept 4

A sketch of the DCB specimen under mode I loading can be seen in B.13 and in B.14 for mixed mode loading. Please note, that the sketches only reefer to the problem with the introduction of angles and hence spurious shear and normal forces and not the concept itself.

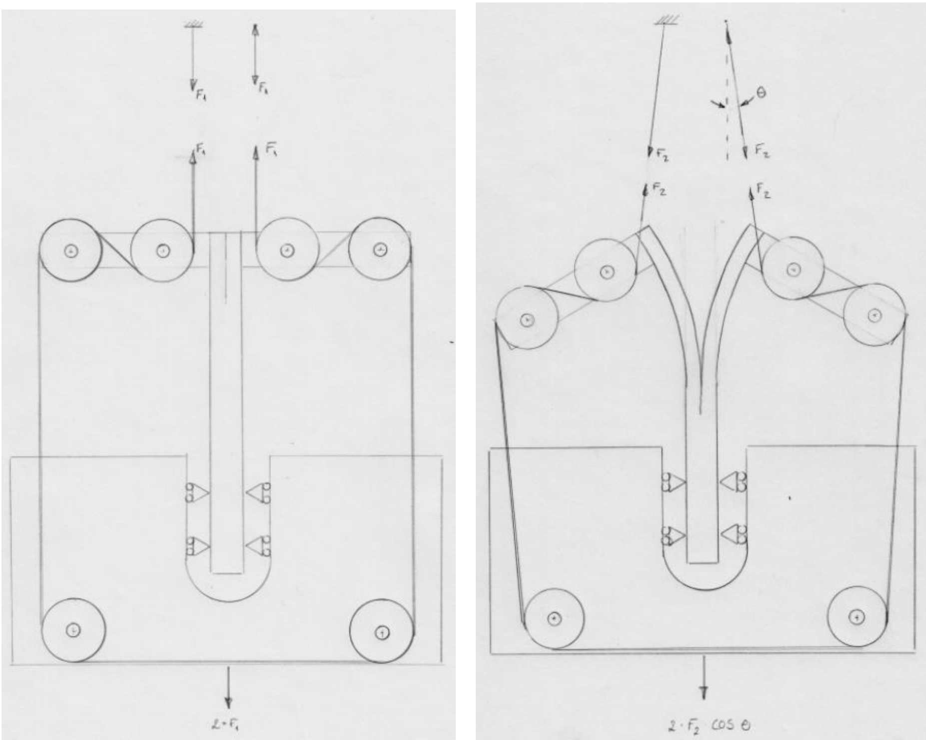

(a) (b)

Figure B.13: Sketch of concept 4, shown in a deformed and undeformed state

Explaining the concept in detail, and starting with the attachment of the test tool to the test machine. The two wire ends are attached to the upper and lower cross heads of the test machine. Running over a set of rollers, they are connected to the moment arms of the specimen. The wire is then creating the moment in the same way as shown previously in figure A.6. This way pure moment is created and it can be used for most normal sized test machines and for loading modes ranging from pure mode I to pure mode II.

**The advantages of the system are that:**

1. It is easy to change the specimen that is tested.

2. It can be adapted to a lot of different sizes of specimens.

3. The concept is proven to work by (Sørensen and Jacobsen, 2009).

4. The structure could be built with an aluminum building kit, which makes it easy to modify and adjust.

**The disadvantages of the system are that:**

1. It will be a large structure, which is not easy to handle. It is also difficult to move the structure around in a confined laboratory environment or find the space for it.

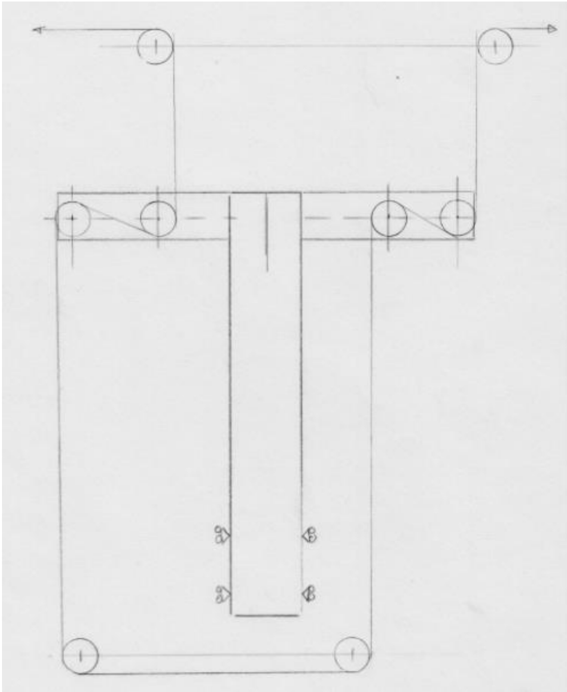

Figure B.14: Sketch of concept 4 for mixed mode loading

2. The moment is depending on the angle as described earlier.

3. It will only allow for low frequencies in testing due to the system with wires and rollers. However the system has been proven valid to use with fatigue as demonstrated by Plausinus and Spelt (1995).

4. The counterweights might be a problem in fatigue testing, but can be replaced by a spring mechanism.

The concept shown here is in general terms the same as developed by Bent Sørensen and his team. However it can be connected to a normal test machine or fatigue testing machines as long as the requirement for the test machine window opening (space between the crossheads) is fulfilled.

### B.3.3 Concept 5

Concept 5 again builds upon the idea of using a wire mechanism to introduce the moment to the test specimen. The problem with wire angles as outlined in figure B.13b, is due to the lateral deflection of the DCB specimen when it opens. In order to avoid this the moment arms are kept parallel to the DCB specimen. Using this method, the wire length is reduced drastically compared to *Concept 4*. A sketch of the system for mode I and mode II loading is shown in figure B.15.

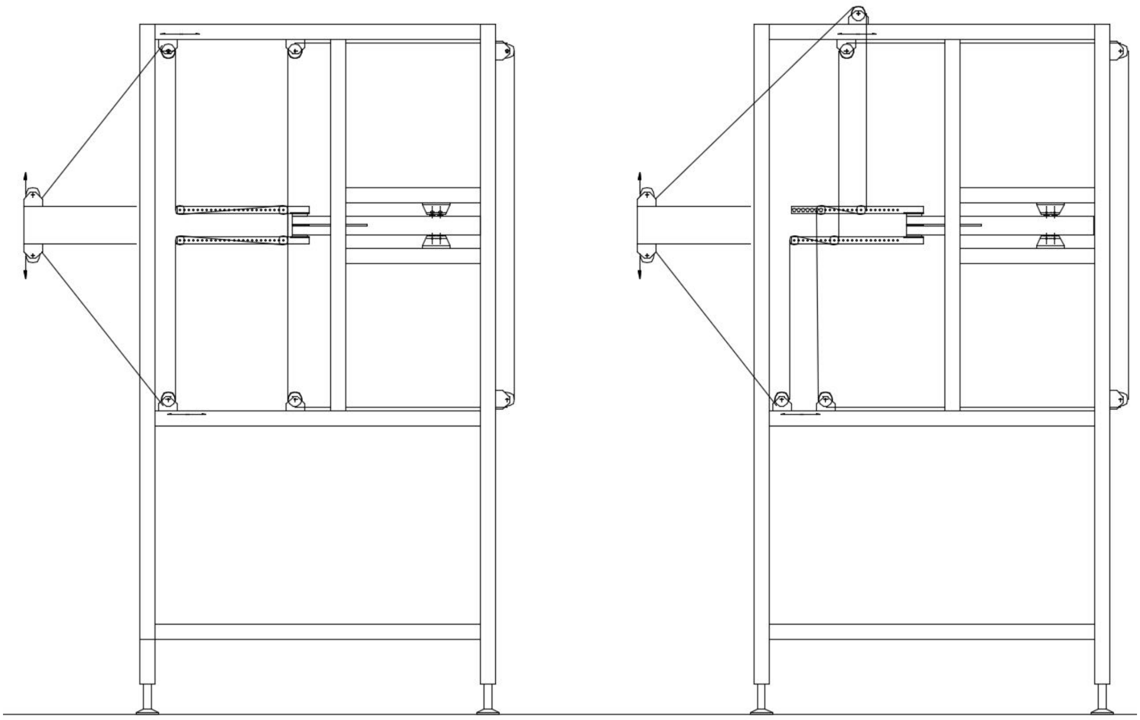

Figure B.15: Concept 5 Mode I and Mode II setup

To validate the assumption that the wire angles will be small under deformation an AutoCad drawing has been made, were the specimen arms are opened 25° under both mode I and mode II loading. This is shown in figure B.16.
This angular rotation of the wires can be minimized even further by making them longer. To minimize the effect of different moment with different angle of the specimen arms, the moment arms can be preset an angle before the test begins. This preset angle, should be the same, but opposite, as the final expected rotational angle when the crack grows at a stable rate.

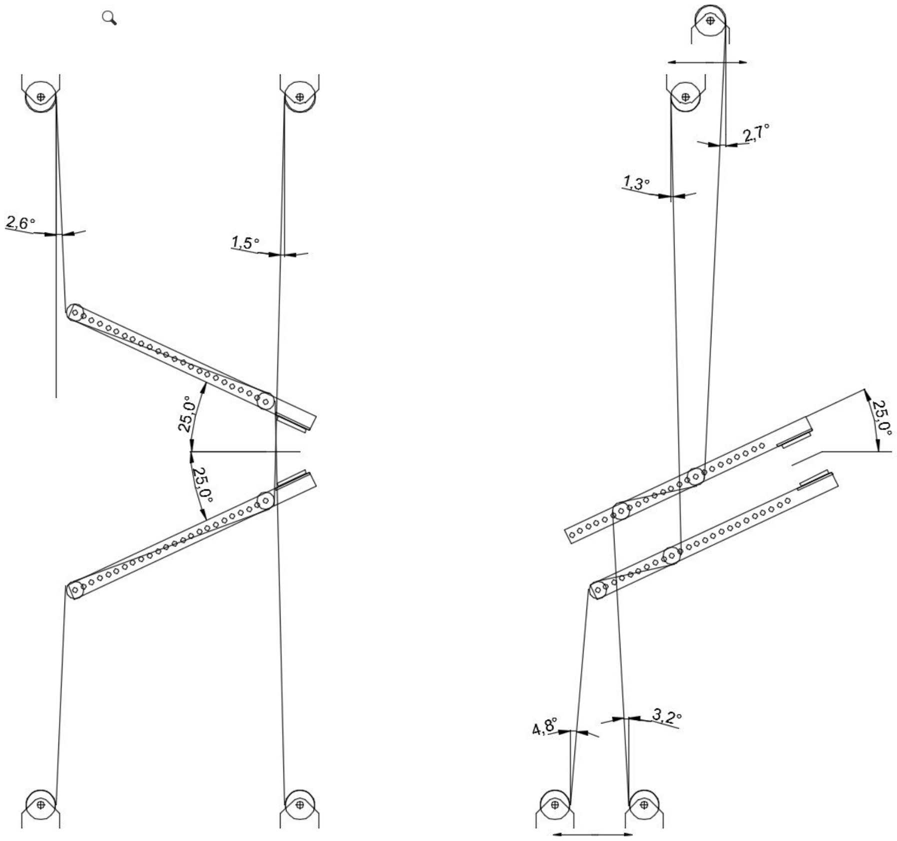


Figure B.16: Sketch of concept 5, showing the deformed state of the moment arms, subjected to pure mode I and mode II respectively

**The advantages of the system are that:**

1. It is easy to change the specimen that is tested as in the previous concept as it builds on the same idea.

2. It can be adapted to a lot of different sizes of specimens.

3. Shorter wire system than seen on the previous test rig by Bent Sørensen.

**The disadvantages of the system are that:**

1. It will still be a large structure which might be difficult to handle.

2. The moment is depending on the angle of the moment arms as described earlier.

3. The system with the wires might cause problems with fatigue.

4. Counterweights might be necessary.

Concept 5, shows a concept that builds upon the idea of using a shorter set of wires, than seen in concept 4. The moment load is introduced to a set of moment arms that are oriented parallel with the DCB specimen. This minimizes the angular rotation of the wires and hence minimizing spurious normal and shear forces. Still problems with controlling the moment is seen, but the effects can be minimized by presetting the moment arms to an angle opposite of the expected rotational angle.

## B.4 Criteria

In order to develop a suitable test tool that can be used for specimens of varying sizes as listed in the introduction, a set of criteria is needed.
Here the different criteria are listed and described. In table B.1 the criteria are given a weight based on their importance. The weights are given from 1-10, where 10 is of highest importance. The importance is a subjective estimation of the influence to the actual project. I.e. costs are not as important as safety. Because if the tool is unsafe to use, costs will not be an issue anymore!

| **Criteria** | **Code** | **Description** | **Weight** |
|---|---|---|---|
| Weight of test tool | C1 | The weight of the test tool is important because it should be able to be moved around by the operator. | 3 |
| Ease of use | C2 | It should be able to be setup by an operator with a minimum of knowledge. | 3 |
| Costs | C3 | The costs of the tool should not be too high. Since this is a master thesis project and not externally financed only a limited amount of money is available. | 8 |
| Safety | C4 | The tool should not make out any risk to the operator. | 8 |
| Size of the test tool | C5 | The size of the test tool matters, because of handling as well as space in the laboratory. | 4 |
| Spurious shear and normal forces | C6 | The introduction of normal and shear forces should be kept at a minimum through the entire test | 7 |
| Stiffness | C7 | The stiffness of the structure is important, because it would otherwise influence the test results. | 6 |
| Fatigue ability | C8 | The ability to perform fatigue analysis is important. It relates to the stiffness of the structure. | 8 |
| Strength | C9 | The strength of the test tool is very important. If it cannot support the testing of the specimens outlined in the introduction, it cannot be used. | 10 |
| Functionality | C10 | A valid estimate is given on the functionality. Will the test tool work? And how difficult will it be to develop it in detail. | 10 |

Table B.1: Criteria for selecting the right concept

### B.4.1 Evaluation of the concepts

In the table below (table B.2), the six concepts are evaluated based on the criteria listed previously in table B.1. Each of the concepts are given a grade from 1-10, were 10 is best. Then the grade is multiplied with the weight of the given criteria. Lastly the product of the grade and weight is summed for each concept. The best concept is the one with the highest score.

| **Criteria/ Concept no.** | **Weight** | **1** | **Sum** | **1.1** | **Sum** | **2** | **Sum** | **3** | **Sum** | **4** | **Sum** | **5** | **Sum** |
|---|---|---|---|---|---|---|---|---|---|---|---|---|---|
| C1 | 3 | 3 | 9 | 1 | 3 | 3 | 9 | 9 | 27 | 6 | 18 | 8 | 24 |
| C2 | 3 | 4 | 12 | 8 | 24 | 3 | 9 | 6 | 18 | 8 | 24 | 8 | 24 |
| C3 | 8 | 4 | 32 | 1 | 8 | 3 | 24 | 8 | 64 | 7 | 56 | 8 | 64 |
| C4 | 9 | 8 | 72 | 8 | 72 | 3 | 27 | 9 | 81 | 7 | 63 | 7 | 63 |
| C5 | 4 | 7 | 28 | 8 | 32 | 6 | 24 | 10 | 40 | 1 | 4 | 6 | 24 |
| C6 | 7 | 4 | 28 | 10 | 70 | 1 | 6 | 1 | 7 | 8 | 56 | 9 | 63 |
| C7 | 6 | 8 | 48 | 9 | 54 | 8 | 48 | 6 | 36 | 7 | 42 | 7 | 42 |
| C8 | 8 | 1 | 8 | 6 | 48 | 1 | 8 | 8 | 64 | 5 | 40 | 6 | 48 |
| C9 | 10 | 8 | 80 | 7 | 70 | 8 | 80 | 9 | 90 | 7 | 70 | 7 | 70 |
| C10 | 10 | 3 | 30 | 8 | 80 | 1 | 10 | 2 | 20 | 8 | 80 | 9 | 90 |
| Sum | - | - | 347 | - | 461 | - | 245 | - | 447 | - | 453 | - | **512** |

Table B.2: Evaluation of concepts

As can be seen, concept 5 has the largest amounts of points. Although concept 1.1 would have scored higher if the cost criteria was not included.

# Appendix C

# The Finite Element Method

## C.1 Introduction

In the next sections, the boundary value problem is shown, and the weak form of the finite element method is presented. Then the derivation of the stiffness matrix based on the principle of virtual work is shown. Followed by an introduction to delamination analysis using the FEM is given. From this the cohesive behavior for mode I and mixed mode is shown and the power law criterion as well as the B-K criterion are presented. This is then followed by a short introduction to nonlinear solution methods and a presentation of the VCCT.

## C.2 Boundary value problem

The finite element method is according to (Lindgaard, 2012) a universal method to solve partial differential equations (PDE) written in "Strong form" but solved in "weak form". In order to be able to this, the PDE's are converted from strong form to weak form, using the principle of stationary total potential energy or virtual work. Since the principle of stationary total potential energy is only valid for elastic continua (Shames and Dym, 2003), the principle of virtual work is used in the following discussion.

For the boundary value problem for a linear elastic isotropic homogenous body, as shown in figure C.1, with a body with domain $\Omega$. It needs to satisfy the strain displacement equations, the equilibrium conditions as well as the constitutive requirements in every point. The derivation of the equations can be found in for instance (Kildegaard, 2013). The 6 equations for the strain displacement relations can in the general sense be written as the non-linear Green-Lagrange tensor (Shames and Dym (2003) p.23):

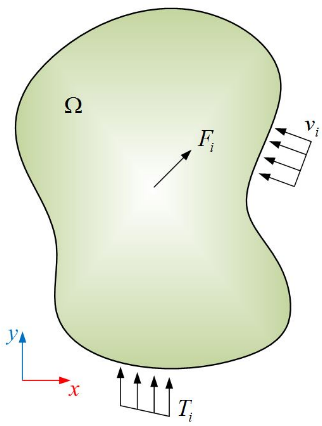


Figure C.1: Domain with boundary $\Omega$, subjected to body forces $F_i$, tractions $T_i$ and boundary conditions $v_i$.

$$\epsilon_{ij} = \frac{1}{2}(v_{i,j} + v_{j,i} + v_{k,i}v_{k,j}) \tag{C.1}$$

Restricting the displacements to being small the product of the differentiated displacements in the above equation $(v_{k,i}v_{k,j})$ could be neglected. But since large displacements might be present, it is left as is.

The static requirements for the 3 equilibrium conditions are given as:

$$\sigma_{ji,j} + F_i = 0 \tag{C.2}$$

Were $F_i$ are the body forces. Finally the constitutive requirements that relate stresses to strains are given as the following 6 equations:

$$\epsilon_{ij} = \frac{1}{E}\{(1+\nu)\sigma_{ij} - \nu\delta_{ij}\sigma_{kk}\} \tag{C.3}$$

Moving from strong form to weak form, the problem shown in figure C.1 is written as a functional that gives the integral expression over the structure as (shown in 2D only) (Cook, 2002):

$$\Pi = \int\int f(x, y, u, v, u_x, u_y, v_x, v_y, ..., v_{yy})dxdy \tag{C.4}$$

This equation represents an integral expression for the functional that is a function of both displacements and strains, where the later is a function of displacements.

## C.3 The principle of virtual work

The principle of virtual work is another alternative to the PDE's which are established on basis of the equilibrium equations. Considering a body subjected to surface and body forces in static equilibrium, all particles of this body is also in equilibrium. This means that this particle subjected to a virtual displacement is fictitious because the virtual forces at the point remains unchanged. Which means that the work done, by these forces are called virtual work. From this it turns out that for a body in equilibrium, the virtual work must be zero. The virtual work done by surface, body forces and concentrated forces are a summation of virtual forces times displacements and are given as (Cook, 2002):

$$\{\delta W\} = \int\limits_{V_e} \{\delta u\}^T \{F\} \, dV + \int\limits_{S_e} \{\delta u\}^T \{\Phi\} \, dS \tag{C.5}$$

Were $\{\Phi\}$ are the surface tractions and $\{F\}$ are the body forces. The virtual work of the internal stresses can be written as:

$$\{\delta W\} = \int\limits_{V_e} \{\delta \epsilon\}^T \{\sigma\} \, dV \tag{C.6}$$

Thereby the weak form of the finite element solution can be written as:

$$\int\limits_{V_e} \{\delta \epsilon\}^T \{\sigma\} \, dV = \int\limits_{V_e} \{\delta u\}^T \{F\} \, dV + \int\limits_{S_e} \{\delta u\}^T \{\Phi\} \, dS + \sum_{i=1}^{n} \{\delta u\}_i^T \{p\}_i \tag{C.7}$$

This equation states that "*for any quasistatic and admissible virtual displacement $\{\delta u\}$ from an equilibrium configuration the increment of strain energy stored is equal to the increment done by body forces $\{F\}$ in volume $V$ and surface tractions $\{\Phi\}$ on surface $S$* " (Cook (2002) p. 88) as well as concentrated forces $\{p\}_i$ (Lindgaard, 2012). In other words the internal work is equal to the work done by the outer forces, when the deformable body is in equilibrium and subjected to a virtual kinematic admissible displacement.

Introducing the interpolated displacement field $\{u\}$ as:

$$\{u\} = [N] \{d\} \tag{C.8}$$

Here $\{d\}$ is the nodal dof, and $[N]$ is the shape functions for the element.

And hence the strains are defined as:

$$\{\epsilon\} = [B]\{d\} \tag{C.9}$$

Where $[B] = [\partial][N]$ is the strain displacement matrix. From equations C.8 and C.9, the virtual displacement and strain can be written as:

$$\{\delta u\}^T = \{\delta d\}^T [N]^T \quad \text{and} \quad \{\delta\epsilon\}^{\mathrm{T}} = \{\delta \mathrm{d}\}^{\mathrm{T}} \{\mathrm{B}\}^{\mathrm{T}} \tag{C.10}$$

From this the discrete version of the virtual work is established for a single element as (Lindgaard, 2012):

$$\underbrace{\{\delta d\}^T \int_{V_e} [B]\{\sigma\}\, dV}_{r^{int}} = \underbrace{\{\delta d\}^T \left( \int_{V_e} [N]^T \{F\}\, dV + \int_{S_e} [N]^T \{\Phi\}\, dS + \sum_{i=1}^{n} \{p\}_i \right)}_{\text{Consistent load vector } \mathrm{r}^{\mathrm{ext}}} \tag{C.11}$$

The above expression is valid for any kinematically admissible virtual displacement of the nodes $\{\delta d\}$. The word consistent stems from the fact that the external load vector is depending on the same shape functions as used to form the stiffness matrix as seen below in eq. C.13. Parts of the integral expression might be 0 in general or for some elements only.

For a single element, the stiffness matrix multiplied with the external consistent nodal load vector can be written as:

$$[k]\{d\} = r^{ext} \tag{C.12}$$

Were $[k]$ is the stiffness matrix for a single element. The derivation of $[k]$ can be found in for instance (Cook, 2002) and is formulated as:

$$[k] = \int_{V_e} [B]^T [E][B]\, dV \tag{C.13}$$

After assembly of the global stiffness matrix $[K]$ the structured governing equation can be solved:

$$[K]\{D\} = \{R\} \tag{C.14}$$

## C.4 Delamination analysis using the FEM

As a method to solve delamination problems using the finite element method two different methods are usually applied. A third method, called the extended finite element method (XFEM) is already implemented in the commercial code Abaqus, and is expected to be implemented in the commercial code Ansys in release 16.0. However this method is outside the scope of this study. The first method, is the popular LEFM approach, were the use of the Virtual Crack Closure Technique (VCCT) has gained great popularity over the recent years. It can be used to calculate the critical energy release rate for existing cracks and can be used to analyze crack propagation when the critical energy release rates for the different modes are known and a preexisting crack is modeled. One of the key benefits is that the VCCT can be used to calculate the critical energy release rate $\mathscr{G}_{Ic}$.

Secondly there is the cohesive damage approach, were a softening relationship between the stresses and displacements is applied. Special elements are employed to characterize the constitutive behavior of the interface surfaces. These elements can either be contact elements which are modeled as bonded or special interface elements. The advantages of the cohesive damage method, is that no pre- crack is needed, and that it is quite easy to change normal contact elements to cohesive contact elements.

For the VCCT, and the cohesive damage method, the use of interface elements can be applied. These elements are based on a traction - constitutive behavior $(\sigma - \delta)$ and are modeled as a layer in between other elements that pre-define the crack growth path through the specimen. I.e. the interface elements join the two parts that are separated during crack growth. Interface elements can have zero or finite thickness.

Contact elements can only be used with the cohesive damage approach. These elements are modeled as zero thickness, and only fully bonded connections are applicable.

### C.4.1 Constitutive behavior for single mode delamination

Here only the bilinear softening model is shown, which is the most used material model to simulate softening behavior of the DCB specimens as the crack opens and propagates. Different methods have been suggested (Davila et al., 2001). The physical behavior of the composite is that, as load increases, no measurable opening is occurring until the normal stress ($\sigma_n$) has reached a value of the critical stress $\sigma_n^c$. Then the crack propagates. But in order to achieve numerical stability, a penalty stiffness $K_p$ is added, which has to simulate the perfect bond of the cohesive interface. Various choice of penalty stiffness has been suggested by different authors (Davila et al., 2001). Davila et al. (2001) suggests to use a value of $10^6 N/mm^3$ for all modes. However according to (Lindgaard, 2012), the value should not be set too high as to avoid numerical instability due to badly conditioned stiffness matrix. A too low value will result in a wrong compliance of the interface and will influence the response of the specimen. (Lindgaard, 2012) suggest use of an expression that relates through thickness stiffness $E_3$ to the penalty stiffness by the use of a factor $\alpha = 50$. This gives epoxy glass laminates approximately the same value as the value suggested by (Davila et al., 2001).

Figure C.2, shows bilinear constitutive behavior of a specimen subjected to pure mode I opening. First at point 0, the specimen is initially unloaded. Then ramping up the stresses to point 1, which is the onset of crack propagation. Followed by decrease in stress to point 3. Here the crack has fully opened and is essentially stress free. During unloading the SERR $\mathscr{G}_I$ is computed from triangle 0-1-2. It could be concluded that when the crack is fully damaged, i.e. at point 3 in figure C.2. The triangle 0-1-3 gives the critical energy release rate $\mathscr{G}_I c$.

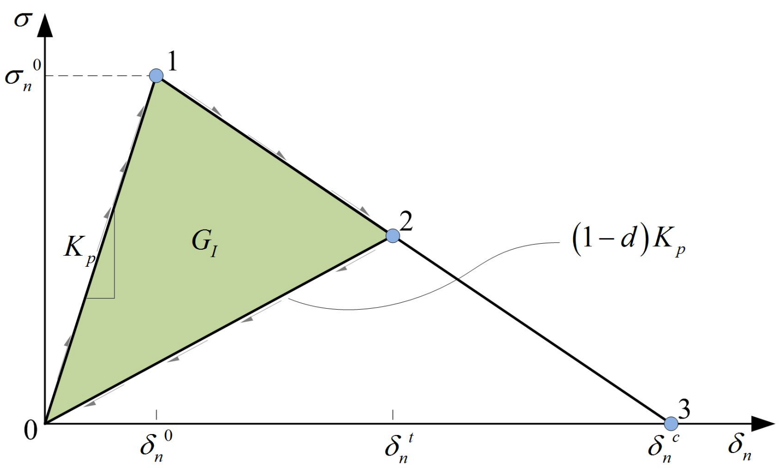


Figure C.2: The bilinear constitutive relationship under mode I loading

Looking at the process between point 0 and 1, it can be described the relation for any single mode as:

$$\sigma_i = K_{pi}\delta_i \tag{C.15}$$

Where index $i$ represents the mode (I, II or III). The equation is valid for the opening of the specimen in the range $\delta_i \leqslant \delta_i^0$. And for the range between $\delta_i^0 < \delta_i < \delta_i^c$ the stress can be written as:

$$\sigma_i = (1 - d_i)K_{pi}\delta_i \tag{C.16}$$

Assembling the above equations, the process can be described for any single mode loading as:

$$\sigma_i = \begin{cases} K_p\delta_i & \text{if} \quad \delta_i^{max} \leqslant \delta_i^0, \\ (1 - d_i)K_{pi}\delta_i & \text{if} \quad \delta_i^0 < \delta_i^{max} < \delta_i^c, \\ 0 & \text{if} \quad \delta_i^{max} > \delta_i^c. \end{cases} \tag{C.17}$$

Where $d_i$ is the accumulated damage in the process, so that $d_i = 0$ initially at $\delta_i^0$ and $d_i = 1$. $\delta_i^{max}$ is used because then the irreversibility is taken into account. Damage variable $d_i$ can be represented as:

$$d_i = \begin{cases} 0 & \text{if} \delta_i^{max} \leqslant \delta_i^0, \\ 1 & \text{if} \delta_i^{max} = \delta_i^c, \end{cases} \tag{C.18}$$

And:

$$d_i = \frac{\delta_i^c(\delta_i^{max} - \delta_i^0)}{\delta_i^{max}(\delta_i^c - \delta_i^0)} \tag{C.19}$$

From the geometrical relations in figure C.2, the critical ERR for the individual mode is found as:

$$\mathscr{G}_{ic} = \frac{\sigma_i^0 \cdot \delta_i^0}{2} \tag{C.20}$$

In order to avoid penetration of the surfaces the following argument is used:

$$\sigma_n = K_p\delta_n \quad \text{if} \quad \delta_n \leqslant 0 \tag{C.21}$$

## C.4.2 Constitutive behavior for mixed mode delamination

For the onset of damage determination, for single mode delamination, stress components can simply be compared with the allowables. For mixed mode delamination, where the different modes (I, II and III) interacts, the onset of damage might occur before any of the stress components reach their allowable values. Different criterion have been proposed by several authors (Davila et al., 2001), (Xu and Needleman, 1994) and (Turon et al., 2006). The derivation here is based on the work done by (Davila et al., 2001) and (Camanho and Davila, 2002).

First assuming that the damage evolution parameter $d_i = d$ is the same for all three modes (Mode I, II, and III) and thereby predicting the onset of damage based on the following criterion:

$$\left(\frac{\langle\delta_I\rangle}{\delta_I^0}\right)^2 \left(\frac{\delta_{II}}{\delta_{II}^0}\right)^2 \left(\frac{\delta_{III}}{\delta_{III}^0}\right)^2 = 1 \tag{C.22}$$

The norm of the displacement jump tensor during opening can be formulated as:

$$\begin{aligned} \delta_m &= \sqrt{\delta_1^2 + \delta_2^2 + \langle\delta_3^2\rangle} \\ &= \sqrt{\delta_{shear}^2 + \langle\delta_3^2\rangle} \end{aligned} \tag{C.23}$$

Here the numbers (1,2 and 3) refers to modes II, III and I respectively according to figure C.3. The angled brackets $\langle\ \rangle$ defines the McCauley operator as: $\langle x\rangle = \frac{1}{2}(x + |x|)$. This ensures that $x$ is always positive. And $\delta_{shear}$ represents the norm of the vector that acc. to Pythagoras defines tangential relative displacement from modes II and III.

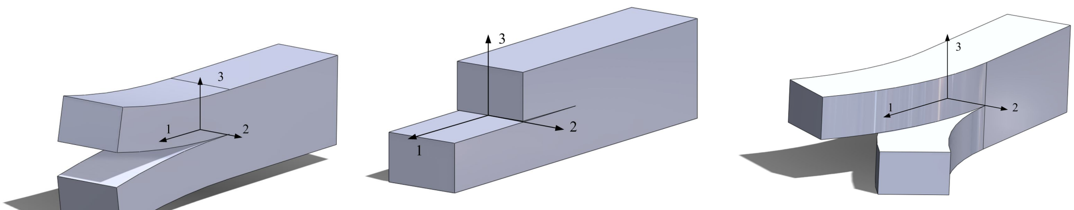


(a) Mode I coordinate system (b) Mode II coordinate system (c) Mode III coordinate system

Figure C.3: Coordinate system for the three opening modes

Formulating mixed mode ratios in terms of the mode components as:

$$\begin{aligned} \beta_{\delta II} = \frac{\delta_{II}}{\delta_I} \quad \text{or} \quad \beta_{\delta III} = \frac{\delta_{III}}{\delta_I} \\ \text{or simply} \quad \beta = \frac{\delta_{shear}}{\delta_I} \end{aligned} \tag{C.24}$$

Onset of damage for mode mixity in terms of the relative opening can be described by combining the above equations:

$$\delta_m^0 = \begin{cases} \delta_3^0\delta_1^0\sqrt{\frac{1+\beta^2}{(\delta_1^0)^2+(\beta\delta_3^0)^2}} & \text{if } \delta_3 > 0, \\ \delta_{shear} & \text{if } \delta_3 \leqslant 0, \end{cases} \tag{C.25}$$

This shows that when the mode mixity $\beta = 0$, for mode I, then $\delta_m^0 = \delta_3^0$ and that for pure shear mode (mode II or III) or modes in between, $\beta \rightarrow \infty$ then $\delta_m^0 = \delta_{shear}^0$.

Now where the prediction of onset is determined from eq. C.25, the propagation criteria must be determined. One of the most used, is the power law criterion, shown for mode I and II only as:

$$\left(\frac{\mathscr{G}_I}{\mathscr{G}_{Ic}}\right)^\alpha + \left(\frac{\mathscr{G}_{II}}{\mathscr{G}_{IIc}}\right)^\alpha = 1 \tag{C.26}$$

For the power law exponent $\alpha$ set to 1, it has been shown to yield good results for some materials . However for most epoxy composites no definite values for $\alpha$ has been found using values $\alpha = 1$ and $\alpha = 2$ (Camanho and Davila, 2002). This curve fit is based on a set of tests ranging from pure mode I to pure mode II. It is created by plotting the SERR as function of the mode mixity $\beta$ and then fitting the results to the power law function.

Another propagation criteria has been proposed by (Benzeggagh and Kenane, 1996). This criteria uses a function of the modes I and II and a parameter $\eta$, which is obtained from mixed mode tests as described above. The criterion for mode I and II is:

$$\mathscr{G}_{Ic} + (\mathscr{G}_{IIc} - \mathscr{G}_{Ic})\left(\frac{\mathscr{G}_{shear}}{\mathscr{G}_I + \mathscr{G}_{shear}}\right)^\eta = \mathscr{G}_c(\beta) \tag{C.27}$$

Using the mode mixity depending parameter (Turon et al., 2006) $B(\beta) = \frac{\mathscr{G}_{shear}}{\mathscr{G}_I + \mathscr{G}_{shear}} = \frac{\beta^2}{1+2\beta^2-2\beta}$ equation C.27 simplifies to:

$$\mathscr{G}_{Ic} + (\mathscr{G}_{IIc} - \mathscr{G}_{Ic})B(\beta)^\eta = \mathscr{G}_c(\beta) \tag{C.28}$$

The B-K criterion can be seen as an interpolation criterion that interpolates the fracture strength between mode I and mode II (Lindgaard, 2012).

Assuming that the critical ERR for the $i^{th}$ mode can be written as:

$$\mathscr{G}_{ci} = \tfrac{1}{2}K_p\delta_i^0\delta_i^c \tag{C.29}$$

Which is taken from the geometrical relations of the entire triangle 0-1-3, seen in figure: C.2. Then combining equations: C.17, C.23, C.28 and C.29 to get the relative opening as a function of mode mixity for complete decohesion:

$$\delta_m^c(\beta) = \begin{cases} \frac{2}{K_p \delta_m^0} \left[ \mathscr{G}_{Ic} + (\mathscr{G}_{IIc} - \mathscr{G}_{Ic}) \left( \frac{\beta^2}{1+\beta^2} \right)^\eta \right] & \text{if } \delta_3 > 0, \\ \sqrt{(\delta_1^c) + (\delta_2^c)} & \text{if } \delta_3 \leqslant 0, \end{cases} \tag{C.30}$$

From eq. C.30, it can clearly be seen that when setting the mode mixity parameter $\beta = 0$, then $\delta_m^c(0) = \frac{2\mathscr{G}_{Ic}}{K_p \delta_3^0}$. This equation leads back to the form of eq. C.29.

Now it is possible to formulate the damage evolution parameter $d$ which is a function of the relative opening $\delta_m$ as (Lindgaard, 2012):

$$d(\delta_m) = \frac{\delta_m^c(\delta_m - \delta_m^0)}{\delta_m(\delta_m^c - \delta_m^0)} \quad d \in [0, 1] \text{ for } \delta_m \in [\delta_m^0, \delta_m^c] \tag{C.31}$$

This damage parameter updates the damage for every substep in the analysis, so that damage will be irreversible. The update procedure is shown as (Lindgaard, 2012):

$$d^{n+1} = min(max(d(\delta_m), d^n), 1) \tag{C.32}$$

This ensures that the damage parameter will never exceed 1, but is always kept at the maximum value. In figure C.4, it is shown how the damage parameter is updated as the opening extends.
Here the mixed mode critical ERR as is indexed as $\mathscr{G}_c$ and it is shown that the critical ERR for the shear modes are expressed as (Camanho and Davila, 2002):

$$\mathscr{G}_{sc} = \mathscr{G}_{IIc} + \mathscr{G}_{IIIc} \tag{C.33}$$

### C.4.3 Constitutive tangent tensor

In figure C.5 the constitutive tangent tensor is introduced, which relates displacements to interface stress for the crack in its respective mode.

The derivation of the tangent stiffness is outside the scope of this study, but is shown in (Turon et al., 2006). The interface stress for a given mode is given as (Turon et al., 2006):

$$\sigma_i = (1-d) D_{ij}^0 \delta_i - d \cdot D_{ij}^0 \overline{\delta_{3i}} \langle -\delta_3 \rangle \quad \text{, where} \quad D_{ij}^0 = \overline{\delta_{ij}} K_p \tag{C.34}$$

Here $\overline{\delta_{ij}}$ represents the *Kronceker delta* and index 3 denotes normal opening. Thereby the undamaged stiffness tensor is written as:

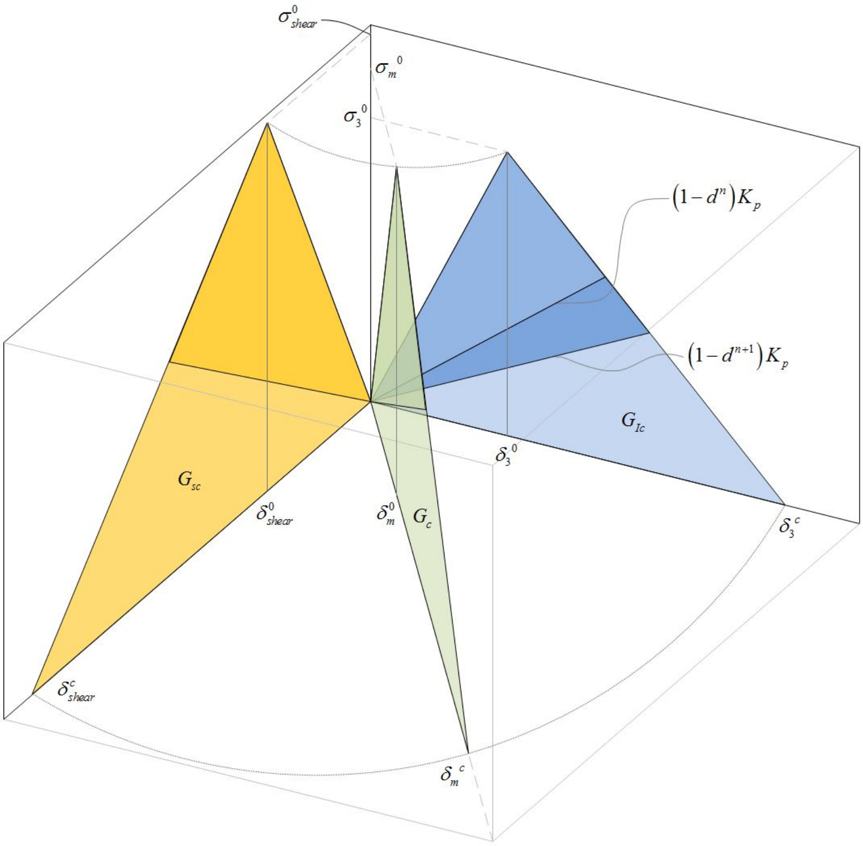


Figure C.4: Illustration of the mixed mode softening law

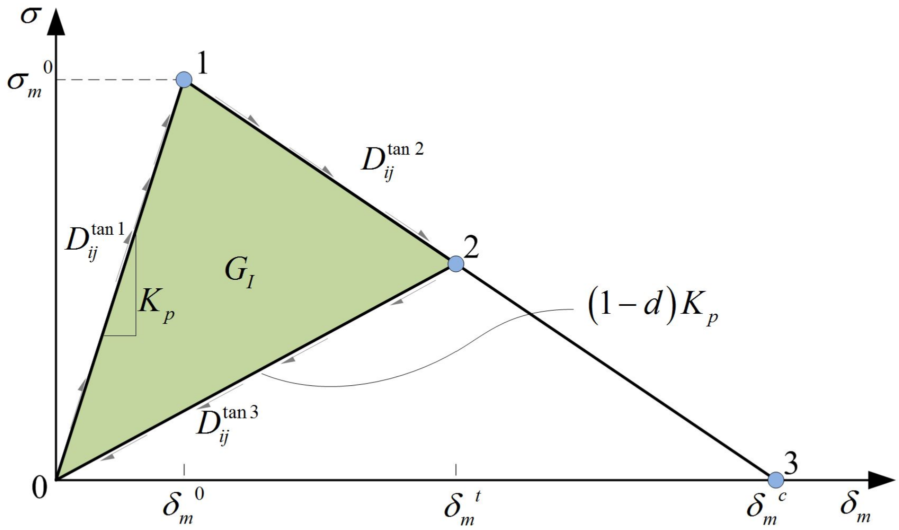


Figure C.5: Tangent stiffness for pure mode displacement

$$D_{ij} = \overline{\delta_{ij}} K_p \left[1 - d\left(1 + \overline{\delta_{3i}} \frac{\langle -\delta_j \rangle}{\delta_j}\right)\right] \tag{C.35}$$

From this the constitutive tangent tensor is obtained as:

$$D_{ij}^{tan} = \begin{cases} D_{ij} & \text{for } \ 0 \leqslant \delta_m < \delta_m^0 \\ D_{ij} - K_p \left(1 + \overline{\delta_{3j}} \frac{\langle -\delta_3 \rangle}{\delta_3}\right) \cdot \left(1 + \overline{\delta_{3i}} \frac{\langle -\delta_3 \rangle}{\delta_3}\right) \cdot L \delta_i \delta_j, & \text{for } \ \delta_m^0 \leqslant \delta_m < \delta_m^c \\ 0 & \text{for } \ \delta_m \geqslant \delta_m^c \end{cases} \tag{C.36}$$

Here $L$ is a scalar value defined as:

$$L = \frac{\delta_m^c \delta_m^0}{\left(\delta_m^c - \delta_m^0\right) \left(\delta_m\right)^3} \tag{C.37}$$

The further implementation can be studied in for instance the Ph.D. thesis by (Turon, 2006).

### C.4.4 Nonlinear solution methods

Nonlinear solutions are typically performed using either the standard Newton-Raphson solver, where the tangent stiffness is updated for every loadstep until convergence. Or the modified Newton-Raphson solver can be used, where the tangent stiffness is kept constant. This can lead to faster convergence even though more iterations are needed in every loadstep. However when displacement jumps occur, limit points or turning point behavior on the load - displacement curve might be observed. This is the case for DCB specimens were the load initially rises, followed by a drop in load. In this case the Arc-length method (ALM) might be used to control the Newton - Raphson method. The ALM incoorperates a method that the solution does not double back on itself during negative slope of the load - displacement curve. For further information refeer to for instance (Cook, 2002).

## C.5 LEFM approach

Because cracks in laminated composites tend to grow along the weak interfaces between the layers, the fracture mechanics approach; Virtual Crack Closure Technique (VCCT) is often used. The VCCT uses the principle outlined by Irwin to calculate the change in strain energy $\Delta U$ which is equal to the work required to close the crack again $W_{closure}$. Furthermore the VCCT uses the following assumptions (Ansys, 2014):

- Crack growth occurs along a predefined crack path

- The hypothesis of self similar crack propagation is used
- The path is defined via interface elements
- The loading can be assumed static or quasi static
- The material is linear elastic and can be isotropic, orthotropic or anisotropic

The crack propagation criterion for the VCCT builds, for instance, for the linear relationship under mode I loading upon that cracks propagate when:

$$\frac{\mathscr{G}_I}{\mathscr{G}_{Ic}} \geqslant 1 \tag{C.38}$$

Other methods are implemented in Ansys APDL release 15, as for instance the power law criterion or the B-K criterion. In figure C.6, the virtual crack closure technique is visualized. The crack grows, so that the initially coincident nodes 2 and 5 are separated. The term stated above, that the crack grows in a self similar way, means that the configuration between nodes 1-2-5-6 is the same as for nodes 2-3-4-5. In other words, this means that the separation between nodes 2 and 5 after crack propagation, will be the same as for nodes 1 and 6 before the crack propagated. This way the work required to close the crack can be formulated for pure mode I as:

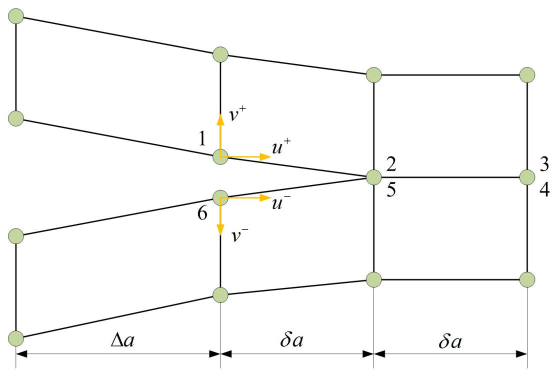


Figure C.6: The virtual crack closure technique (VCCT)

$$\frac{F_{2,5}v_{1,6}}{2\Delta A}\frac{1}{\mathscr{G}_{Ic}} \geqslant 1 \tag{C.39}$$

Here $F_{2,5}$ is the nodal forces that keep the nodes 2 and 5 coincident. $v_{1,6}$ is the separation between nodes 1 and 6, i.e. $v^+ + v^-$ as seen in the figure. $\Delta A = \delta a \cdot t$ where $t$ is the width of the specimen. Similarly it can be formulated for pure mode II and III. For mixed mode criterion the previous described power criterion or the B-K criterion might be applied.

## C.6 Conclusion

In this chapter the relation between the continuum and finite element approach was shown using the principle of virtual work, that allows for elastic continua opposed to the principle of stationary potential energy. The constitutive behavior for mode I is shown using a linear damage variable. Mixed mode is shown, using both the power law criterion as well as the B-K criterion. Furthermore the nonlinear solution methods applied are briefly discussed and it is argued why the use of the Arc - Length method is important. Finally the principle of using the Virtual Crack Closure Technique is shown.

# Appendix D

# Micromechanic aspects of delamination

## D.1 Introduction

In contrast to macro testing of laminates, Sørensen and Jacobsen (1998) presented analytical solutions to the mechanics of fiber bridging using Bernoulli - Euler beam theory and in- situ observations of crack propagation using an environmental scanning electron microscope (ESEM).

First looking at the micro-level crack formation. Crack formation, crack front shape and propagation can be quite different depending on both the resin toughness as well as the loading type, which can be either mode I, II, III or mode mixities in between. (See figure 3.4).
A crack will start as nucleation of microscopic voids or crazing in the matrix material, depending on ductility. These micro voids in turn will grow and coalescence of micro cavities will occur. The continuous growth of the micro cavities will eventually turn into macro cracks and the debonding process will be started. See figure D.1.
When the crack grows, fiber ligaments, will form between the two crack faces. An example of this is shown in figure D.2 for pure mode I loading. The fiber ligaments will have an restrictive influence on the crack from opening.

## D.2 Pure mode I loading

For mode I loading Sørensen and Jacobsen (1998) presented a relation between stress and displacement based on in- situ observations, from ESEM micro-graphs, and Bernoulli - Euler beam theory. Despite neglecting shear deformation and shear

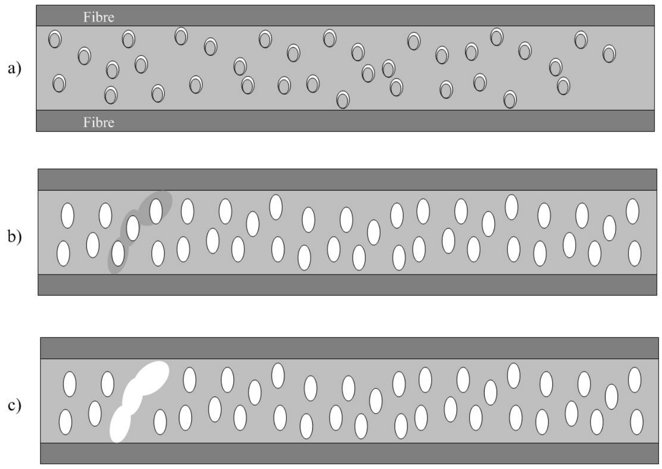


Figure D.1: a) Nucleation of voids in the matrix material, b) Micro cavities and coalescence, c) creation of macro cracks. All for mode I loading

modulus, eq. D.1 was proven to be quite close to the model presented by (Spearing and Evans, 1992) which included the shear modulus. The traction - displacement relationship is given:

$$\sigma_n(\delta_n) = \left(\frac{2}{3}\right)^{3/4} \cdot \eta \frac{\mathscr{G}_c^{3/4} E^{1/4} t}{\sqrt{\delta_n}} \tag{D.1}$$

Here $\mathscr{G}_c$ is the energy release rate for the ligament, $t$ is the height of the ligaments, $E$ is the modulus of elasticity, and $\eta$ is the number of ligaments per crack surface area. Thus the stress - displacement relationship curve, which can be seen in figure D.3 is described using the material values defined in table D.1. The nominator in eq. D.1 can be expressed as $\lambda$. Hence the equation becomes:

$$\sigma_n(\delta_n) = \frac{\lambda}{\delta^{1/2}} \tag{D.2}$$

$\lambda$ can be found experimentally as (Sørensen and Jacobsen, 1998):

$$\lambda = \frac{\Delta J_{ss}}{2\sqrt{\delta^0}} \tag{D.3}$$

Here $\Delta J_{ss}$ is the difference between the crack tip fracture energy and the steady state energy release rate, i.e. $(J_{ss} - J_0)$. The shape of the traction - displacement curve is quite similar to macro-scale traction - displacement curves, which proves the validity of the model.

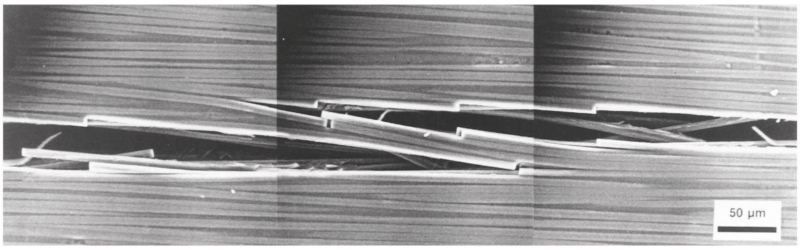


Figure D.2: ESEM micrograph showing beam-like bridging of fibre bundles and single fibres. The crack tip is outside the picture to the right-hand side (Sørensen and Jacobsen, 1998)

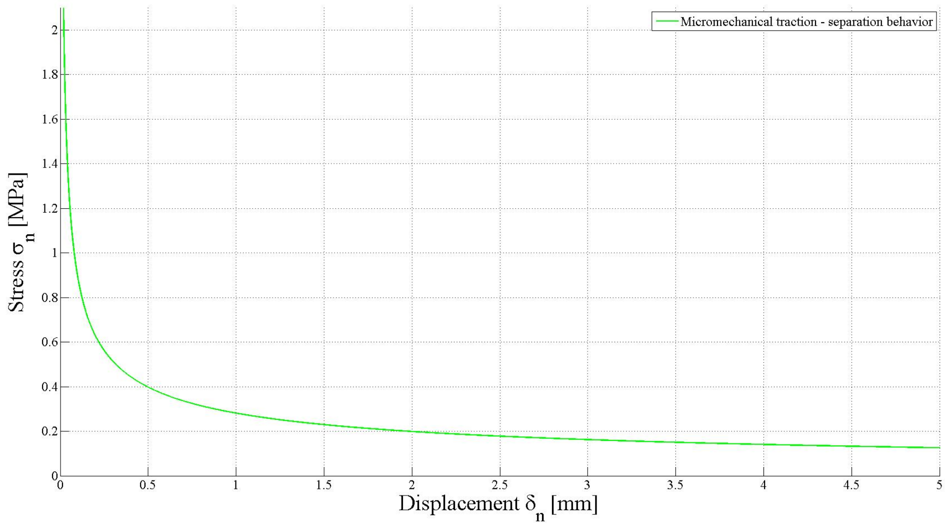


Figure D.3: Micro-mechanical behavior of traction separation behavior

| $2t$ [$\mu$m] | $E$ [GPa] | $\mathscr{G}_c$ [Jm$^{-2}$] | $\eta$ |
|---|---|---|---|
| 50 | 140 | 20 | 12 |

Table D.1: Ligament parameters (Sørensen and Jacobsen, 1998)

## D.3 Mode mixity loading

For mode mixity, the relation between stress and displacement is not trivial since the normal and tangential stresses depend on both normal and tangential opening. Here the mechanisms involved for mode mixity was observed to be the same as for mode I (Sørensen et al., 2008). However one complication was observed, which was that the ligaments in compression acts different than in tension. Namely under compression they buckle. This however was disregarded due to the low strength under buckling. The normal stress as function of the openings is described as:

$$\frac{\sigma_n}{\eta bhE} = \frac{\frac{\delta_n}{h}\left[\frac{\mathscr{G}_c}{Eh}\right]^{3/2}}{\left[\left(\frac{\delta_t}{2h}\right)^2 + \sqrt{\left(\frac{\delta_t}{2h}\right)^4 + 6\frac{\mathscr{G}_c}{Eh}\left(\frac{\delta_n}{2h}\right)^2}\right]^{3/2}} \tag{D.4}$$

And shear stress as:

$$\frac{\sigma_t}{\eta bhE} = \frac{\frac{\delta_t}{h}\left[\frac{\mathscr{G}_c}{Eh}\right]^{1/2}}{\left[\left(\frac{\delta_t}{2h}\right)^2 + \sqrt{\left(\frac{\delta_t}{2h}\right)^4 + 6\frac{\mathscr{G}_c}{Eh}\left(\frac{\delta_n}{2h}\right)^2}\right]^{1/2}} \tag{D.5}$$

Equation D.4 was shown to yield a similar result to equation D.1 if $\delta_t = 0$ thus reduces to:

$$\sigma_n = \frac{1}{4}\left[\frac{8}{3}\frac{\mathscr{G}_c}{Eh}\right]^{3/4}\sqrt{\frac{2h}{\delta_n}\eta bhE} \quad \wedge \quad \delta_t = 0 \tag{D.6}$$

A similar expression can be shown for eq. D.5 if $\delta_n = 0$. Plots of the normal and shear stresses as function of normal and tangential opening can be seen in figures D.4 and D.5.

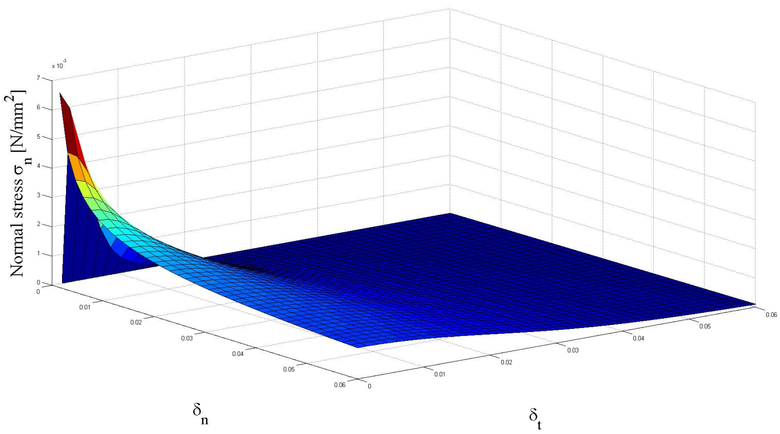


Figure D.4: Normal stress as function of opening

From figure D.4, it can be seen that when the tangential openings occur under mode mixity, the normal stress quickly declines. In contrast in figure D.5, it is seen that the tangential stresses rise quickly when tangential opening modes are present. This can be assumed to be due to fiber fracture in pure tension for mode II, which requires more energy than the peel of effect and fiber bending, that is happening under mode I loading.

From this it can clearly be concluded that the two modes (I and II) cannot be separated during mode mixity.

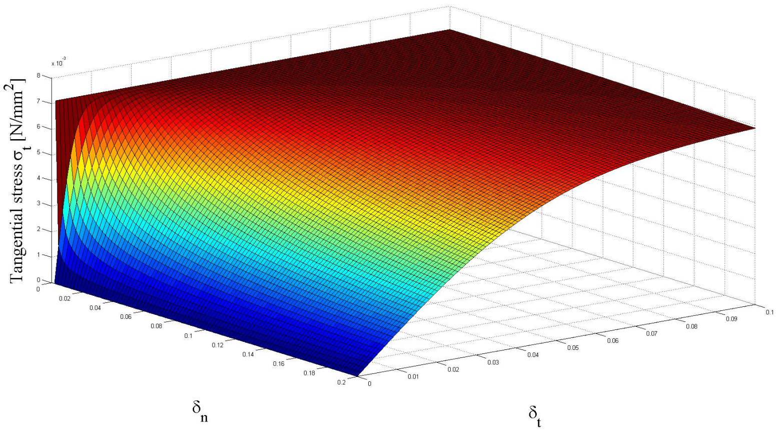


Figure D.5: Tangential stress as function of opening

## D.4 Conclusion

In the above, a short introduction to micro - mechanics aspects for fiber bridging were given. Followed by the presentation of the analytic approach, based on the works by Sørensen and Jacobsen (1998), for the stresses in the cohesive zone as function of mode I and mode mixity.

# Appendix E

# Calculation documentation

| Text: | Calculations: | Input / Results: | Ref. / Comments: |
| --- | --- | --- | --- |

The following calculation documentation, has the purpose to verify the structural strength and capabilities of the test rig.

The documentation is divided into the following parts.
1. List of all loads, dimensions, material constants etc.
2. Static analysis of the moment arms
3. Fatigue analysis of the moment arms
4. Static analysis of the frame
5. Eigen frequency analysis of the frame
6. Static analysis of the wire rollers
7. Static analysis of the roller support structure

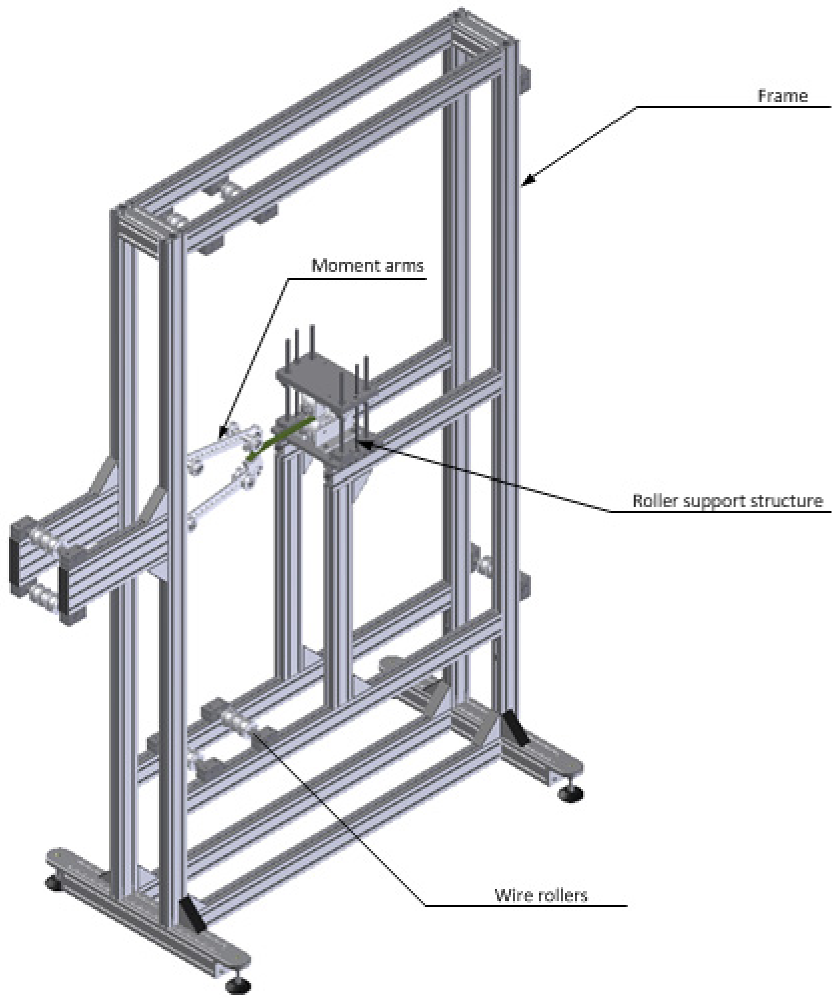

# 1. List of all loads, dimensions, material constants etc.

**Materials:**

Aluminum

| | | | |
|---|---|---|---|
| Density: | | $\rho_{alu} := 2700 \frac{kg}{m^2}$ | |
| Yield stress: | EN AW 6082 - T6 | $R_{p02.6082} := 290MPa$ | From Alumeco.dk |
| | EN AW 2011 Drawn | $R_{p02.2011} := 270MPa$ | |
| | EN AW 2014 T6 | $R_{p02.2014} := 420MPa$ | |
| Fracture strength: | EN AW 6082 - T6 | $R_{m.6082} := 340MPa$ | From Alumeco.dk |
| | EN AW 2011 Drawn | $R_{m.2011} := 370MPa$ | |
| | EN AW 2014 T6 | $R_{m.2014} := 455MPa$ | |
| Young's modulus: | | $E_{alu} := 71 \cdot 10^3 MPa$ | |

Stainless steel

| | | | |
|---|---|---|---|
| Density: | | $\rho_{ss} := 7850 \frac{kg}{m^3}$ | |
| Yield strength | EN 1.4305 | $R_{p02.1.4305} := 490MPa$ | From Matweb.com |
| Fracture strength | EN 1.4305 | $R_{m.1.4305} := 600MPa$ | |
| Young's modulus: | | $E_{ss} := 190 \cdot 10^3 MPa$ | |

Steel

Density: $\rho_{st} := 7850 \frac{kg}{m^3}$

Yield strength C45 $f_y := 490MPa$ From Mechanical and Metal trade Handbook

Fracture strength C45 $f_u := 700MPa$

Yield strength Bolt pin 12.9 $f_{y.b} := 1080MPa$ From Mechanical and Metal trade Handbook

Fracture strength Bolt pin 12.9 $f_{u.b} := 1200MPa$

Young's modulus: $E_{st} := 210 \cdot 10^3 MPa$

**Fatigue strength data for the materials:**

Uncorrected end. limit alu. 6082 T6 $S_{e.6082} := 0.4 \cdot R_{m.6082}$ $S_{e.6082} = 136 \cdot MPa$ According to Machine Design 4th ed.

Hardening exponent - aluminum: $b := -0.115$ Metal fatigue in engineering. Tb. A2

Fatigue strength coefficient: $\sigma_{f'} := 826MPa$ Metal fatigue in engineering. Tb. A2

Basquin formula for EN AW 6082 T6: $S_A(N_{f\_a}) := \sigma_{f'} \cdot (2N_{f\_a})^b$ $S_A(10^8) = 91.7 \cdot MPa$ For R = 0, i.e. pulsating tension, this is the allowable stress range.

| | | | |
|---|---|---|---|
| Uncorrected end. limit C45 steel | $S_{e.C45} := 0.5 \cdot f_u$ | $S_{e.C45} = 350 \cdot MPa$ | |
| Low fatigue limit: | $S_{m.C45} := 0.75 \cdot f_u$ | $S_{m.C45} = 525 \cdot MPa$ | |
| Factor: | | $z := -3$ | Norton Machine design Tb. 6.5 |
| Hardening exponent steel: | $b := \frac{1}{z} \cdot \log\left(\frac{S_{m.C45}}{S_{e.C45}}\right)$ | $b = -0.0587$ | Dividing with MPa, to have consistent units! |
| Fatigue strength coefficient: | $a := \frac{S_{m.C45}}{\left(10^3\right)^b}$ | $a = 787.5 \cdot MPa$ | Metal fatigue in engineering. Tb. A2 |
| Basquin formula for C45 Steel: | $S_S\left(N_{f\_a}\right) := \left\lvert \begin{array}{l} \text{return } a \cdot \left(N_{f\_a}\right)^b \text{ if } N_{f\_a} \le 10^6 \\ S_{e.C45} \text{ otherwise} \end{array} \right.$ | $S_S\left(10^6\right) = 350 \cdot MPa$ | For R = 0, i.e. pulsating tension, this is the allowable stress range. |

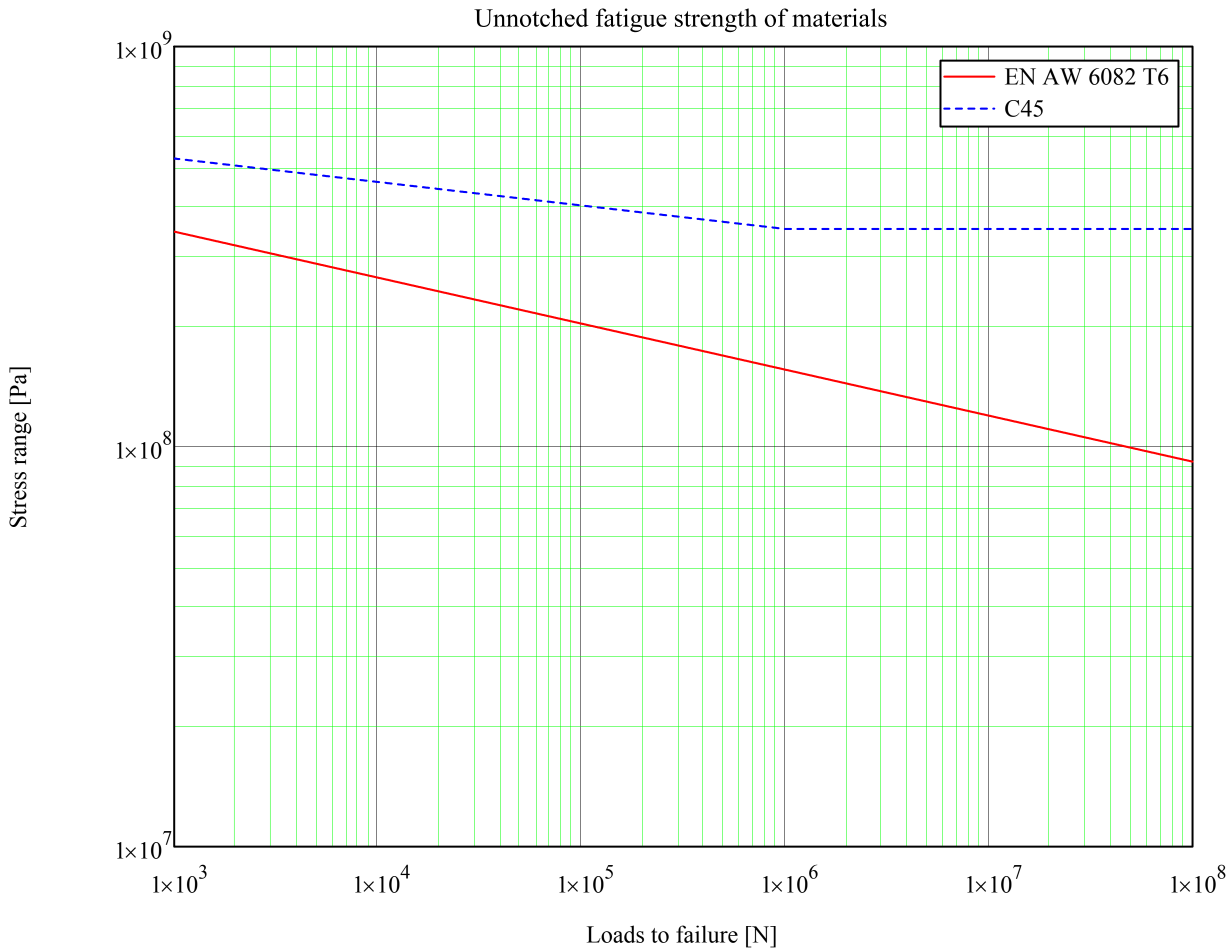
Unnotched fatigue strength of materials
EN AW 6082 T6
C45
Stress range [Pa]
1×10^9
1×10^8
1×10^7
1×10^3
1×10^4
1×10^5
1×10^6
1×10^7
1×10^8
Loads to failure [N]

**Pure Mode I loads**
The calculated forces are based on mode I opening, with the critical energy release rate set to:

| | | |
|---|---|---|
| Critical ERR: | $G_{I.c} := 500 \frac{J}{m^2}$ | This is the basis for mode I loading. |
| Maximum moment for the smaller specimens. | $M_{I.s} := 50 N \cdot m$ | This mode I load covers specimen sizes up to a dimension 2H = 30 mm and t = 25 mm |
| Maximum moment for the larger specimens. | $M_{I.L} := 147 N \cdot m$ | The mode I load is based on a maximum cross section dimension of 2H = 50 mm and t = 30 mm |

**Pure Mode II loads**
The calculated forces are based on mode II opening, with the critical energy release rate set to:

| | | |
|---|---|---|
| Critical ERR: | $G_{II.c} := 3000 \frac{J}{m^2}$ | This is the basis for mode II loading |
| Maximum moment for the smaller specimens. | $M_{II.s} := 160 N \cdot m$ | The mode II load is based on a maximum cross section dimension of 2H = 30 mm and t = 25 mm |
| Maximum moment for the larger specimens. | $M_{II.L} := 420 N \cdot m$ | The mode II load is based on a maximum cross section dimension of 2H = 50 mm and t = 30 mm |

## 2. Static analysis of the moment arms

As outlined in the main report, two types of moment arms have been designed. The smaller ones can be used with DCB specimen beam height up to 15 mm, i.e. total height of 30 mm. And a width of 25 mm. The larger moment arms are designed to test specimens up to a total cross section of 2H = 50 mm, and width t = 30 mm. This is under the assumption of the critical ERR stated.

First the **smaller moment arms** are verfied:

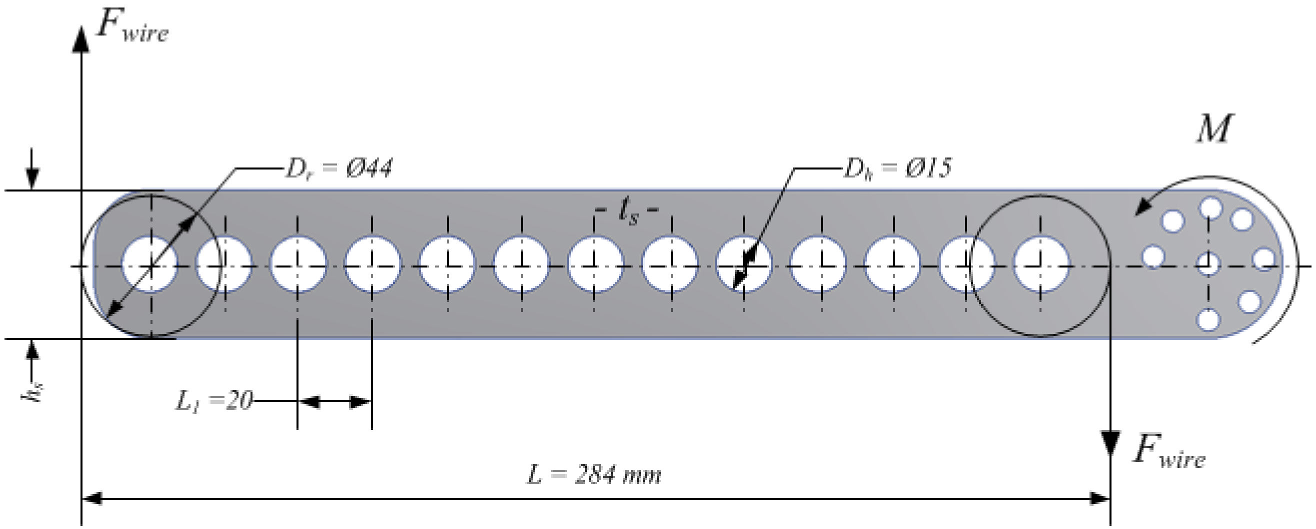


Maximum length between input loads: $L := 284mm$ Maximum length is taken, because it will be used with the largest specimens.

Diameter of rollers: $D_r := 44mm$

Diameter of holes: $D_h := 15mm$

Length between holes: $L_1 := 20mm$

Thickness of small moment arm: $t_s := 8mm$

Heigth of moment arm: $h_s := 40mm$

*If the rollers are set to the maximum distance i.e.*

Force in the wires for small specimens: $F_{wire.1.s} := \frac{M_{II.s}}{L}$ $F_{wire.1.s} = 563.4\,N$

Please note, that this force is divided into two rollers. One on each side of the moment arm.

Force in the wires for large specimens: $F_{wire.1.L} := \frac{M_{II.L}}{L}$ $F_{wire.1.L} = 1478.9\,N$

*If the rollers are set to the minimum distance i.e.*

Minimum distance: $d_{min} := D_r + 2 \cdot L_1$ $d_{min} = 84 \cdot mm$

Force in the wires for small specimens: $F_{wire.2.s} := \frac{M_{II.s}}{d_{min}}$ $F_{wire.2.s} = 1905\,N$

Please note, that this force is divided into two rollers. One on each side of the moment arm.

Force in the wires for large specimens: $F_{wire.2.L} := \frac{M_{II.L}}{d_{min}}$ $F_{wire.2.L} = 5000\,N$

Pin diameter - small moment arm: $D_{ps} := 8mm$

Circular hole diameter small moment arm: $D_{cs} := 30mm$

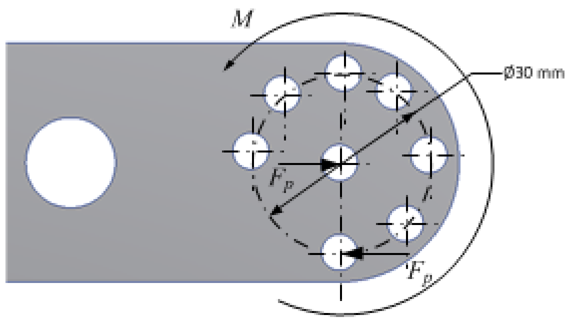


Force acting on each pin: $F_p := \frac{2M_{II.s}}{D_{cs}}$ $F_p = 10.7 \cdot kN$

Shear force in the pin: $F_v := \frac{F_p}{2}$ $F_v = 5.3 \cdot kN$

Pin area: $A_p := \frac{\pi}{4} \cdot D_{ps}^{\ 2}$ $A_p = 50.3 \cdot mm^2$

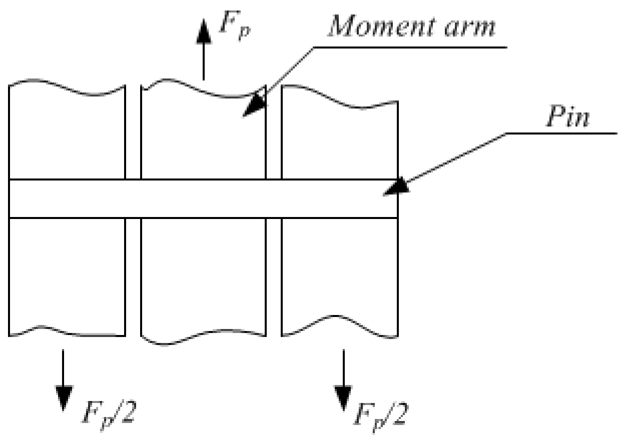


Shear stress in pin: $\tau_p := \frac{4F_v}{3 \cdot A_p}$ $\tau_p = 141.5 \cdot MPa$ Gere and Goodno, 8th SI ed. p. 462

Equivalent stress: $\sigma_{eq.p} := \sqrt{3 \cdot \tau_p^{\ 2}}$ $\sigma_{eq.p} = 245 \cdot MPa$

Shear stress in moment arm: $\tau_{ma} := \frac{F_p}{t_s \cdot D_{ps}}$ $\tau_{ma} = 166.7 \cdot MPa$

Equivalent stress: $\sigma_{eq.ma} := \sqrt{3 \cdot \tau_{ma}^{\ 2}}$ $\sigma_{eq.ma} = 288.7 \cdot MPa$

Utilization of pin bolt: $U_{pin} := \frac{\sigma_{eq.p}}{f_{y.b}}$ $U_{pin} = 22.7 \cdot \%$ The utilization is wrt. the yield strength of the bolt and moment arm material!

Utilization of moment arm: $U_{ma} := \frac{\sigma_{eq.ma}}{R_{p02.6082}}$ $U_{ma} = 99.5 \cdot \%$

Now the **larger moment arms** are verified:

Generally the dimensions are not changed except the ones listed below.

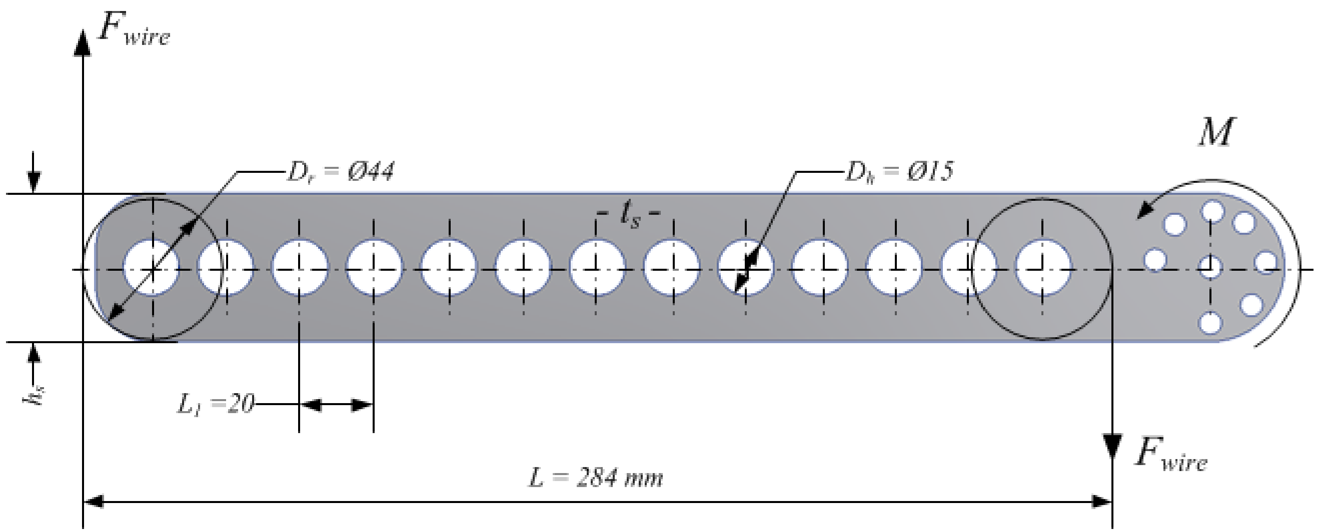


Thickness of large moment arm: $t_L := 15mm$

Heigth of moment arm: $h_L := 50mm$

Pin diameter - large moment arm: $D_{pl} := 10mm$

Circular hole diameter large moment arm: $D_{cL} := 35mm$

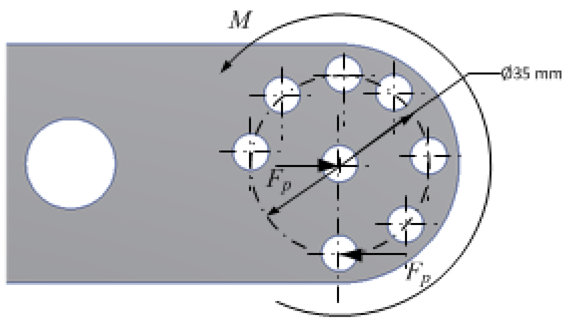


Force acting on each pin: $F_p := \frac{2M_{II.L}}{D_{cL}}$ $\qquad F_p = 24 \cdot kN$

Shear force in the pin: $F_v := \frac{F_p}{2}$ $\quad F_v = 12 \cdot kN$

Pin area: $A_p := \frac{\pi}{4} \cdot D_{pl}^2$ $\quad A_p = 78.5 \cdot mm^2$

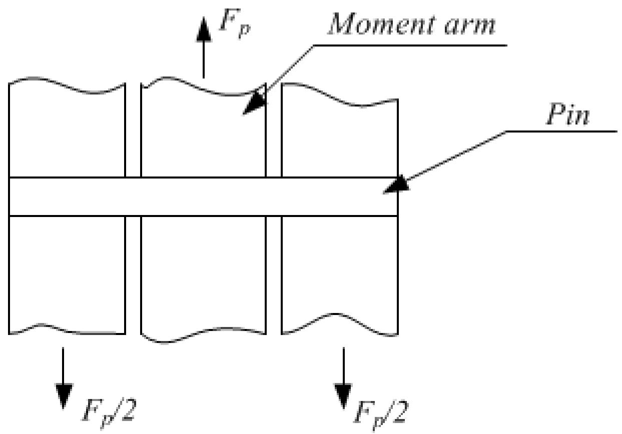


Shear stress in pin: $\tau_p := \frac{4F_v}{3 \cdot A_p}$ $\quad \tau_p = 203.7 \cdot MPa$ $\quad$ Gere and Goodno, 8th SI ed. p. 462

Equivalent stress: $\sigma_{eq.p} := \sqrt{3 \cdot \tau_p^2}$ $\quad \sigma_{eq.p} = 352.9 \cdot MPa$

Shear stress in moment arm: $\tau_{ma} := \frac{F_p}{t_L \cdot D_{pl}}$ $\quad \tau_{ma} = 160 \cdot MPa$

Equivalent stress: $\sigma_{eq.ma} := \sqrt{3 \cdot \tau_{ma}^2}$ $\quad \sigma_{eq.ma} = 277.1 \cdot MPa$

Utilization of pin bolt: $U_{pin} := \frac{\sigma_{eq.p}}{f_{y.b}}$ $\quad U_{pin} = 32.7 \cdot \%$ $\quad$ The utilization is wrt. the yield strength of the bolt and moment arm material!

Utilization of moment arm: $U_{ma} := \frac{\sigma_{eq.ma}}{R_{p02.6082}}$ $\quad U_{ma} = 95.6 \cdot \%$

The entire wire load is divided into two rollers. I.e. the load will create a moment on the roller shaft. This moment loading is symmetric in its sense, and no rotations of the shaft will take place inside the moment arm as can be seen in the FBD.

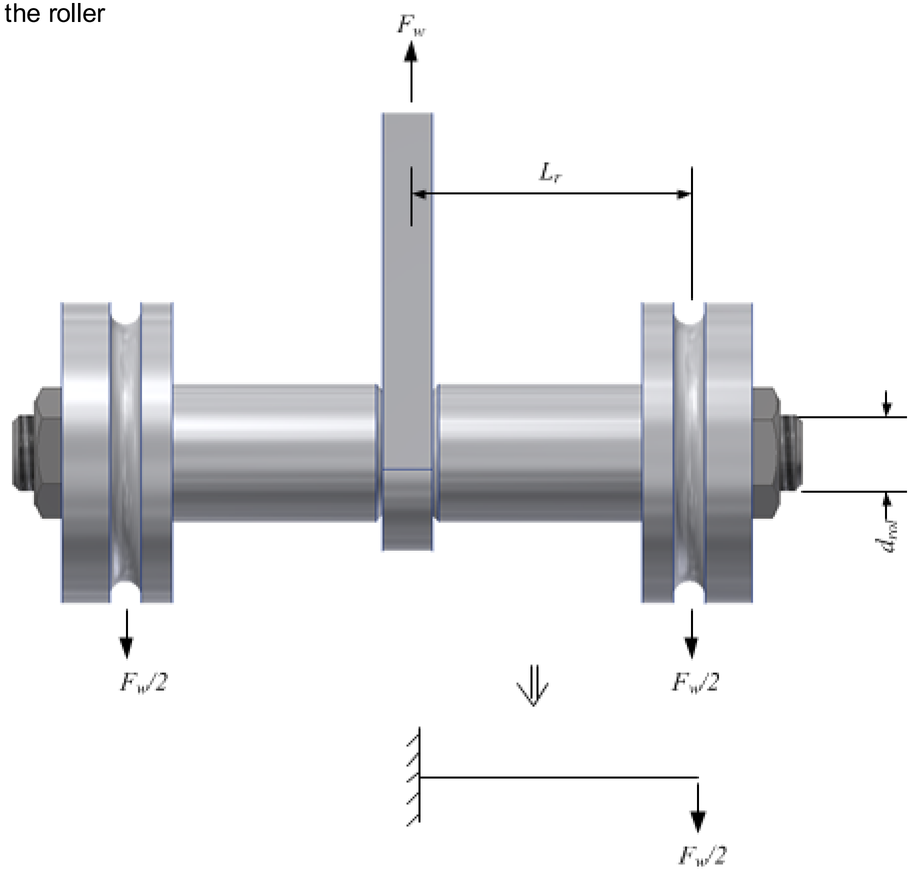


Half length of the entire shaft: $L_r := 40mm$

Diameter of the shaft: $d_{rol} := 15mm$

Moment of inertia shaft: $I_{rol} := \frac{\pi}{64} \cdot d_{rol}^4$ $I_{rol} = 2.5 \times 10^3 \cdot mm^4$

Moment applied to the shaft: $M_{rol} := \frac{F_{wire.2.L}}{2} \cdot L_r$ $M_{rol} = 100 \cdot N \cdot m$ The largest wire force is taken.

Maximum normal stress due to bending: $\sigma_{n.rol} := \frac{M_{rol} \cdot d_{rol}}{2 \cdot I_{rol}}$ $\sigma_{n.rol} = 301.8 \cdot MPa$

Utilization of shaft material: $U_{rol} := \frac{\sigma_{n.rol}}{f_y}$ $U_{rol} = 61.6 \cdot \%$ The utilization is wrt. the yield strength of the shaft material!

Cross section static analysis of the small moment arms:

The cross section effective area: $A_{s.ma} := \left(h_s - D_h\right) \cdot t_s$ $A_{s.ma} = 200 \cdot mm^2$

Moment of inertia: $I_{s.ma.1} := \frac{1}{12} \cdot \left(\frac{h_s - D_h}{2}\right)^3 \cdot t_s + \frac{A_{s.ma}}{2} \cdot \left(\frac{h_s + D_h}{4}\right)^2$ $I_{s.ma.1} = 20.2 \times 10^3 \cdot mm^4$

Maximum normal stress, from bending moment: $\sigma_{s.n.ma} := \frac{M_{II.s} \cdot h_s}{2 \cdot I_{s.ma.1}}$ $\sigma_{s.n.ma} = 158.4 \cdot MPa$

Utilization of yield stress: $U_{s.ma.1} := \frac{\sigma_{s.n.ma}}{R_{p02.6082}}$ $U_{s.ma.1} = 54.6 \cdot \%$

Maximum shear stress is calculated between the holes:

First section modulus: $Q := \frac{A_{s.ma}}{2} \cdot \frac{h_s}{2}$ $\quad Q = 2 \times 10^3 \cdot mm^3$

Moment of inertia, without the hole: $I_{s.ma.2} := \frac{h_s^{\,3} \cdot t_s}{12}$ $\quad I_{s.ma.2} = 42.7 \times 10^3 \cdot mm^4$

Maximum shear stress: $\tau_{s.ma} := \frac{F_{wire.1.s} \cdot Q}{I_{s.ma.2} \cdot t_s}$ $\quad \tau_{s.ma} = 3.3 \cdot MPa$

Utilization of yield stress: $U_{s.ma.2} := \frac{\sqrt{3} \cdot \tau_{s.ma}}{R_{p02.6082}}$ $\quad U_{s.ma.2} = 2 \cdot \%$

Cross section static analysis of the large moment arms:

The cross section effective area: $A_{L.ma} := \left(h_L - D_h\right) \cdot t_L$ $\quad A_{L.ma} = 525 \cdot mm^2$

Moment of inertia: $I_{L.ma.1} := \frac{1}{12} \cdot \left(\frac{h_L - D_h}{2}\right)^3 \cdot t_L + \frac{A_{L.ma}}{2} \cdot \left(\frac{h_L + D_h}{4}\right)^2$ $\quad I_{L.ma.1} = 76 \times 10^3 \cdot mm^4$

Maximum normal stress, from bending moment: $\sigma_{L.n.ma} := \frac{M_{II.L} \cdot h_L}{2 \cdot I_{L.ma.1}}$ $\quad \sigma_{s.n.ma} = 158.4 \cdot MPa$

Utilization of yield stress: $U_{L.ma.1} := \frac{\sigma_{L.n.ma}}{R_{p02.6082}}$ $\quad U_{L.ma.1} = 47.6 \cdot \%$

Maximum shear stress is calculated between the holes:

First section modulus: $Q := \frac{A_{L.ma}}{2} \cdot \frac{h_L}{2}$ $\qquad Q = 6.6 \times 10^3 \cdot mm^3$

Moment of inertia, without the hole: $I_{L.ma.2} := \frac{h_L^{\,3} \cdot t_L}{12}$ $\qquad I_{L.ma.2} = 156.3 \times 10^3 \cdot mm^4$

Maximum shear stress: $\tau_{L.ma} := \frac{F_{wire.1.L} \cdot Q}{I_{L.ma.2} \cdot t_s}$ $\qquad \tau_{L.ma} = 7.8 \cdot MPa$

Utilization of yield stress: $U_{L.ma.2} := \frac{\sqrt{3} \cdot \tau_{L.ma}}{R_{p02.6082}}$ $\qquad U_{L.ma.2} = 4.6 \cdot \%$

## 3. Fatigue analysis of the moment arms

Since the test tool will be used for fatigue calculation as well as static analysis, the maximum moment load is found based on the Basquin curve, shown in section 1, of this appendix.

Supposing that the moment arms, will experience up to $10^8$ load cycles in their lifetime, the unnothed fatigue strength of the aluminum parts are:

Unnothed fatigue strength range aluminum: $S_A\left(10^8\right) = 91.7 \cdot MPa$

Unnothed fatigue strength range C45 steel: $S_S\left(10^8\right) = 350 \cdot MPa$

Since the highest loaded part is where the pin bolts are located in the moment arms, and the aluminum has the highest utilization ratio, this is where we attend our focus! The fatigue strength should normally be reduced using factors as f. instance using the procedure according to Norton Machine design. However, in this case the purpose is to find the load that the moment arm can withstand under the optimum conditions i.e without any factors taking into account notches, surface finish ets.

The load is pulsating tension, i.e. the static stress range will be equal to the dynamic stress range! Using iteration, we find that the maximum moment that can be input for mode I and mode II loading, using a Haigh diagram to account for positive mean stress (Not shown here):

Maximum allowable moment for Mode I and II loading: $M_{I.max\_f} := 50N \cdot m$

The corresponding eq. stress is calculated as: $\sigma_{eq} := 90MPa$

This load corresponds to cross section dimensions ***for mode I loading of 2H = 28 mm and t = 25 mm.*** For ***mode II; 2H = 12 mm and t = 25mm:***

These dimensions should of course be smaller than this, depending on the actual stress concentration and surface roughness in this area. But the dimensions can be used as a guideline for designing experiments. Remeber to correct for the energy release rates.

## 4. Static analysis of the frame structure

The analysis of the frame is difficult to perform using an analytic approach. Therefore, it is analyzed using a beam element model in the commercial FEM application - Ansys APDL.

Beam elements used: Beam188

No. of elements: 508

No. of nodes: 933

A cubic interpolation of the shape functions are used to capture all natural frequency modes. I.e. 4 nodes per element are used. KEYOPT(3)=3

The dimensions are taken from the specific drawing 01-01 - Rev. B, that can be found on the accompanying DVD.

The density used for the aluminum profiles and steel shafts are listed in the begining of this appendix.

The following cross section data is used for the profiles:

ITEM8 - 80 x 40 mm

$$I_{y8040} := 1026914 \cdot mm^4$$

$$I_{z8040} := 273767mm^4$$

ITEM8 - 80 x 80 mm

$$I_{y8080} := 1899749 \cdot mm^4$$

$$I_{z8080} := 1899749mm^4$$

ITEM8 - 160 x 40 mm

$$I_{y1640} := 7471891 \cdot mm^4$$

$$I_{z1640} := 535793mm^4$$

Since it is not possible to input the shapes from the ITEM profiles to a beam model cross section, the moment of inertias, and cross sections, have been adapted to rectangular hollow sections, so that they possess the same cross sectional properties with $\pm$ 2%.

**Mesh and boundary conditions**

The discretized model is hown to the right:

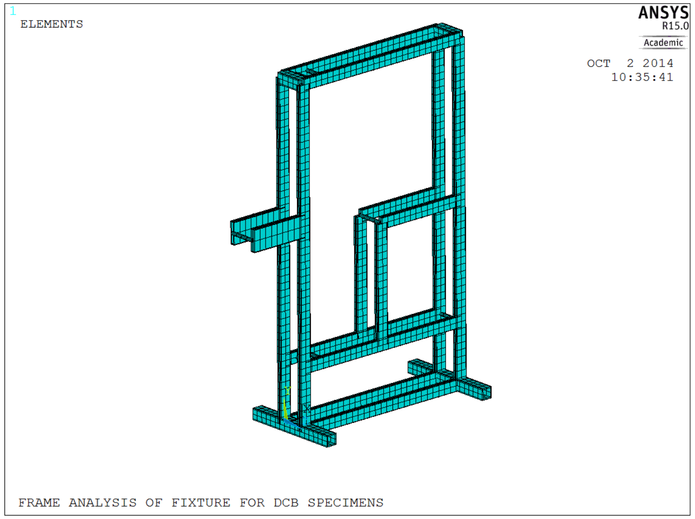


The boundary conditions of the model, can be seen in the figure to the right:

The loads applied correspond to a wire load of 2500 N under mode II loading.

I.e. the moment applied at the roller fixture corresponds to 1420 Nm.

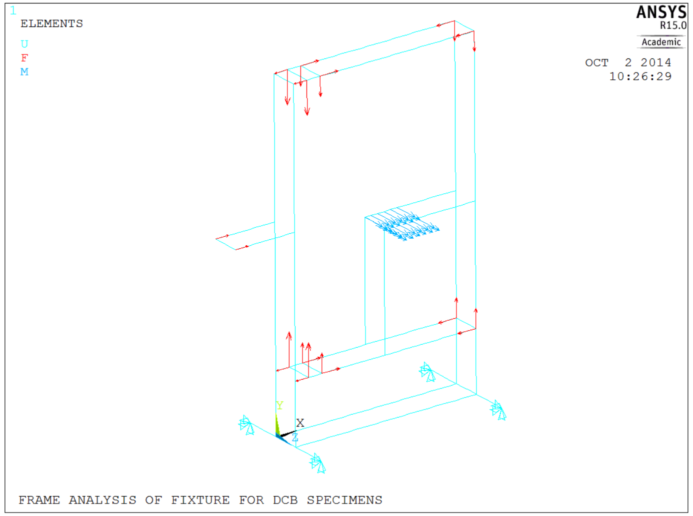


The input file for both static analysis and natural frequency analysis can be found on the DVD.

**Displacements and stresses**

The displacement vector sum is shown to the right:

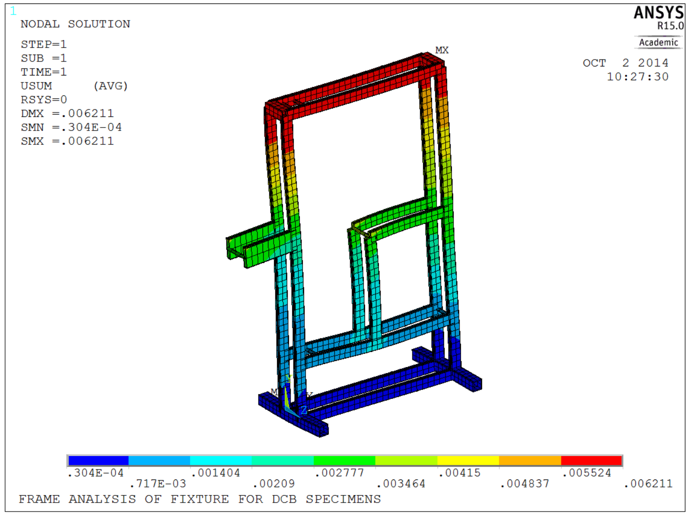


The von Mises stresses are shown here:

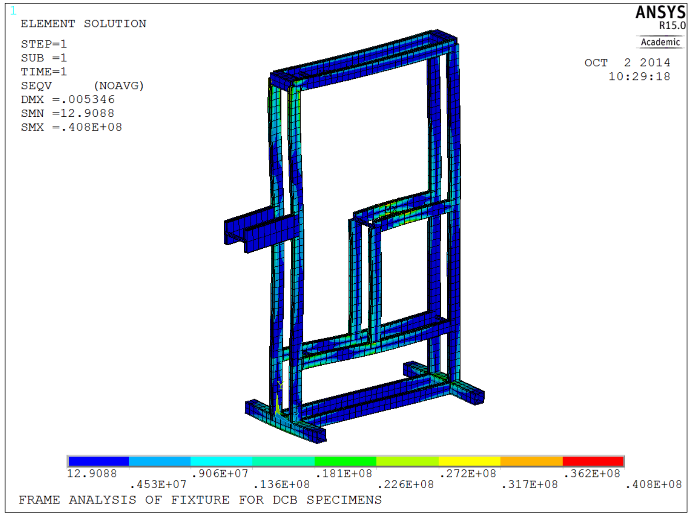


Maximum displacement in the model: $u_{max} := 6.2mm$

Maximum von Mises stress: $\sigma_{vm.max} := 40.8MPa$

## 5. Eigen frequency analysis of the frame

The natural frequency analysis is performed as a linear non-prestressed modal analysis. This can be done since no stress stiffening or large deformations are expected.

The first five mode frequencies are:

$$freq_1 := 8.03Hz$$

$$freq_2 := 12.4Hz$$

$$freq_3 := 17.7Hz$$

$$freq_4 := 31.13Hz$$

$$freq_5 := 38.63Hz$$

The first 2 mode shapes are motions that are not concerned with the loading directions. The third one is!

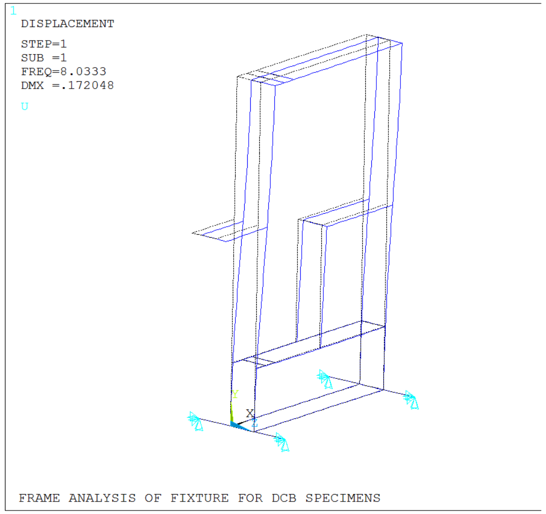


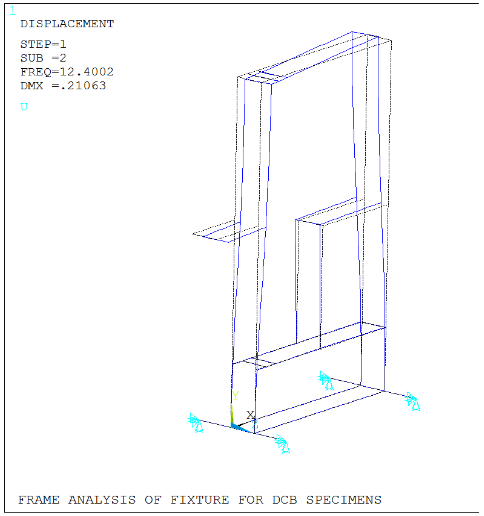


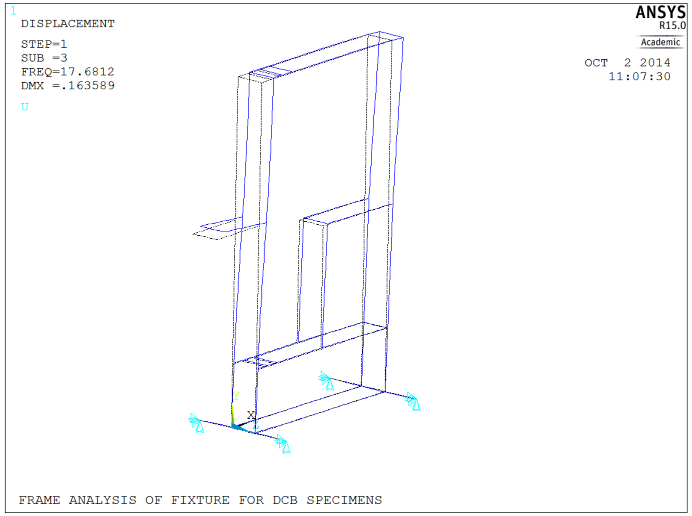


This means that, when applying dynamic loads to the structure, the input frequency, should be less than 1/3 of the minimum relevant natural frequency (Norton - Machine design). I.e.

Maximum input frequency:

$$freq_{max} := \frac{1}{3} \cdot freq_3 = 5.9 \cdot Hz$$

## 6. Static analysis of the wire rollers

The wire rollers as seen to the right are analyzed for their static strength.
The maximum applied load for any load case is used, which is for pure mode II loading for the largest specimens.

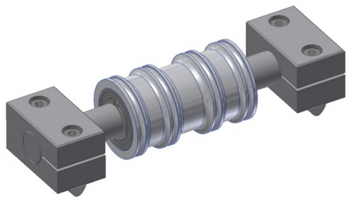

First the outer tube is verified:

Minimum outer diameter: $d_{out} := 53mm$

Minimum inner diameter: $d_{in} := 43mm$

Distances:

$L_{r.1} := 27mm$

$L_{r.2} := 45mm$

$L_{r.3} := 63mm$

$L_{r.4} := 90mm$

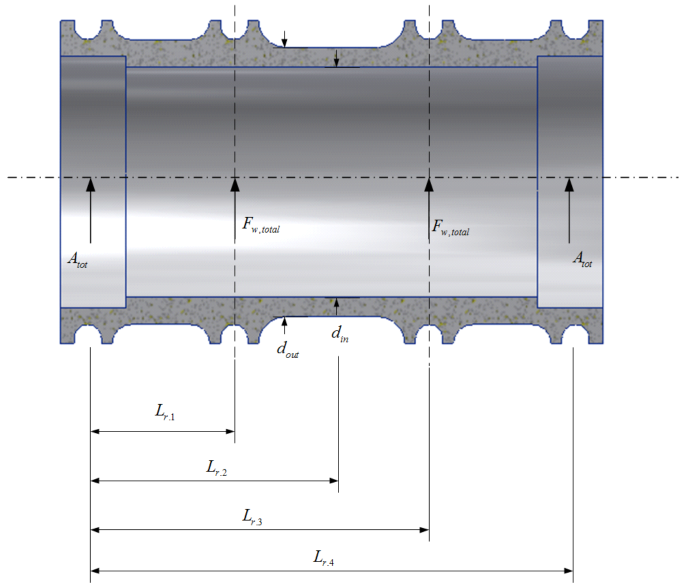


Moment of inertia: $I_{rol.1} := \frac{\pi}{64} \cdot \left(d_{out}^{\ 4} - d_{in}^{\ 4}\right)$ $\qquad I_{rol.1} = 219.5 \times 10^{3} \cdot mm^{4}$ Minimum moment of inertia, for the tube is taken!

The maximum wire force is determined as: $F_W := 2500N$

The total resultant acting on the rollers are calculated for those, that are loaded as seen in the figure below:

Here the angle θ is depending on how the system is setup. For these initial calculations, a maximum angle of:

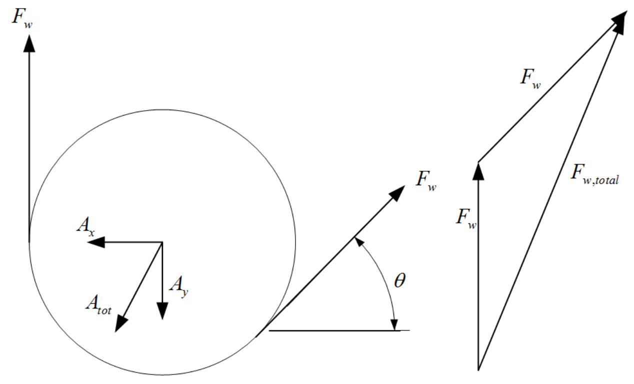


Maximum angle: $\theta_{rol} := 60deg$

Total force: $F_{w.total} := \sqrt{\left(F_W \cdot \cos\left(\theta_{rol}\right)\right)^2 + \left[F_W \cdot \left(1 + \sin\left(\theta_{rol}\right)\right)\right]^2}$ $F_{w.total} = 4829.6\,N$

The reaction is: $A_{tot} := -F_{w.total}$ $A_{tot} = -4829.6\,N$

Maximum moment in the pipe is located in the center and is calculated as:

$$M_{rol} := A_{tot} \cdot L_{r.2} + F_{w.total} \cdot \left(L_{r.2} - L_{r.1}\right) \qquad M_{rol} = -130.4 \cdot N \cdot m$$

Normal stress due to bending: $\sigma_{n.rol} := -\dfrac{M_{rol} \cdot d_{out}}{I_{rol.1} \cdot 2}$ $\sigma_{n.rol} = 15.7 \cdot MPa$

Utilization wrt. the yield stress:

$$U_{rol} := \frac{\sigma_{n.rol}}{R_{p02.6082}}$$

$$U_{rol} = 5.4 \cdot \%$$

Diameter shaft:

$$d_{shaft} := 25mm$$

Area of shaft:

$$A_{shaft} := \frac{\pi}{4} \cdot d_{shaft}^{2}$$

$$A_{shaft} = 490.9 \cdot mm^{2}$$

Distances:

$$L_{s.1} := 56mm$$

$$L_{s.2} := 100mm$$

$$L_{s.3} := 144mm$$

$$L_{s.4} := 200mm$$

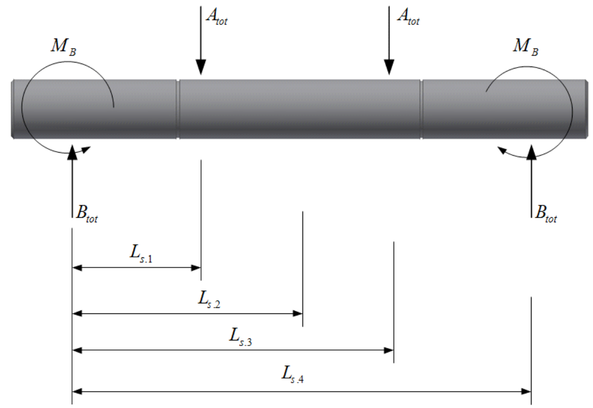


Moment of inertia:

$$I_{shaft} := \frac{\pi}{64} \cdot d_{shaft}^{4}$$

$$I_{shaft} = 19.2 \times 10^{3} \cdot mm^{4}$$

Reaction load:

$$B_{tot} := -A_{tot}$$

$$B_{tot} = 4829.6\,N$$

Please note, that the shaft is assumed fixed supported in both ends!

Maximum moment: $M_{shaft} := -A_{tot} \cdot \frac{L_{s.1}^{2} \cdot \left(L_{s.2} - L_{s.1}\right)}{L_{s.2}^{2}}$ $M_{shaft} = 66.6 \cdot N \cdot m$

Normal stress: $\sigma_{n.shaft} := \frac{M_{shaft} \cdot d_{shaft}}{2 \cdot I_{shaft}}$ $\sigma_{n.shaft} = 43.4 \cdot MPa$

Utilization wrt. the yield stress: $U_{shaft.\sigma} := \frac{\sigma_{n.shaft}}{f_y}$ $U_{shaft.\sigma} = 8.9 \cdot \%$ The material is C45 steel.

Maximum shear stress: $\tau_{shaft} := \frac{4 \cdot A_{tot}}{3 \cdot A_{shaft}}$ $\tau_{shaft} = -13.1 \cdot MPa$

Utilization wrt. the yield stress: $U_{shaft.\tau} := \frac{\left|\sqrt{3} \cdot \tau_{shaft}\right|}{f_y}$ $U_{shaft.\tau} = 4.6 \cdot \%$ The material is C45 steel.

## 7. Static analysis of the roller support structure

The roller support structure (ss) will only experience load, in case of mode mixity or pure mode II loading.
**Important:** The roller support structure is only designed for the small specimens, and will need small modifications in order to cope with the large specimens!!!

Distances:

$L_{ss.1} := 44mm$

$L_{ss.2} := 82mm$

$L_{ss.3} := 35mm$

$L_{ss.4} := 100mm$

$L_{ss.5} := 85mm$

$L_{ss.6} := 170mm$

$L_{ss.7} := 130mm$

$L_{ss.8} := 41mm$

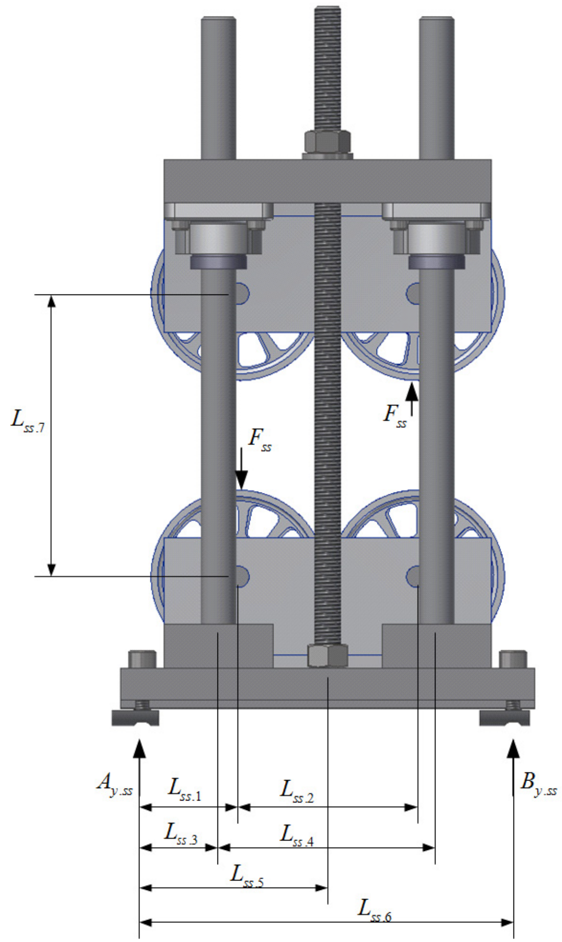

The maximum load the support structure can be loaded with is coming from pure mode II loading.

Maximum moment: $M_{II.L} = 420 \cdot N \cdot m$

The moment as a force pair: $F_{ss} := \dfrac{M_{II.L}}{L_{ss.2}}$ $\quad F_{ss} = 5122\,N$

Reactions: $B_{y.ss} := -\dfrac{1}{L_{ss.6}} \cdot \left(F_{ss} \cdot L_{ss.2}\right)$ $\quad B_{y.ss} = -2470.6\,N$

$A_{y.ss} := -B_{y.ss}$ $\quad A_{y.ss} = 2470.6\,N$

The free body diagram of the upper part can be seen to the right.

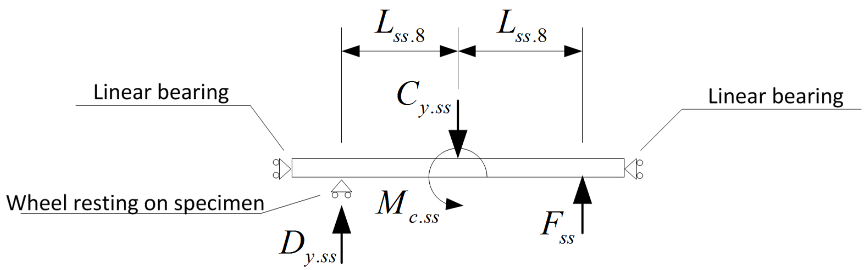


The reactions at C: $C_{y.ss} := -F_{ss}$ $\quad C_{y.ss} = -5122\,N$

$M_{c.ss} := F_{ss} \cdot L_{ss.8}$ $\quad M_{c.ss} = 210 \cdot N \cdot m$

This moment is small compared to the dimensions of the plate. Therefore no stress calculation is performed!

The reaction at D: $D_{y.ss} := 0MPa$

The supporting wheels are calculated based on the largest loads possible acting on one wheel: $\frac{F_{SS}}{2} = 2561\,N$

It is assumed that two wheels will carry the entire load. The wheel is analyzed using a solid FE model, with the following data:

| | | |
|---|---|---|
| Element types: | Solid187 | Ansys 20 node brick elements |
| No. of elements: | 204000 | |
| No. of nodes: | 827852 | |

The load is applied on a small surface, to approximate the area of contact. The inside of the wheel, where the bearing is located, is restrained against all translations and rotations, using a bearing support condition. Symmetry could have been used, but the preprocessing time, would exceed the additional solution time. Furthermore 100 N, is applied in the axial direction (z), to simulate out of plane loads.

The discritized model:

The boundary conditions:

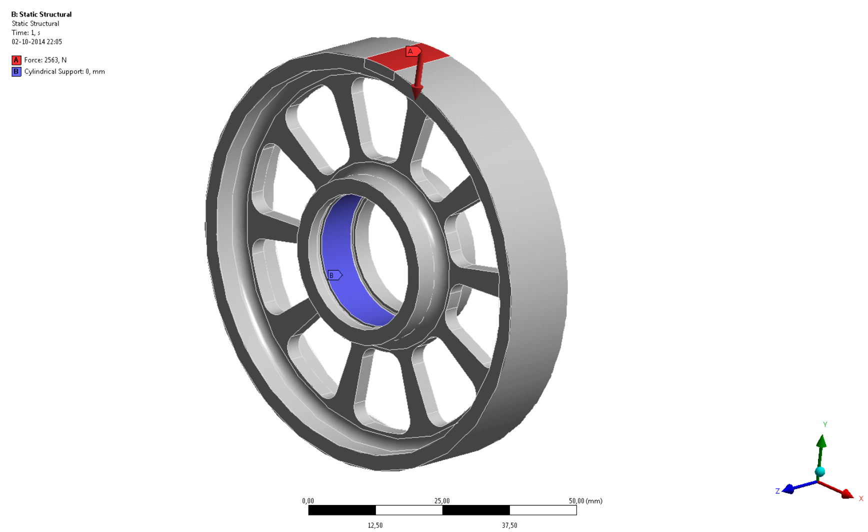


**The results:**

The von Mises stress in the wheel is high in a certain area.

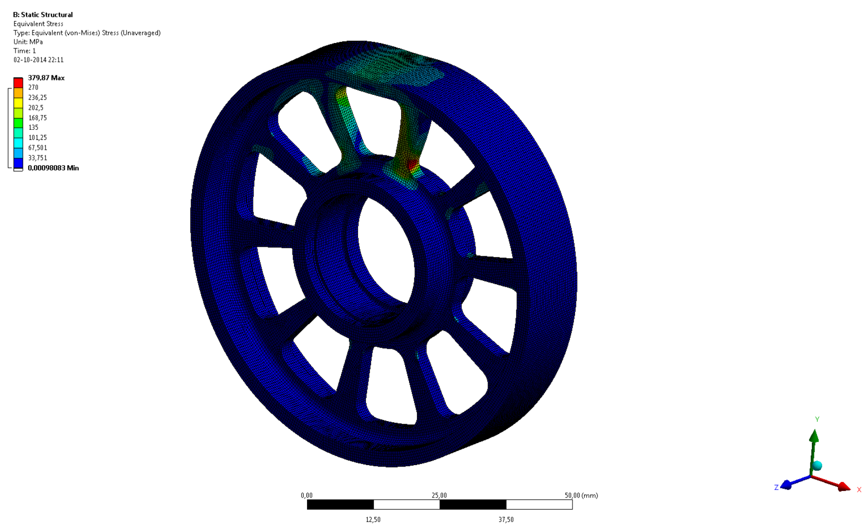

Cutting through the wheel, were the maximum stress is located, we can see, that the stress is confined to less than 0.5 mm from the surface.

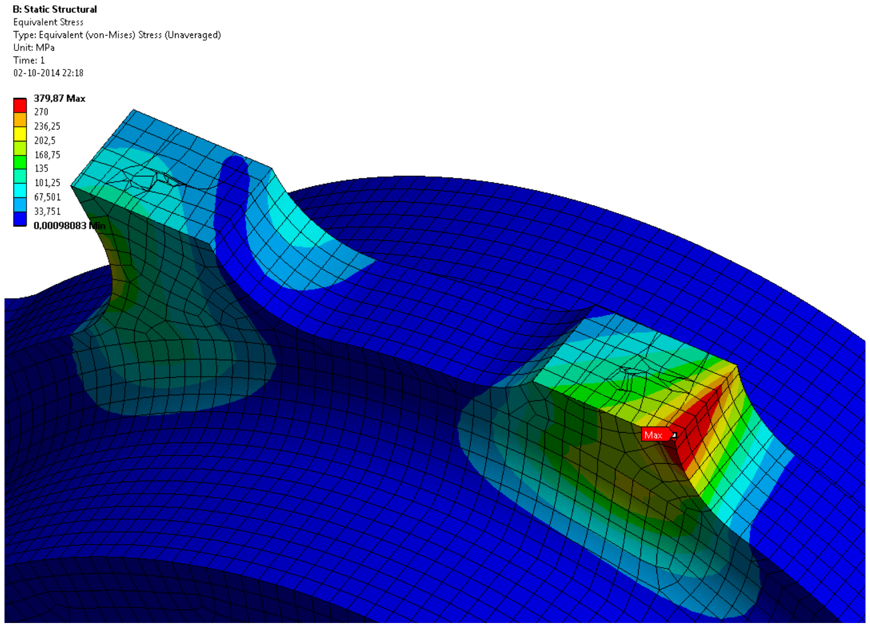


The yield stress of the wheels:

$$R_{p02.2014} = 420 \cdot MPa$$

This clearly indicates, that the stresses in the wheels are well below the admissible!

The shaft that holds the 3 wheels, is shown in a FBD to the right:

It is assumed that two wheels will distribute the load from $F_{ss}$ This means
That the middle wheel will always be carrying a load, but the other two can shift.

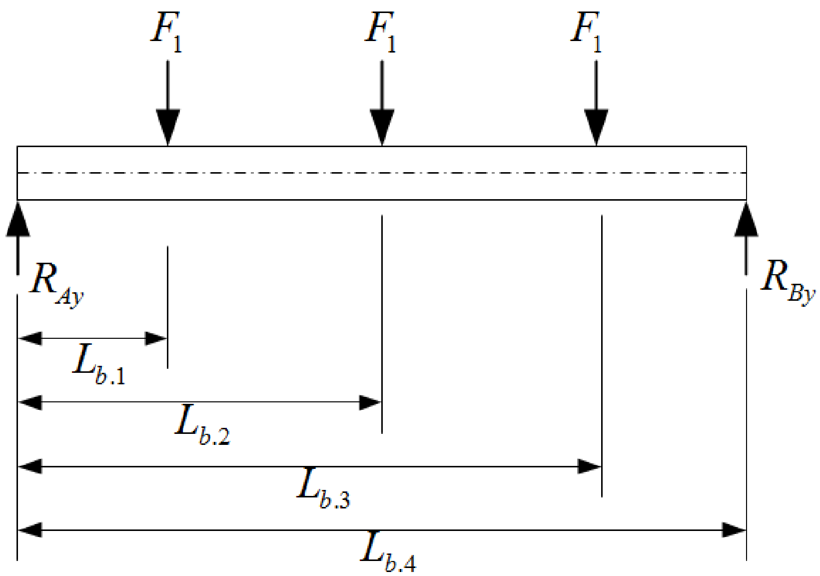


Shaft diameter: $d_{shaft.2} := 10mm$

Distances: $L_{b.1} := 8mm$

$L_{b.2} := 25.5mm$

$L_{b.3} := 42.5mm$

$L_{b.4} := 51mm$

Load: $F_1 := \frac{F_{ss}}{2}$ $F_1 = 2561\,N$

Reactions:

$$R_{Ay} := \frac{F_1 \cdot L_{b.3}}{L_{b.4}} + \frac{F_1}{2}$$ $R_{Ay} = 3414.6\,N$

$$R_{By} := 2 \cdot F_1 - R_{Ay}$$ $R_{By} = 1707.3\,N$

Moment function:

$$M(x) := \begin{vmatrix} \left(R_{Ay} \cdot x\right) \text{ if } 0 \le x < L_{b.1} \\ \left[R_{Ay} \cdot x - F_1 \cdot \left(x - L_{b.1}\right)\right] \text{ if } L_{b.1} \le x < L_{b.2} \\ \left[\left[R_{Ay} \cdot x - F_1 \cdot \left(x - L_{b.1}\right) - F_1 \cdot \left(x - L_{b.2}\right)\right]\right] \text{ otherwise} \end{vmatrix}$$

Maximum moment occurs in the center of the shaft - at $L_{b2}$

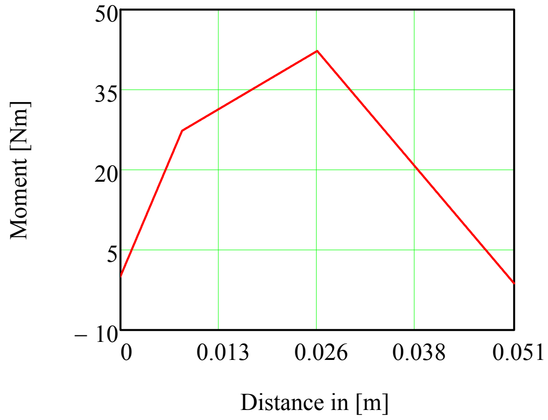


Moment of inertia for the shaft:

$$I_{shaft.2} := \frac{\pi}{64} \cdot d_{shaft.2}^{\,4}$$ $I_{shaft.2} = 490.9 \cdot mm^4$

Normal stress:

$$\sigma_{n.shaft.2} := \frac{M\left(L_{b.2}\right) \cdot d_{shaft.2}}{2 \cdot I_{shaft.2}}$$ $\sigma_{n.shaft.2} = 430.4 \cdot MPa$

Utilization wrt. the yield stress:

$$U_{shaft.2} := \frac{\sigma_{n.shaft.2}}{R_{p02.1.4305}}$$ $U_{shaft.2} = 87.8 \cdot \%$